Quantum simulation of doped two-dimensional Mott insulators

Joannis Koepsell

München 2021

Quantum simulation of doped two-dimensional Mott insulators

Joannis Koepsell

Dissertation
an der Fakultät für Physik
der Ludwig–Maximilians–Universität
München

vorgelegt von
JOANNIS KOEPSELL
aus Frankfurt am Main

München, den 05.01.2021

Erstgutachter: Prof. Dr. Immanuel Bloch
Zweitgutachter: Prof. Dr. Eugene Demler
Tag der mündlichen Prüfung: 11.02.2021

Zusammenfassung

Dotierte antiferromagnetische Mott Isolatoren sind der Ausgangspunkt vieler exotischer Phänomene stark wechselwirkender Elektronen, wie z.B. Hochtemperatursupraleitung oder Streifenphasen. Solche Systeme verletzen die Regeln konventioneller Metalle bereits bei Raumtemperatur durch Pseudogap und Strange-Metal Verhalten. Eine normale Fermiflüssigkeit entsteht lediglich bei starker Dotierung. Trotz jahrzehntelanger intensiver Forschung konnte bisher kein vollständiges Verständnis des Verhaltens beim Übergang von schwacher zu starker Dotierung erlangt werden.

Diese Arbeit liefert eine neuartige Perspektive auf dotierte zweidimensionale Mott Isolatoren durch Quantensimulation mit kalten Atomen in optischen Gittern bei Temperaturen um die Austauschkopplungsenergie. Mehr als 70 000 Fotografien von dotierten Fermi-Hubbard Systemen wurden aufgenommen, in welchen Ort und Spin jedes Teilchens durch aufwändige Mikroskopietechnik detektiert sind. Dabei konnte die starke Kopplung zwischen antiferromagnetischen Korrelationen und der Delokalisierung von Dotanden direkt beobachtet und charakterisiert werden. Die hier ausgewerteten Spin-Ladungs Korrelatoren ermöglichen mikroskopische Beobachtungen, welche in traditionellen Festkörperexperimenten unzugänglich sind.

Eine direkte Abbildung magnetischer Polaronen wurde im Regime einzelner Dotanden erstellt. Die Wolke aus reduzierten magnetischen Korrelationen, welche Dotanden stets umgibt, konnte mittels eines Dreipunktkorrelators aufgedeckt werden. Diese hat eine kompakte Größe von zwei Gitterplätzen im Durchmesser und ihre innere Struktur enthält Spinkorrelationen mit umgekehrtem Vorzeichen im Vergleich zum antiferromagnetischen Hintergrund. Die Mobilität der Dotanden war eine notwendige Voraussetzung für die Entstehung magnetischer Polaronen.

Des Weiteren zeigen wir die Auflösung eines Metalls aus magnetischen Polaronen in eine normale Fermiflüssigkeit durch die Vermessung von Mehrpunktkorrelatoren mit ansteigender Dotierung. Die Transformation äußert sich in allen betrachteten Observablen und schließt bei Dotierungen um 30 % ab. Am Übergang zwischen beiden Regimen finden wir negative Spinkorrelationen in der Nähe von Dotandenpaaren, welche eine Verbindung zu Prozessen bei niedrigerer Temperatur andeuten.

Die Entwicklung und Implementierung eines stabilen vertikalen zweifarbigen Übergitters konnte die Leistungsfähigkeit unseres Simulators signifikant erweitern. Effiziente Zweilagenmikroskopie erlaubt nun mehr als eine Verdopplung der zweidimensionalen Systemgröße bei voller Spin- und Dichteauflösung.

Die präsentierte Übergittertechnologie ebnet den Weg für weitere Kühlmethoden. Durch das Erreichen niedrigerer Temperaturen könnte in Zukunft der Zusammenhang zwischen magnetischen Polaronen und Hochtemperatursupraleitung erforscht werden.

Abstract

Doped antiferromagnetic Mott insulators lie at the heart of many exotic phenomena of strongly-interacting electrons, such as high-T_c superconductivity or stripe phases. These systems violate the rules of conventional metals already at room temperature by pseudogap and strange-metal behavior. A normal Fermi liquid develops only at strong doping. Despite decades of intense research, a complete understanding of the transformation from weak to strong doping is lacking.

This thesis provides a novel perspective on doped two-dimensional Mott insulators through quantum simulation, based on cold atoms in optical lattices at temperatures around the superexchange energy. Over 70 000 photographs of doped Fermi-Hubbard systems were taken, in which the location and spin of every particle is resolved with advanced microscopy techniques. Thus, we directly observed the intricate interplay between antiferromagnetic correlations and the delocalization of dopants. The higher-order spin-charge correlators evaluated within this thesis enable microscopic observations, which are inaccessible to traditional solid-state experiments.

A direct real-space image of magnetic polarons is reported in the single dopant regime. The magnetic dressing cloud surrounding individual dopants is revealed with a three-point correlator. It features a compact size of about two sites in diameter and its inner structure contains sign-reversed spin correlations compared to the antiferromagnetic background. The mobility of dopants is demonstrated to be an essential ingredient for polaron formation.

Moreover, we show how a metal of magnetic polarons dissolves into a conventional Fermi liquid, by tracking the evolution of several multi-point correlations with increasing doping. The transformation is signaled across all measured observables and is completed at dopings around 30 %. At the crossover between both regimes, we find negative spin correlations in the vicinity of pairs of dopants, which hint a connection to the lower temperature physics.

We designed and implemented a highly-stable vertical bichromatic superlattice to significantly improve the capabilities of our simulator. It enables efficient bilayer microscopy and more than doubles the size of two-dimensional systems at full spin and density resolution.

The developed superlattice technology paves the way for multiple further cooling schemes. By reaching lower temperatures, the link between magnetic polarons and high-T_c superconductivity could eventually be explored in the future.

Contents

To my family

---

*"When you change the way you look at things,
things you look at change."*

— Max Planck

Introduction

Electronic systems are fundamental to modern technology because they govern some of the most useful properties of a material [1]. For instance, electrons in photo-voltaic cells convert solar energy from the sun [2], classical computers rely on semi-conducting properties of electrons, superconducting electrons create magnetic fields for medical surgery[1] or Nobel-prize-winning Higgs boson discoveries[2] [3, 4]. Despite their importance, computing the behavior of electrons in condensed-matter systems quickly becomes intractable, since in many cases a quantum mechanical treatment of interacting particles is required. Electronic properties of materials are a cornerstone of technological progress, but many phenomena are still poorly understood.

One of the greatest puzzles of electronic quantum matter are anomalous metallic states, which can emerge from strong interactions between electrons. Such states are found e.g. in heavy-fermion alloys [5], organic conductors [6] or doped ceramics [7]. Defining properties of these materials are unusual resistivities or magnetic susceptibilities as well as excitations, which strongly deviate from the ones of normal metals, such as copper. For the physics of normal metals, a theoretical framework exists, which was developed by Lev Landau [8]. According to Landau, interacting electrons can form a Fermi liquid (FL), which behaves just like non-interacting electrons with renormalized properties [9]. The validity of such a description might be surprising, given the ubiquitous and strong Coulomb interaction of electrons. But the concept turned out to work extremely well for many systems. All metals with Fermi-liquid behavior, such as copper, are termed *normal*. Their physics is universal and well understood. The violation of Fermi-liquid behavior is a hallmark of strongly-correlated quantum materials [10]. Such anomalous (i.e. non-FL) metallic states pose many open questions to their underlying microscopic processes.

In the copper-oxide ceramics, *d*-wave superconductivity emerges from an anomalous strange-metal regime at unconventionally high temperatures up to 135 K at room pressure[3] [10, 13, 14]. Another anomalous phenomenon in copper oxides is the pseudogap [15], which originates from doping holes into an otherwise antiferromagnetic Mott insulating parent compound. Intriguingly, the strange metal can turn into a conventional Fermi liquid by only slightly increasing the doping concentration [16–19]. The transformation between the anomalous and normal regime is among the greatest mysteries in condensed matter physics [10, 20]. A prominent scenario linking all three phenomena – pseudogap, strange metal, Fermi liquid – is the existence of a quantum

---

[1] such as nuclear magnetic resonance
[2] at the Large Hadron Collider
[3] conventional superconductivity at room temperature was realized at extreme pressures [11, 12]

phase transition as a function of doping [21, 22]. But decades after the initial Nobel-prize-winning discovery of these materials in 1986 by Bednorz and Müller [23], much of their physics still defies a complete understanding.

Significant insights could be gained from countless experimental studies [10, 13, 14, 24], but fundamental challenges remain. The complex structure of real materials complicates conclusions on whether phonons, band structure, or magnetic couplings are the driving mechanism for an observation [25, 26]. Furthermore, observables such as higher-order correlations between spins and holes remain inaccessible in traditional solid-state experiments, which are based on conventional two-point correlations. The tunability of parameters in real materials is limited and every measurement at different doping requires the production of a dedicated sample.

Numerical calculations of interacting electrons are very difficult on classical computers, due to an exponentially growing Hilbert space with system size. While progress has been made [27, 28], insights are often restricted to small systems or parameter regimes and approximate numerical methods are limited by the fermion sign problem [29, 30]. The computational power of classical computers seems to approach an end of Moore's law[4]. Current transistor sizes have reached 10 nm [31], while the Van-der-Waals radius of silicon is ~ 0.22 nm [32]. The miniaturization of components therefore approaches an end, which is calling for a new era of quantum computing.

Feynman envisioned that solving quantum problems ultimately requires quantum technology [33]. The race for controlling quantum objects to perform computations with them has dramatically gathered pace across the globe in the last years. Promising progress towards a quantum computer could recently be demonstrated [34, 35]. Nonetheless, general quantum computation of electronic systems will not be available in the near future [36]. From the current perspective, specialized quantum technology will be required to solve a particular quantum-many-body problem.

Ultracold atoms have emerged as specialized quantum simulators to study strongly-correlated quantum matter [37, 38]. Neutral atoms in optical lattices can be controlled to mimic the behavior of electrons in solid-state systems [39]. Defect-free versions of the two-dimensional Fermi-Hubbard model can be implemented [40], which is often believed to capture the essential physics of high-T_c materials like the cuprates [41]. The demonstration of fermionic Mott insulators [42, 43] and the detection of antiferromagnetic spin correlations [44, 45] constituted important steps towards cold-atom based simulation of Fermi-Hubbard physics.

Recent breakthroughs in the manipulation and detection of quantum gases have

---

[4]Moore's law is an empirical statement: the number of transistors on a chip doubles every two years (and usually with it the computational speed).

enabled powerful lattice simulators with single-particle resolution [46–48]. This quantum gas microscopy technique could be extended to Fermi-Hubbard systems in 2015 [49–53], which paved the way for probing synthetic electronic systems at the single-particle level. Based on thousands of snapshots of the collapsed many-body wavefunction classical two-point [54–56], as well as novel string [57], or spin-charge correlators [58] can be measured. More conventional quantities, such as transport properties [59, 60], structure factors [61], susceptibilities [62–64], and angle-resolved photoemission spectroscopy measurements [65–68] are also accessible in cold-atom experiments. Even dynamical tracking of observables is possible in systems out-of-equilibrium because the dynamics of particles is slower than experimental control electronics [59, 60, 69, 70]. High tunability of interaction, hopping, and doping parameters qualify cold-atom systems as an ideal platform to probe strongly-correlated fermions and their anomalous metallic states in unprecedented ways.

Major efforts are underway to perform cold-atom quantum simulation of anomalous metallic states and d-wave superconductivity in doped two-dimensional Mott insulators. To this end, reaching low enough temperatures is a major challenge. The current state of the art are temperatures down to $T = 0.25\text{-}0.4\,t$ [60, 61, 71], where t denotes the tunneling energy (Boltzmann constant is set to $k_{\mathrm{B}} = 1$). In this regime, long-range antiferromagnetism has been observed [61] and how doping diminishes average spin-spin correlations [54, 55, 61, 72]. These and further dynamical studies of single-site [70] or long-wavelength [60] density modulations suggest an intricate interplay between dopants and spin correlations already at currently accessible temperatures, which might be linked to anomalous metallic properties.

This thesis reports experimental spin-charge correlations up to higher order in doped two-dimensional Fermi-Hubbard systems. Measurements were performed on the ^{6}Li-based MPQ quantum simulator with full spin and density resolution. We reveal the magnetic dressing cloud of single dopants and thus confirm the microscopic real-space picture of magnetic polarons. We study how a metal of magnetic polarons dissolves into a Fermi liquid by continuously increasing the doping of Mott insulators. All measured observables indicate a crossover from a polaronic metal to a conventional metal, which completes around 30 % doping. The doping-induced evolution of microscopic correlations is compared to several theoretical concepts for weakly-doped Mott insulators. Spin-charge correlations show discrepancies to experimental data in particular in the crossover regime. Finally, developments of the quantum simulator are described, which concern the implementation of a highly-stable bichromatic superlattice. This technology opens the door to entropy engineering, which could enable exploration of essential aspects of the high-T_c puzzle at lower temperatures.

Outline

This thesis is organized as follows:

Chapter 1 reviews some of the puzzles of doped Mott-insulating copper oxides and discusses the connection to the field of ultracold neutral atoms in optical lattices. Common simplifying theories for the weak doping regime are presented. The concept of correlators as well as their visual representation and decomposition into connected and disconnected parts are introduced.

Chapter 2 describes the experimental apparatus. A particular focus is provided on engineering optical superlattices and the bilayer detection method. The scheme for full spin- and density-resolution of a monolayer is explained and the readout of strongly-interacting bilayer Fermi-Hubbard systems is presented.

Chapter 3 summarizes a study of weakly doped Mott insulators, in which images of the dressing cloud of magnetic polarons were taken. Furthermore, the necessity of dopant motion for magnetic polaron formation is shown, by demonstrating how the confinement of a dopant to a single lattice site leads to a disappearance of the magnetic dressing.

Chapter 4 contains information on how various correlators up to fourth order evolve when Mott insulators are doped from polaronic metal to Fermi liquid. The crossover is found to be located around doping of 30 %, where all studied observables undergo a significant change. The polaronic metal has an anomalous doping-dependence of the spin susceptibility and the Fermi liquid exhibits incommensurate spin fluctuations. The spin environment of pairs of dopants is investigated and significant correlations are discovered, which point to a connection to possible hole pairing scenarios at colder temperatures.

Publications

The following papers were published in the course of this PhD thesis. Publications relevant to the content of this manuscript are highlighted:

- **Microscopic evolution of doped Mott insulators from polaronic metal to Fermi liquid**.
  J. Koepsell, D. Bourgund, P. Sompet, S. Hirthe, A. Bohrdt, Y. Wang, F. Grusdt, E. Demler, G. Salomon, C. Gross and I. Bloch. pre-print, arXiv:2009.04440 (2020).

- Dominant fifth-order correlations in doped quantum anti-ferromagnets.
  A. Bohrdt, Y. Wang, J. Koepsell, M. Kánasz-Nagy, E. Demler, F. Grusdt.
  pre-print, arXiv:2007.07249 (2020).

- **Robust bilayer charge pumping for spin- and density-resolved quantum gas microscopy**.
  J. Koepsell, S. Hirthe, D. Bourgund, P. Sompet, J. Vijayan, G. Salomon, C. Gross and I. Bloch. Physical Review Letters **125**, 010403 (2020).

- Time-resolved observation of spin-charge deconfinement in fermionic Hubbard chains.
  J. Vijayan*, P. Sompet*, G. Salomon, J. Koepsell, S. Hirthe, A. Bohrdt, F. Grusdt, I. Bloch and C. Gross. Science **367**, 6474 (2020).
  * *Equal contributions*

- **Imaging magnetic polarons in the doped Fermi-Hubbard model**.
  J. Koepsell, J. Vijayan, P. Sompet, F. Grusdt, T.A. Hilker, E. Demler, G. Salomon, I. Bloch and C. Gross. Nature **572**, 358-362 (2019).

- Direct observation of incommensurate magnetism in Hubbard chains.
  G. Salomon, J. Koepsell, J. Vijayan, T.A. Hilker, J. Nespolo, L. Pollet, I. Bloch and C. Gross. Nature **565**, 56-60 (2019).

1 | ⊞ → ⚛

From real to synthetic electronic systems

The copper-oxide materials and their properties pose some of the most challenging questions in solid-state physics. Gaining insight into exotic phenomena emerging in such strongly-correlated electronic systems is a key motivation for this thesis. This chapter starts with a phenomenological introduction of copper oxides at intermediate temperatures, comparing the Fermi liquid with pseudogap or strange metallic behavior. Many different mechanisms determine the properties of cuprate superconductors, but one of them stands out: a fierce battle between magnetic and kinetic processes. The two-dimensional Fermi-Hubbard model describes such a competition and, therefore, serves as a basic approach to study strongly-correlated electrons. We present the competition between antiferromagnetic correlations and dopant motion in this model, which leads to the concept of magnetic polarons. Such polarons might be intimately connected to anomalous metallic properties. Finally, cold-atom-based quantum simulation of the Fermi-Hubbard model is summarized and the novel correlator-based analyses afforded by these machines are introduced.

1.1   Cuprates - phenomenology of anomalous metals

1.1.1   Mott insulators as parent compounds

One of the most heavily studied cuprates are compounds of the yttrium-barium-copper-oxide (YBCO) family. A photograph of such a material is shown in Fig. 1.1a. The internal structure of copper oxides can be approximated by weakly-coupled two-dimensional (2d) layers [10, 13, 14]. In the most simple picture, electrons stay in a single layer and hop or interact on a 2d square lattice [74], see Fig. 1.1b. The parent compounds are brittle ceramics with excellent insulating properties, even though the non-interacting band structure is only half filled (i.e. one particle per lattice site). Due to the strong Coulomb repulsion of electrons on the same lattice site, charge transport becomes strongly suppressed. This is called a Mott insulator [75]. Already around
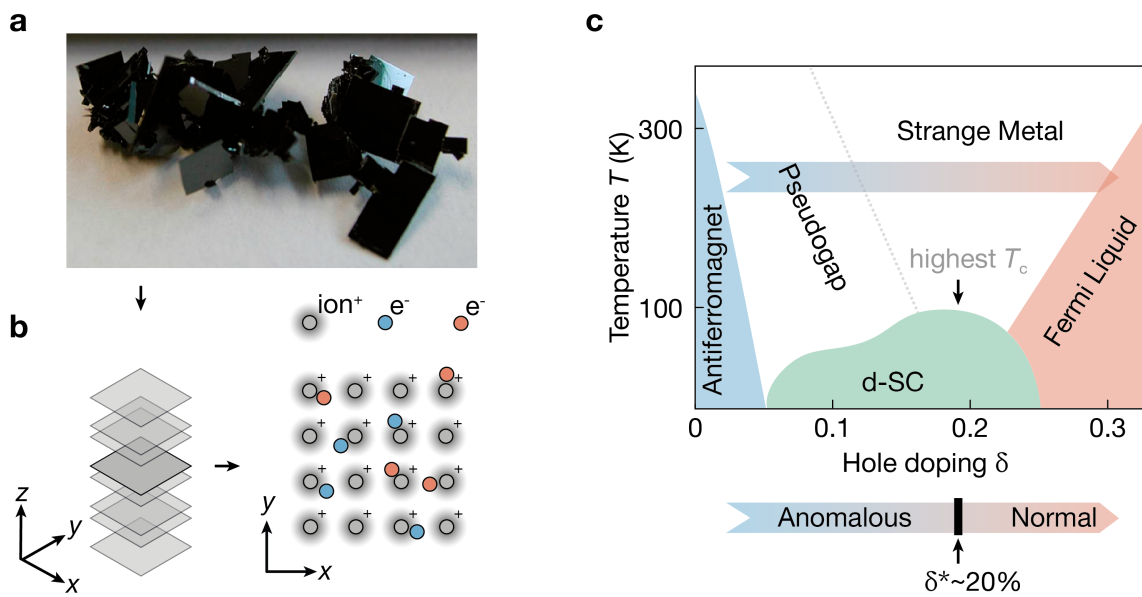
Figure 1.1: Copper oxides and their phase diagram. a, Photograph of grown YBCO crystals, taken from [73]. The visual appearance is very dark and shiny. **b**, Cuprate materials consist of weakly coupled 2d layers (here shown as stacked bilayers). In the simplest approximation, electrons are confined within a single 2d layer. The ion crystal in this monolayer can be approximated by a square lattice. **c**, A sketch of the phase diagram for copper oxides as a function of temperature and hole doping, reproduced from [10]. Just below room temperature, hole doping leads to a change from an anomalous metal to a normal Fermi liquid (see arrow). The transformation between the two metallic regimes was found to occur around 20 % doping in copper oxides.

room temperature, most Mott insulators additionally develop long-range antiferromagnetism [76, 77].

1.1.2 Doping at intermediate temperatures

The most interesting phenomena of copper oxides are found as a function of hole doping δ and temperature T, see Fig. 1.1c. Doping of cuprates is performed by changing the chemical composition of the material, which effectively removes (or adds) free electrons from the 2d half-filled lattice. Resulting holes (or double occupations) in a Mott insulator can move through the system and restore the ability to conduct heat or electricity.

For hole dopings close to half filling, the resulting metallic states have anomalous

properties already around and below room temperature. The initial antiferromagnetic order is quickly destroyed in the presence of doping, but measurements suggest short-range magnetic correlations play an important role up to dopings way beyond the antiferromagnetic phase [78]. Only when hole doping is sufficiently large, the system turns into a normal Fermi liquid. The transition from an anomalous to a normal metal in copper oxides occurs around a specific doping across many observables [18, 19], referred to as $\delta^\star \sim 20\,\%$.

1.1.3   The anomalous metal

For hole dopings between Mott insulator and Fermi liquid (FL), two phenomena stand out. Pseudogap [15] and strange metal behavior occur in the anomalous regime. How those two are related is not clear. The pseudogap phenomenon is often linked to the concept of pre-formed pairs, which might form prior to superfluidity at colder temperatures [79]. Strange metals have no sharp FL-quasiparticle excitations [16, 19] (therefore sometimes referred to as incoherent metal) and a conductivity with unconventional temperature and frequency dependency. Such features are also found across many other types of materials with strongly-interacting electrons [80]. For many decades, measurements of the anomalous regime in copper oxides have been performed. Even though the observed characteristics have no generally accepted explanation, some of them have become the defining properties of the pseudogap or strange metal phase. To gain an intuition for the peculiar effects seen in solid-state measurements, Fig. 1.2 sketches some of the established findings. There are of course many more observations, which can be found in references [10, 13, 14].

The Fermi surface is a surface in quasi-momentum space q, which separates occupied from unoccupied states. It can be measured with angle-resolved photoemission spectroscopy (ARPES). For a Fermi liquid of weakly-interacting electrons on a square lattice, this surface is a square at half filling and a circular shape below half filling, see Fig. 1.2a. Such a surface follows from the non-interacting band structure of the underlying 2d lattice and is indeed observed for the Fermi liquid in cuprates [17]. For the anomalous metal, the Fermi surface is cut into so-called Fermi arcs [15, 81], which violate the FL concept of a closed surface formed by FL-type quasiparticles. The suppression of weight occurs for momenta, where a pseudogap opens in the spectrum. Nonetheless, quantum oscillation measurements suggest an actual Fermi surface does exist [82–84]. Common speculation is that these arcs are actually pockets forming an own Fermi surface growing with doping [85]. Why only the arc part of the pocket should be seen in ARPES measurements remains unclear. A possible explanation for the Fermi-arc phenomenon in terms of magnetic polarons and their internal structure was recently presented in the strong-coupling limit [86].

The uniform spin susceptibility χ_s quantifies how much the system can be magnet-
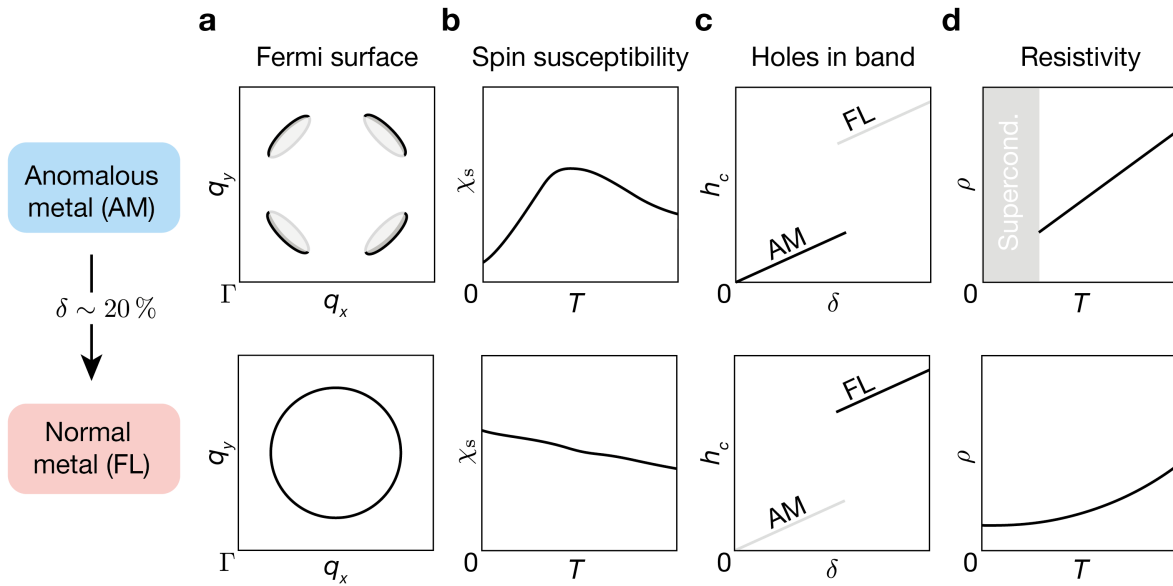
Figure 1.2: Properties of anomalous and normal metallic regimes in copper oxides. Sketching the qualitative change of copper oxide behavior from anomalous metal (AM) to normal metal (FL). **a**, The Fermi surface is cut into four arcs at weak doping (reproduced from [10]), while the FL possesses a closed circular surface at strong doping. The gray shading at weak doping indicates a speculated pocket scenario, see text. **b**, The uniform spin susceptibility drops at low temperatures at weak doping (reproduced from [87]), but is approximately constant with temperature in the FL regime. **c**, The number of hole charge carriers in the lowest band is proportional to δ at weak doping (reproduced from [18]), but increases as $1 + \delta$ in the FL regime. **d**, The in-plane resistivity scales linearly with temperature in the strange metal (reproduced from [88]), but grows quadratically in the FL.

ically polarized, e.g. by an external magnetic field. In solid-state systems this quantity can be obtained through Knight shift measurements with nuclear magnetic resonance [87, 89, 90]. For non-interacting fermions, and thus for a weakly-interacting FL, the susceptibility is independent of temperature [9], see Fig. 1.2b. For a Mott insulator, a transition into an antiferromagnetic phase occurs as a function of temperature. Antiferromagnetic correlations strongly suppress the susceptibility to an external field. For the pseudogap regime, a similar suppression is observed. Below a finite temperature, the susceptibility strongly drops. Due to the proximity to the antiferromagnetic Mott insulator, this might not be surprising. The puzzling part is that this suppression is found also for hole dopings, where the long-range antiferromagnetic phase is absent in hole-doped copper oxides. This might be an indicator that the interplay between

antiferromagnetic correlations and doping persists up to much stronger dopings.

The hole charge carrier density h_c measures how many holes exist in the lowest occupied band, relative to the number of total possible spinless states in that band. This quantity can be probed by quantum oscillations or through Hall measurements. For a band insulator of non-interacting fermions, this carrier density is zero. For an empty band, it is two (two spin states). In a half-filled non-interacting system, $h_c = 2 \cdot 1/2 = 1$. In terms of doping δ w.r.t. half filling, the carrier density grows like $h_c = 1 + \delta$, see Fig. 1.2c. For a Mott insulator, the lower Mott band is fully occupied without any holes. At weak doping in the anomalous metal, h_c grows with doping like $h_c = \delta$ [18]. Around $\delta^\star \sim 20\,\%$, a rapid transformation from the Mott-like scaling δ to the Fermi-liquid scaling $1 + \delta$ sets in. Around this doping, Mott insulating processes seem to fade and the original non-interacting band structure and bandwidth start to be explored by the system.

The in-plane electrical resistivity ρ specifies how much the material resists to conduct current within the 2d plane when a voltage is applied. In the Fermi liquid, electron-electron scattering increases with temperature and leads to a scaling $\rho \propto T^2$, see Fig. 1.2d. The strange metal defies this dependence and scales linearly $\rho \propto T$, which is one of its defining properties [88, 91]. A second characteristic of normal metals is the Mott-Ioffe-Regel (MIR) limit, which states that the resistivity cannot grow indefinitely and saturates at some temperature. Strange metals show a linear increase as a function of temperature even beyond the MIR limit [80]. This is another indicator of behavior, which is in strong contradiction to Fermi-liquid theory.

In conclusion, the anomalous metal seems strongly connected to the physics of the parent Mott insulator and violates several paradigms of Fermi-liquid theory. At lower temperatures, collective effects such as charge-density waves (stripes) can emerge from the anomalous regime [92]. Most strikingly, superconductivity with d-wave symmetry (d-SC) is found at weak and intermediate dopings [93, 94]. In the cuprates, superconductivity at the highest temperatures emerges from the strange metal, which points to a deep connection between the two. While an understanding of unconventional superconductivity represents a major challenge itself, much less is known about the anomalous metallic states at more elevated temperatures. The connection between pseudogap or strange metals and conventional Fermi liquids is often perceived as one of the biggest mysteries in solid-state physics [10].

Many ingredients, such as phonons [95], inter-layer couplings, magnetism, or orbital degrees of freedom can play a role for the emergence of exotic phenomena in copper oxides. Nonetheless, two key processes are often believed to be responsible for the anomalous metallic regime and high-T_c superconductivity [14, 30, 41]: antiferromagnetic correlations of the Mott insulator and the motion of doped holes. The most simple model for doped Mott insulators, which captures those two competing

mechanisms, is the 2d Fermi-Hubbard model.

1.2 Fermi-Hubbard model

The competition between antiferromagnetism and hole motion in the doped copper oxides is believed to be the most important mechanism for their rich phase diagram [14, 30, 41]. The Fermi-Hubbard model is one of the most prominent theoretical models for this competition [96, 97]. It consists of spin-1/2 fermions on a 2d lattice, see Fig. 1.3. Particles can hop to nearest-neighbor sites with amplitude t. Opposite spins on the same lattice site repel each other with interaction energy U. The Hamiltonian is given by

$$\mathcal{H}_{\text{FH}} = -t \sum_{\langle i,j \rangle, s=\uparrow,\downarrow} (\hat{c}_{i,s}^\dagger \hat{c}_{j,s} + \text{h.c.}) + U \sum_i \hat{n}_{i,\uparrow} \hat{n}_{i,\downarrow} \; . \tag{1.1}$$

Here the operator $\hat{c}_{i,s}^\dagger$ ($\hat{c}_{i,s}$) creates (removes) a fermion of spin s at site i, $\hat{n}_{i,s}$ is the density operator at site i for particles with spin s, and $\langle i, j \rangle$ denotes nearest-neighbor sites.

Despite the presence of only two ingredients, the 2d Fermi-Hubbard model poses major challenges to its numerical or analytical computation. The Hilbert space grows exponentially with system size and an exact solution cannot be obtained in polynomial time [27]. In particular, in the most interesting weak and intermediate doping regime, Quantum Monte Carlo (QMC) methods suffer from a sign problem [29], requiring the development of alternative algorithms to reach more interesting regimes [28, 98]. This struggle of classical computation motivates major efforts in cold atom quantum simulation of the Hubbard model, which will be introduced in one of the following sections. The key processes and established numerical insights for this model are summarized below.

1.2.1 Mott insulator

At half filling, Fermi-Hubbard systems turn into a Mott insulator when the interaction U is larger than the free particle bandwidth $W = 8t$. In that case, every lattice site is occupied by exactly one fermion. In a virtual process, where two fermions with opposite spins briefly hop on top of each other and back, neighboring particles can exchange their spin. This leads to an antiferromagnetic superexchange coupling $J = 4t^2/U$, see Fig. 1.3b. If the temperature is as low as this energy scale $T \sim J$ (the Boltzmann constant is set to $k_B = 1$), the Mott insulator builds up strong antiferromagnetic correlations. Undoped cuprates are antiferromagnets at room temperature
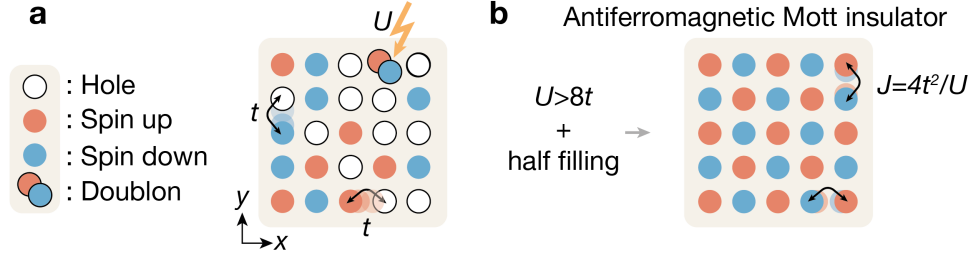
Figure 1.3: The Fermi-Hubbard model. a, Spin-1/2 fermions on a 2d, which can hop to nearest-neighbor sites with amplitude t. Opposite spins on the same lattice site repel each other with interaction energy U. **b**, At half filling and strong interactions, electron motion is blocked by the on-site repulsion and leads to a Mott insulating state. A higher-order superexchange with amplitude J is still possible. This mechanism allows opposite spins to exchange their place and causes antiferromagnetic spin couplings of nearest-neighbor lattice sites.

and estimates for their parameters are $t \sim 4500\,\mathrm{K}$, $U/t \sim 12$ and $J \sim 1500\,\mathrm{K}$ [14]. An important consequence of a theorem proven by Mermin and Wagner [99] is that the strict dimensionality (2d) of the Hubbard model implies the absence of an antiferromagnetic phase at finite temperature in an infinite system. Nonetheless, antiferromagnetic correlations can still build up at finite temperature over scales much larger than the size of a finite system. The transitions between different regimes in the 2d Hubbard model, therefore, behave not as phase transitions but as crossovers. For copper oxides, a finite inter-layer coupling invalidates the Mermin-Wagner theorem and leads to a phase transition at finite temperature. This subtlety does not play an important role in this work.

Another manifestation of the superexchange process is the occurrence of doublon-hole fluctuations. These are short-lived quantum fluctuations, which are directly linked to the superexchange. A fermion hops on top of another fermion with opposite spin but takes a finite amount of time to hop back. When a snapshot of the system is taken, these fluctuations manifest as a hole and a double occupation (doublon) detected next to each other. Such doublon-hole fluctuations are strongly suppressed for increasing U/t. In the infinite U limit, the Fermi-Hubbard model, therefore, maps onto a Heisenberg model of spins with antiferromagnetic spin couplings J [97]

$$\mathcal{H}_{\mathrm{Heis}} = J \sum_{\langle i,j \rangle} \hat{S}_i \hat{S}_j \ , \tag{1.2}$$

where $\hat{S}_i$ is the spin operator at site i.

When analyzing the physics of doped Mott insulators, theorists often turn to the

related t-J model [97]. It neglects the physics of doublon-hole fluctuations, by assuming a Heisenberg model in which holes can hop around with amplitude t. This approximation significantly simplifies the numerics as compared to the bare Hubbard model.

1.2.2 Kinetic vs magnetic energy

The Hubbard model is particle-hole symmetric, which means there is no difference between doublon or hole doping [100]. For now, dopants are considered to be holes. The fierce competition between antiferromagnetically correlated spins in the Mott insulator and the kinetic energy of doped holes is the key mechanism driving exotic regimes in the 2d Fermi-Hubbard model. This can be illustrated by contemplating the ground state of a single doped hole placed in an antiferromagnetic Mott insulator, see Fig. 1.4. The background particles minimize their magnetic energy by maintaining strong antiferromagnetic correlations. A doped hole on the other hand requires minimization of its kinetic energy, which is only possible if the hole is allowed to delocalize. This requires the hole to propagate through the system by the hopping process t. Already the effect of a single hopping event of the hole is detrimental to the antiferromagnetic correlations. The hole shuffles around the position of a spin and creates ferromagnetically aligned domains, which cost significant magnetic energy. With every hopping, the antiferromagnetic pattern is increasingly destroyed. The delocalization of the hole competes with the magnetic background.

1.2.3 Magnetic polaron

The search for a solution to a single doped hole in a Mott insulator has challenged theorists for years and lead to a vast number of publications, all considering the single-hole problem [101–107]. By now a thorough theoretical understanding of the expected behavior has emerged. The doped hole is expected to form a magnetic polaron. A constant bubble, also called dressing cloud, of reduced antiferromagnetic alignment surrounds the hole at all times. The dressing cloud has a finite size, in which the hole can move around. Both together form a quasiparticle, called the magnetic polaron.

The magnetic polaron has renormalized properties compared to the bare hole. When a bare hole moves around, it can do so on a timescale $1/t$. For the polaron to move, the dressing cloud has to be dragged along through the system, which requires the superexchange process to flip spins. Therefore the timescale for polaron motion is expected to be of order $1/J$. A strong indication for the existence of magnetic polarons in cuprates was therefore the observation that the single-particle bandwidth W for excitations in parent compounds is strongly suppressed [24, 108]. Instead of the non-interacting bandwidth $W \sim 8t$, it was found $W \sim 2J$. This is consistent with the
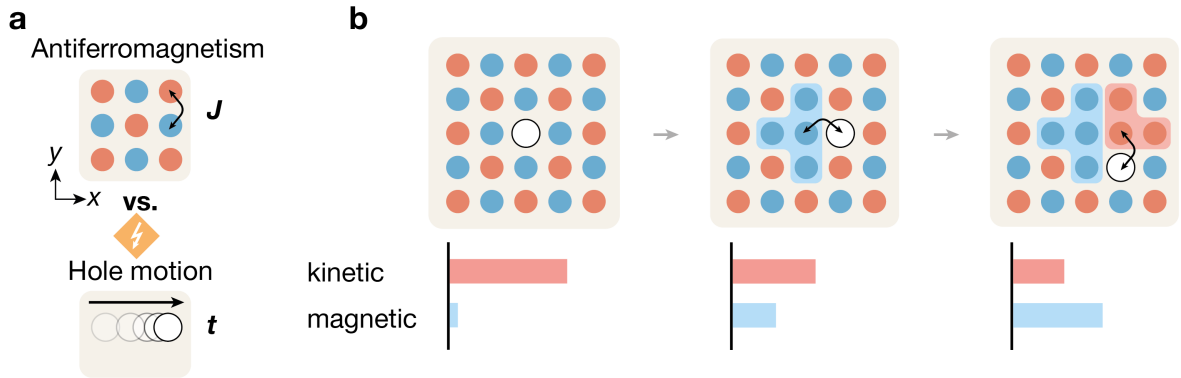
Figure 1.4: Competition between magnetic and kinetic energy. a, The antiferromagnetic processes of the Mott insulator (energy J) compete with the delocalization (energy t) of a hole (more generally: a dopant). **b,** When a hole hops in an antiferromagnetically aligned system, it creates ferromagnetic domains (shadings). With every hopping event, the magnetic cost grows until the lowering of kinetic energy through delocalization is not favorable anymore. For a single hole in an antiferromagnetic environment, a magnetic polaron is expected to form.

bandwidth of magnetic polarons in the t-J model [24].

The size of the dressing cloud scales only weakly with interaction strength U/t, which effectively changes the ratio t/J. Based on semi-classical considerations [97], the polaron size increases with stronger interactions like $\sim (t/J)^{1/4}$. An additional property of the dressing cloud is its inner structure of correlations. Far away from the hole, antiferromagnetic spin correlations remain unharmed. But close to the hole, right in the epicenter of the dressing cloud, how do spin correlations behave? Nagaoka showed, in the infinite U/t limit the dressing cloud can become ferromagnetic [109]. Since in this limit the polaron size also becomes infinite, this means the hole turns the entire system ferromagnetic. The inner structure and size of the magnetic dressing for finite U/t will be probed experimentally in chapter 3.

Directly imaging the magnetic dressing of holes remains elusive in solid-state experiments. Fully resolved snapshots of cold-atom quantum simulators are an ideal basis to search for such entities.

1.2.4 The fate of polarons

When two or more holes are doped into a Mott insulator, the physics becomes significantly more complex. Already the problem of exactly two doped holes challenges theorists to date. Intuitively, it could be energetically beneficial to share the same dressing

cloud to minimize the overall destruction of the antiferromagnetic background. This effect could lead to an attractive interaction between polarons, which is mediated by the antiferromagnetic background correlations. Such a scenario might favor binding of two holes, which are then glued together through their magnetic environment [30, 110–112].

In conventional superconductors, a weak attraction between fermions is mediated by phonons and superfluidity emerges simultaneously with the formation of Cooper pairs, according to Bardeen-Cooper-Schrieffer (BCS) theory [113]. In the Hubbard model, attraction of holes could be strong and Cooper pairs could form before superconductivity sets in, thus being closer to the Bose-Einstein-Condensate (BEC) limit of superfluidity. Pre-formed pairs existing at temperatures well above T_c are often considered as a possible explanation for the pseudogap phenomenon [30]. Only once the temperature reaches T_c, phase coherence is established between bound pairs. The BCS (weakly bound pairs) and BEC (strongly bound pairs) limit as well as their crossover is deeply connected to the high-T_c problem and is studied beyond the Hubbard model [66, 114].

Recent numerical studies of two holes confirm the presence of a binding mechanism in the t-J model even at elevated temperatures [112]. Nonetheless, a microscopic observation of hole attraction or a detection of polaron interactions as a precursor is lacking. The battle between antiferromagnetic correlations and hole motion is expected to dominate the physics up to a certain hole concentration. The phase diagram of the 2d Fermi-Hubbard model is not fully known but is believed to feature similar phenomena as found in copper oxides [115]. A conjectured phase diagram is shown in Fig. 1.5. Magnetic polarons constitute the onset of an anomalous metallic regime, which has clearly observable pseudogap features already at intermediate temperatures $T \sim 0.2t$ [116–118]. A conventional Fermi liquid form once the system is dilute enough, but the specific doping value δ_{FL} for this crossover and its microscopic details are not well known. At much colder temperatures, many different collective phenomena can emerge. Among superconductivity [119], charge-density wave (stripe) states are very close in energy [120]. Which of these eventually forms the ground state is an open debate, which is heavily influenced by next-nearest-neighbor hopping [121]. The temperature scale for such collective behavior appears to be $T \sim 0.02t$ [119].

There exist many proposed concepts for the poorly understood weak to intermediate doping regime, which all try to capture and model different mechanisms [7, 14, 41, 107, 122–124]. Some of the ones compared to the work in this thesis are described in the next paragraph. The magnetic polaron concept is expected to break down eventually with increasing doping. But how exactly do polarons dissolve? Are interaction processes between polarons involved? At what doping does the breakdown happen and does it coincide with δ_{FL}? How do microscopic correlations evolve
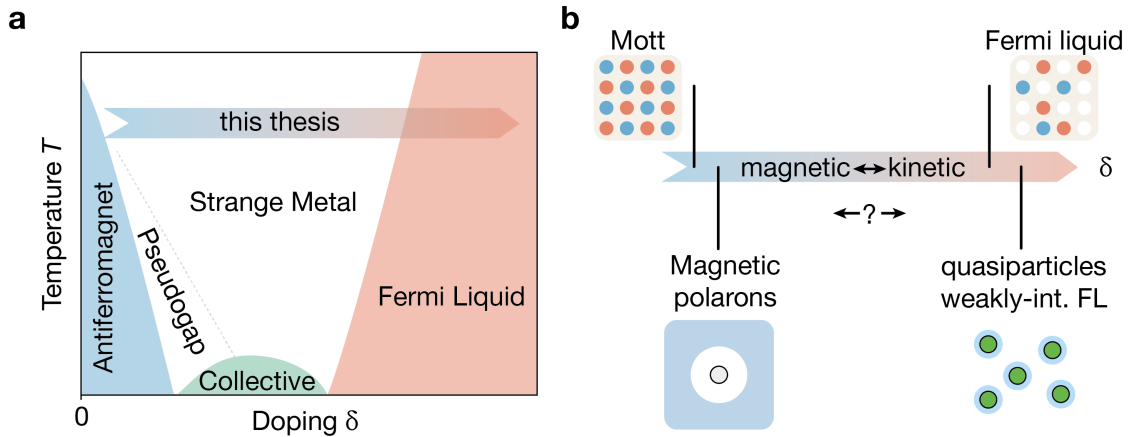
Figure 1.5: Anomalous and normal metals in Fermi-Hubbard systems. a, Conjectured phase diagram of the 2d Hubbard model as a function of temperature and doping. It is more accurate to speak of crossovers than of phases, due to the Mermin-Wagner theorem, see text. Close to zero temperature, various collective effects, such as stripes or d-wave superconductivity can emerge. Between Mott insulator and Fermi liquid anomalous metallic states are realized at intermediate temperatures. **b**, Many open questions on the connection from Mott insulator to Fermi liquid as a function of doping remain. This thesis reports on the evolution of spin-charge correlations as a function of doping at temperatures around the superexchange energy J.

and what happens to the dressing cloud of polarons? All these points are essential questions towards understanding the crossover from anomalous metal to Fermi liquid and are deeply linked to the high-T_c puzzle. Chapter 4 explores these questions and furthermore finds a change across all measured observables around $\delta_{\mathrm{FL}} \sim 30\,\%$.

1.2.5 Weak doping physics - possible concepts

An important part of the high-T_c puzzle is the quest for a simplifying effective description of weak-doping phenomena in Fermi-Hubbard systems. Two approaches are presented below. Quantum simulation with cold atoms (as presented in one of the next sections) offers an ideal testbed with novel observables for these and other theoretical concepts.

Resonating valence bond

The ground state of the 2d Heisenberg model has a large overlap with a classical Néel spin order [125], which is a perfect alternation between up and down spins. Ander-

son introduced a spin liquid state as another possible ansatz to minimize the energy cost of antiferromagnetic spin couplings [41]. This so-called resonating-valence-bond (RVB) state is a superposition of spins forming spin-singlet pairs. The two spins of a singlet can be nearest neighbor, or very far apart. While at half filling a Néel state is more likely, doping might favor such a short-range correlated spin-liquid state [14]. In the RVB state, holes could move through the sea of singlets and shuffle individual spins around without paying a magnetic energy cost. The formation of local singlets could explain the spin susceptibility behavior in the pseudogap regime [14], but the existence of such a spin liquid remains unclear. The spin liquid concept has proven to be fertile ground and different variations RVB states exist [14]. In chapter 4, we benchmark the microscopic correlations of two popular incarnations - uniform [126] and π-flux [127]- with our experiment. The agreement is limited to two-point correlations. In particular higher-order correlations of the experiment reveal discrepancies with uniform and π-flux RVB correlations.

String

An effective model for magnetic polarons assumes that a polaron is a bound state between two fractionalized entities, called spinon and holon [107, 128]. These two partons are bound together by a string of reshuffled spins, hence the name string model. While numerical calculations of the Fermi-Hubbard model with a single hole can only diagnose the existence of the polaron, the string model casts the problem into a simplified effective Hamiltonian [72, 107]. It can therefore make predictions even in the presence of multiple holes, by assuming the formation of independent polarons. Furthermore, the string model predicts a rich inner structure of the magnetic polaron, with possible rotational and vibrational excitations akin to states found in high-energy physics. The intuition behind the string picture can be understood with Fig. 1.4. When a hole starts moving, it leaves behind a string of reshuffled spins, which connect the hole to a spin excitation (spinon) it leaves behind at its initial position. The bound object of hole (in this case holon) and spinon corresponds to the magnetic polaron. The average string length (related to the polaron size) is determined by the antiferromagnetic correlation strength and the ratio of t/J. The hole can therefore not leave the vicinity of the spinon, and the center of mass of both can only move once the spinon moved (requiring spin flips at timescale $1/J$). The holon surrounds the spinon like an electron surrounds the proton in a hydrogen atom. In the reference frame of the hole, spin correlations are therefore on average reduced in its vicinity in all directions because in every realization the spinon and string are found in a different configuration. In our benchmark (chapters 3 and 4), experimental spin-charge correlations and the string model show decent qualitative similarities in the single-dopant regime, but only limited agreement for dopings approaching δ_{FL}.

1.3 Cold atoms - quantum simulation

Since the advent of laser cooling and Bose-Einstein condensation of neutral atoms in the 1990s [129–131], generating degenerate cold-atomic Fermi gases at low temperatures down to $T/T_{\mathrm{F}} \sim 0.05$ has become a reality [132]. Instead of electrons, the fermions, in this case, are fermionic atoms, such as ^{40}K or ^{6}Li, with recent additions to the portfolio being fermionic alkaline-earth [133] or erbium [134] atoms. The hyperfine states of neutral atoms can play the role of the spin of electrons. Based on optical lattices and ultracold collisions, clean implementations of Fermi-Hubbard systems can be created from scratch within $\sim 20\,\mathrm{s}$ in such laboratories [40, 135, 136]. The analogy to condensed matter systems is summarized in Fig. 1.6. Around 2010, major advances in microscopy and imaging techniques of these atomic gases enabled taking pictures of strongly-correlated bosonic systems with single-particle resolution [46, 47]. These microscopy techniques could be extended to fermionic gases in 2015 [49–53]. These breakthroughs started an era, in which higher-order non-local real-space correlations can directly be probed in quantum matter [57, 137–139]. An important difference between electronic and cold-atomic systems is the energy scale. Lattice spacings are much larger and dynamical timescales slower, allowing unprecedented measurements with cold atomic systems, such as tracking the dynamical time evolution upon a quench [140, 141]. As a trade-off, the Fermi temperature T_{F} is 10^{10} times smaller than for electrons, requiring setups to reach some of the coldest temperatures accessible on earth.

1.3.1 Optical lattice and ultracold collisions

The optical dipole force is an essential ingredient for manipulating cold atoms [135, 142]. An oscillating electric laser field of intensity I couples to the outer electron of a neutral atom, described by a dipole coupling. When the oscillation frequency ω_{L} of the laser is off-resonance by a detuning Δ from an electronic transition of the atom at angular frequency ω_0, an actual excitation of the electron is strongly suppressed. Nonetheless, the absolute energy of the electronic transition is changed by the presence of off-resonant light, referred to as light shift. A spatially varying intensity of the light $I(\boldsymbol{r})$ therefore creates an optical potential $V(\boldsymbol{r})$ for the atom, given by

$$V(\boldsymbol{r}) = \frac{3\pi c^2}{2\omega_0^3} \frac{\Gamma}{\Delta} I(\boldsymbol{r}) \ , \tag{1.3}$$

where c is the speed of light and Γ the natural linewidth of the transition. When the laser frequency $\omega_{\mathrm{L}} < \omega$ (red detuned), the potential is attractive and for $\omega_{\mathrm{L}} > \omega$
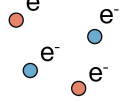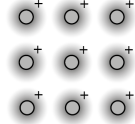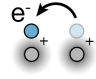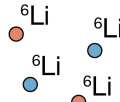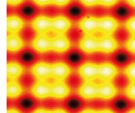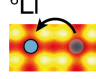
Condensed matter $(T_F \sim 5000\ K)$	electrons	ionic lattice	$t/h \sim$ THz	Coulomb
Fermi-Hubbard	fermions spin 1/2	2d lattice structure	hopping t	interaction U
Cold atoms $(T_F \sim 300\ nK)$	neutral atoms	optical lattice (tunable)	$t/h \sim 0.1$-1 kHz (tunable)	on-site collisions (tunable)

Figure 1.6: Real and synthetic electronic systems. The simplest approximation of copper oxides is the 2d Fermi-Hubbard model. Material parameters for nearest-neighbor hopping amplitude t and an effective screened on-site Coulomb repulsion U can be estimated from experimental measurements. Finite next-nearest-neighbor and diagonal hopping amplitudes exist in cuprates (relevant for some phenomena [121]) but are neglected in the simplest version of the Hubbard model. Cold-atoms can be used to implement fully tunable versions of Hubbard systems. Neutral atoms (here ^6Li) emulate the behavior of electrons.

(blue detuned) repulsive. The residual off-resonant scattering rate Γ_{sc} is given by

$$\Gamma_{sc}(\boldsymbol{r}) = \frac{3\pi c^2}{2\hbar\omega_0^3}\left(\frac{\Gamma}{\Delta}\right)^2 I(\boldsymbol{r}). \tag{1.4}$$

Both Eq. 1.3 and 1.4 are valid for two-level systems. In principle, atoms are much more complex, giving rise to vector- or more general tensor-light shifts [143], allowing for the generation of fictitious magnetic fields [144] and spin manipulation techniques [145]. Such advanced schemes are mostly not applicable to ^6Li, due to its small fine structure splitting. For ^6Li, laser light needs to be close to resonance to generate significant vector light shifts, which leads to strong off-resonant heating. By interfering two laser beams of wavelength λ, a spatial lattice can be created. The spacing a of this

lattice depends on the angle α between both beams

$$a = \frac{\lambda}{2} \frac{1}{\sin(\alpha/2)}. \tag{1.5}$$

The second important ingredient to cold-atom quantum simulation are atom-atom collisions. At temperatures below quantum degeneracy, most of the time only head-on s-wave collisions are relevant [132, 135]. Thus, opposite spins interact via such collisions, while same-spin fermions become non-interacting (s-wave collisions are strongly suppressed). The interaction can effectively be described by a contact potential with scattering length a_{sc}. The strength of this effective parameter is rooted in the physics of inter-atomic bound states, details can be found e.g. in [132]. When the binding energy is brought into resonance with the kinetic energy of both particles, a_{sc} diverges. This phenomenon is called Feshbach resonance. Whenever the energy of the underlying bound state can be tuned with an external parameter, the effective interaction can be tuned. For ^{6}Li, the scattering length can be readily tuned with a magnetic bias field and Feshbach resonances around $800\,\text{G}$, see chapter 2.

Combining an optical lattice potential and opposite-spin collisions, the Hamiltonian for two opposite-spin particles with position and momenta (x_i, p_i) becomes [146]

$$\mathcal{H} = \sum_i \left(V_0 \cos^2\left(\frac{\pi x_i}{a}\right) + \frac{p_i^2}{2m} \right) + \frac{4\pi \hbar^2 a_{sc}}{m} \delta(x_1 - x_2). \tag{1.6}$$

The optical lattice introduces a new energy scale, which is the recoil energy

$$E_R = \frac{h^2}{8ma^2}. \tag{1.7}$$

The potential depth of the lattice is typically measured in units of E_R. When the lattice is sufficiently deep $V_0 > 5\,E_R$, Eq. 1.6 can be expressed in terms of Wannier functions, which are states localized at individual lattice sites. In this tight-binding limit and using the many-body notation with operators $\hat{c}_i^\dagger$ creating a fermion in a Wannier state at site i., Eq. 1.6 turns into the Fermi-Hubbard Hamiltonian. The nearest-neighbor tunneling amplitude and on-site interaction are then given by [146] (deep lattice limit $V_0 \gg E_R$)

$$\frac{t}{E_R} \simeq \frac{4}{\sqrt{\pi}} \left(\frac{V_0}{E_R}\right)^{3/4} \exp\left(-2\sqrt{\frac{V_0}{E_R}}\right) \tag{1.8}$$

and

$$\frac{U}{E_R} \simeq \sqrt{8\pi} \frac{a_{sc}}{a} \left(\frac{V_0}{E_R}\right)^{3/4}. \tag{1.9}$$

The precise control of laser power, Feshbach resonances and total number of particles allows cold-atom simulators to explore Fermi-Hubbard physics with full tunability of hopping, interaction and doping. The dimensionality of atomic systems can furthermore be varied by individual adjustment of laser power along the three spatial dimensions. Different lattice geometries, such as honeycomb [147] or kagomé [148], are accessible by generating different interference patterns. In particular, superlattice structures can be engineered [149], which will be used as a powerful tool in the following chapters.

1.3.2   Quantum gas microscopy

Since lattice spacings for cold atomic systems are on the scale of optical wavelengths, very high numerical aperture (NA) objectives can be used to achieve optical resolution of individual lattice sites. To take a photograph of a lattice gas, atoms are pinned with a very deep lattice at maximal available laser power. Atoms are exposed to resonant light, which makes them start to scatter fluorescence photons. To keep the atoms pinned during the fluorescence process, active cooling needs to be provided. An efficient cooling scheme is Raman sideband cooling, as used in most fermionic microscopes [49–51, 150]. The resulting single-site resolved snapshot measures the occupation on each lattice site, see Fig. 1.7 for a fermionic Mott insulator. Taking such a snapshot collapses the many-body wavefunction. Taking photos of many realizations therefore allows a complete and model-independent characterization of the underlying quantum state.

There are two constraints of traditional quantum gas microscopy. The spin of a fermion is not detected with the method mentioned above. Push-out schemes can be implemented [54, 55], but then only information of a single spin species can be revealed within the same shot. Furthermore, the density information in most experiments is not accurate, due to light-assisted collisions. Double occupations are lost during imaging and show up as holes, referred to as parity projection [46, 47]. This renders doublons and holes indistinguishable in traditional quantum gas microscopy. The lack of spin-resolution and parity projection are major obstacles when trying to unravel the intricate interplay of spins and doped holes or doublons in the Fermi-Hubbard model.

The MPQ machine overcomes both problems, i.e. parity projection [49] and spin resolution [56, 71]. The technique currently used for spin resolution was developed in this work and is presented in chapter 2. Measurements featured within this thesis were therefore performed with full spin- and density-resolution, referred to as *full resolution*.
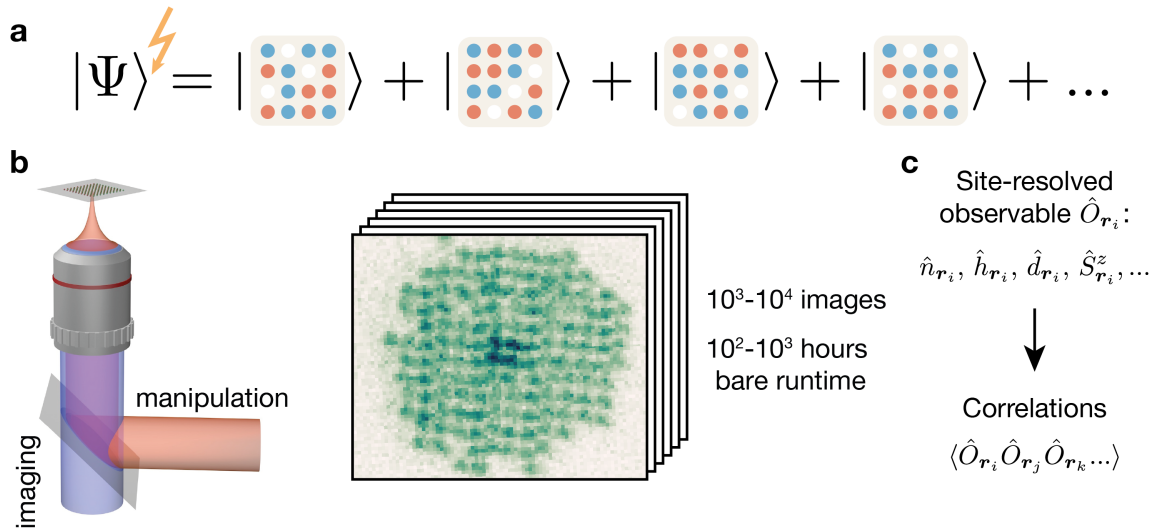
Figure 1.7: Quantum gas microscopy. a, Once the quantum state is prepared, taking a real-space snapshot of the system collapses the wavefunction onto the Fock basis of the lattice sites. **b**, Using a high-resolution objective, single-site resolved snapshots of thousands of realizations are taken. Each snapshot requires a new preparation of the quantum system. **c**, Through advanced techniques, all local spin and density observables can be measured in each shot. Based on such full resolution, multi-point correlations between spins and charges (density) can be studied in the system.

1.4 Correlators

Analyzing correlations is a fundamental tool across many disciplines. When two quantities are correlated, knowledge of one component allows the inference of the most probable state of the other. This can be used in modern data science to build predictive models. In quantum-many-body physics, correlations allow researchers to explore the statistical connections and the inner structure of the underlying wavefunction, without having to note down the actual wavefunction [151–153]. A quantum state can be fully characterized by its correlations [151]. In fact, linear-response functions of a material are directly linked to microscopic two-point correlations in the system through the fluctuation-dissipation theorem [9]. Correlators of particular importance to the doped Fermi-Hubbard model are correlations between dopants (e.g. holes) and spins. Such spin-charge correlations will be the main topic of chapters 3 and 4. This section introduces a visual representation of spin correlations and how they can be normalized. The very important concept of connected and disconnected parts is explained as well as the relation between two-point spin correlations and spin

structure factor or susceptibility.

1.4.1   Correlators and normalization

N-point correlations are the expectation value of the product of N observables $\hat{O}_i$, such as $C = \langle \hat{O}_1 ... \hat{O}_N \rangle$. One of the simplest and intuitive correlators is a spin-spin correlator, which compares the mutual alignment of spins at two different positions

$$C(\boldsymbol{r}_1, \boldsymbol{r}_2) = \eta \langle \hat{S}^z_{\boldsymbol{r}_1} \hat{S}^z_{\boldsymbol{r}_2} \rangle \ . \tag{1.10}$$

To be able to compare different correlations quantitatively, a correlator needs to be normalized with an appropriate factor η.

In statistics, the Pearson Correlation Coefficient (PCC) [154] is commonly used to quantify the linear correlation between two random variables A and B. The PCC is given by $C(A, B) = \text{cov}(A, B)/\sigma(A)\sigma(B)$. The bare covariance $\text{cov}(A, B)$ is normalized to the product of standard deviations $\sigma(A)\sigma(B)$. The intuition behind this normalization is simple: the strength of the combined fluctuation is compared to the independent fluctuations of both variables. The PCC therefore takes values between -1 and 1, which correspond to maximum possible negative or positive correlation. In analogy to the PCC, the normalization η should be

$$\eta_{\text{Pearson}} = 1/\sigma(\hat{A})\sigma(\hat{B}) = 1/(\sqrt{\langle \hat{A}^2 \rangle - \langle \hat{A} \rangle^2} \sqrt{\langle \hat{B}^2 \rangle - \langle \hat{B} \rangle^2}) \ . \tag{1.11}$$

The PCC normalization is not always directly used for correlations in physics. For spin-spin correlations, a common choice of normalization is $\eta_{\text{Heis}} = 4$. In the context of a spin-1/2 Heisenberg model, this is equivalent to the PCC, since $\sigma(\hat{S}^z_i) = 1/2$. But for the Hubbard model at finite interaction strength and in particular for doped systems $\sigma(\hat{S}^z_i) < 1/2$, because empty or doubly-occupied sites contribute zero spin ($\hat{S}^z_i = 0$). If the Heisenberg normalization η_{Heis} were to be used for doped systems, the maximum possible strength of spin correlations would be $C_{\text{max}} < 1$. Only with η_{Pearson} the maximum correlation strength is always $C_{\text{max}} = 1$. Therefore, the PCC normalization ensures that correlation values can be quantitatively compared between different systems, because $C = 1$ universally means maximal possible correlation.

For instance, consider a heavily doped system in which the spin of a lattice site $\hat{S}^z_i$ fluctuates very little around zero ($\sigma(\hat{S}^z_i) \ll 1/2$) because a spinful particle only very rarely occupies that site. Nonetheless, spinful particles in the strongly doped system might still be maximally correlated. If e.g. spin fluctuations on two sites in such a system are maximally negatively correlated, a correlator normalized with η_{Pearson} would measure the value -1. This is not the case with $\eta_{\text{Heis}} = 4$.

a

b
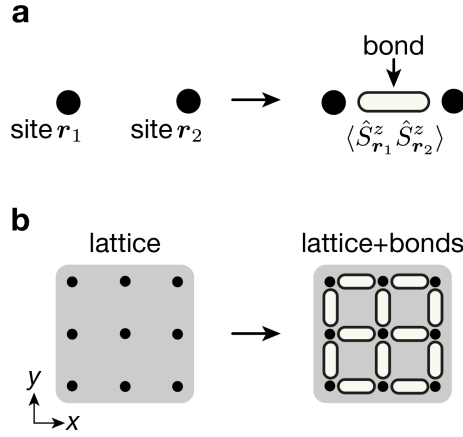
Figure 1.8: Visualizing spin correlations. a, The correlation of spins between two lattice sites r_1 and r_2 can be visualized by a colored bond connecting both sites. The color (here white) will be used to indicate the sign and strength of the measured correlation. **b,** Spin correlations between all lattice sites can be visualized in the bond picture. Here only NN correlations ($d = 1$) are shown.

Throughout this thesis the applied normalization - η_{Heis} or η_{Pearson} - will be indicated.

1.4.2 Visualization - bond picture

In a homogeneous translation-invariant system comprising Ω lattice sites, spin-spin correlations at fixed distance $d = r_2 - r_1$ are the same everywhere in space. The correlation can be represented with a single value, which is the average (assuming periodic boundaries for simplicity)

$$C(d) = \sum_{r_1 \in \Omega} C(r_1, r_1 + d)/\Omega \ . \tag{1.12}$$

In inhomogeneous systems, or more importantly, in the reference frame of a dopant or magnetic polaron, correlations at fixed d can vary in space, as will be seen in chapter 3 and 4. It is therefore desirable to have a visual representation of spin-spin correlations in real space. Our way of plotting correlations relies on the bond picture, which was already invoked in previous numerical work [111]. As shown in Fig. 1.8, the correlation strength between two sites is indicated by the color of a bond connecting both sites. We also refer to this as the *bond strength*. The distance between both sites is referred to as the *bond length*. Extending this concept to the entire lattice allows a representation of correlations at fixed d in the system. For $d > \sqrt{2}$ the visualization becomes increasingly difficult, due to the overlapping of different bonds.

1.4.3   Connected and disconnected parts

Strictly speaking, the bare object $\langle \hat{O}_1 ... \hat{O}_N \rangle$ does not measure the *correlation* directly [155]. More accurately, $\langle ... \rangle$ is called a *moment*. It is the *cumulant*, which contains the information about correlation. The careful reader might already have noticed, the PCC introduced above also defines a correlation through the covariance between two observables, which in this case is the same as the cumulant. Therefore, a correlation between N observables can formally be defined as

$$C(\hat{O}_1, ..., \hat{O}_N) = \eta_{\text{Pearson}} \langle (\hat{O}_1 - \langle \hat{O}_1 \rangle)...(\hat{O}_N - \langle \hat{O}_N \rangle) \rangle \ . \tag{1.13}$$

A key difference between the bare moment $\langle ... \rangle$ and this definition of correlation is that the moment of order N can be nonzero, while there is zero correlation between the observables. Such a situation can e.g. arise when the mean of individual observables is nonzero, which can cause a finite moment of order N in the absence of a correlation.

However, in colloquial physics language (and also for the rest of this thesis), the word *correlation* is often used in reference to bare moments, which are then called *bare correlations*. As a consequence of this choice of language (to which we adhere in this thesis), special care needs to be taken concerning the origin of a correlation under investigation.

The bare correlation of order N can be decomposed into two parts: a combination of correlations arising from lower-order moments, referred to as disconnected part, and the actual correlation, also referred to as the connected part. In this context, cumulant, connected part and Eq. 1.13 denote the same object. Throughout this thesis, bare moments are therefore considered a correlation C and we use the concept of connected and disconnected parts to distinguish between true correlation effects C^c of order N and correlations arising from lower-order contributions C^d [151]

$$C = C^c + C^d \ . \tag{1.14}$$

The concept of connected and disconnected part is best illustrated with an example for the two-point spin correlator discussed before, see Eq. 1.10. Let us take a fully magnetized spin system, such that $\langle \hat{S}_{r_i}^z \rangle = 1/2$ on every lattice site, see Fig. 1.9. The bare spin-spin correlator (for the sake of simplicity we consider a constant normalization $\eta = 4$) measures a maximum correlation value of $+1$ between lattice sites. But this bare correlation is fully determined by the disconnected part, which is $C^d = \eta \langle \hat{S}_{r_1}^z \rangle \langle \hat{S}_{r_2}^z \rangle = 1$. The connected part, measuring the actual correlation of order two, is given by

$$C^c = C - C^d = \eta \langle \hat{S}_{r_1}^z \hat{S}_{r_2}^z \rangle - \eta \langle \hat{S}_{r_1}^z \rangle \langle \hat{S}_{r_2}^z \rangle \ . \tag{1.15}$$

Sample system	bare $\langle \hat{S}^z_{\boldsymbol{r}_1} \hat{S}^z_{\boldsymbol{r}_2} \rangle$	disc. $\langle \hat{S}^z_{\boldsymbol{r}_1} \rangle \langle \hat{S}^z_{\boldsymbol{r}_2} \rangle$	conn. $\langle \hat{S}^z_{\boldsymbol{r}_1} \hat{S}^z_{\boldsymbol{r}_2} \rangle - \langle \hat{S}^z_{\boldsymbol{r}_1} \rangle \langle \hat{S}^z_{\boldsymbol{r}_2} \rangle$
Classical Ferromagnet (polarized+)			
Antiferromagnet			
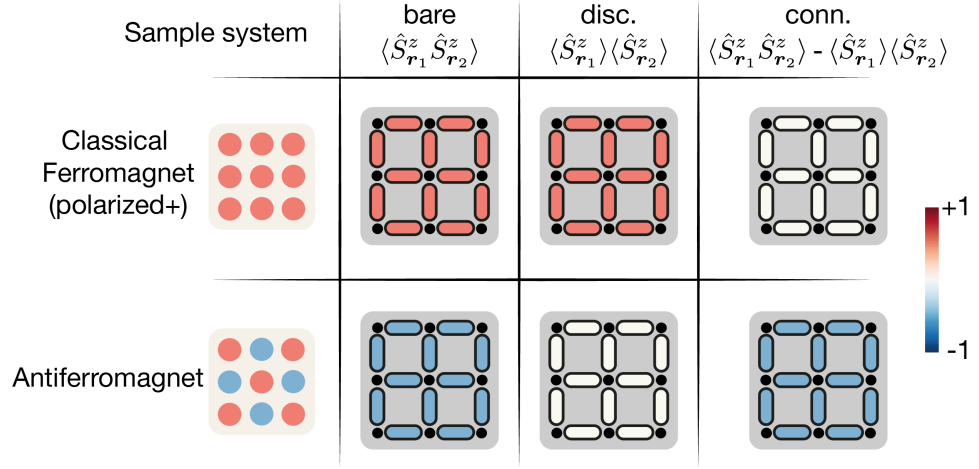
Figure 1.9: Connected and disconnected parts. Bare correlations are always composed out of disconnected contribution from lower-order terms and the connected higher-order correlation. This concept is demonstrated with NN two-point spin correlations for two states. A balanced spin mixture with antiferromagnetically aligned spins has no disconnected contribution to spin correlations. In the (polarized) classical ferromagnet shown, all bare spin correlations originate from the presence of finite magnetization.

In the scenario of a magnetized system, no actual two-point correlation between the lattice sites exists and $C^c = 0$. For spin-balanced antiferromagnetic spin systems investigated in this thesis $\langle \hat{S}^z_{\boldsymbol{r}_i} \rangle = 0$, which means the disconnected part for spin-spin correlations is zero.

In particular, when investigating higher-order spin-charge correlators, it will be important to distinguish the connected and disconnected contribution to the bare correlation value.

1.4.4 Conditional correlations

Another type of correlations are correlations conditioned on a certain event. An example is the spin correlation between two sites $\boldsymbol{r}_1$ and $\boldsymbol{r}_2$, conditioned on detecting a hole at a third site $\boldsymbol{r}_3$. The probability of detecting a hole at $\boldsymbol{r}_3$ is given by $\langle \hat{h}_{\boldsymbol{r}_3} \rangle$, where $\hat{h}_{\boldsymbol{r}_3}$ denotes the hole-density operator on that site. The conditional probability for A, given B, can be expressed as $P(A|B) = P(A \cap B)/P(B)$ [154]. Following this logic, the spin-spin correlation in the presence of a hole can be expressed as

$$C(\boldsymbol{r}_1, \boldsymbol{r}_2)_{\circ_{\boldsymbol{r}_3}} = \eta \langle \hat{S}^z_{\boldsymbol{r}_1} \hat{S}^z_{\boldsymbol{r}_2} \hat{h}_{\boldsymbol{r}_3} \rangle / \langle \hat{h}_{\boldsymbol{r}_3} \rangle \ . \tag{1.16}$$

Here, the expectation values $\langle ... \rangle$ are taken with respect to all shots. This correlator is an example of a three-point correlator. Based on real-space snapshots of the system, an alternative algorithm to compute this correlation is by applying a post-selection on the data. In this case, first the data is post-selected to snapshots with $\hat{h}_{r_3} = 1$. Then $C(r_1, r_2)$ is computed. Both routes are equivalent. Such conditional correlations will play an important role in chapters 3 and 4.

1.4.5 Structure factor and susceptibility

The knowledge of two-point correlations in the system can be used to reconstruct macroscopic quantities.

The static spin-structure factor $S(q)$ is an observable, which measures the different wavevectors q present in spin patterns emerging in the system [9]. $S(q)$ corresponds to the Fourier transform of two-point spin correlations

$$S(q) = \sum_{r_i \in \Omega} \sum_{d=0}^{\infty} \langle \hat{S}_{r_i}^z \hat{S}_{r_i+d}^z \rangle e^{iqd} / \Omega \; , \tag{1.17}$$

where Ω denotes the number of lattice sites in the system. Here we consider a system in the thermodynamic limit $\Omega \to \infty$, such that finite size effects can be neglected. Strong antiferromagnetic correlations at half filling lead to a staggered spin pattern, which has a wavevector $q_{\mathrm{AFM}} = (\pi, \pi)$, where the lattice spacing set to one.

In solid-state systems, the spin-structure factor can be measured by neutron scattering [156]. With a quantum gas microscope, this quantity can be directly computed from fully-resolved snapshots. Other static structure factors, such as the ones for charges or only holes, can be evaluated in a similar manner.

The uniform spin susceptibility χ_{s} was already mentioned in the first section of this chapter as an observable detecting pseudogap features. It is a response function, which measures how spins in the system respond to a weak homogeneous ($q = 0$) magnetic field (linear-response regime). The fluctuation-dissipation theorem links the susceptibility to two-point correlations in the equilibrium unperturbed system [9], i.e. application of a magnetic field is not required,

$$\chi_{\mathrm{s}}(q = 0) = S(0)\, 1/T \; . \tag{1.18}$$

This relation is in general only valid for $q = 0$. In solid-state systems, the spin susceptibility can be determined through Knight-shift measurements with nuclear-magnetic resonance [14]. For quantum gas microscopes, this quantity can be obtained from the sum of all two-point spin correlations. As a consequence, $S(0)$ cannot be determined accurately when the correlation length approaches the system size, which is not the case in this thesis.

2 |

A bilayer quantum gas microscope

This chapter covers the experimental setup. Recent upgrades are described in detail, which concern the engineering and implementation of a highly-stable bichromatic superlattice in the vertical direction. Precise control over this superlattice enables efficient bilayer microscopy. Two applications are demonstrated, the microscopy of bilayer Fermi-Hubbard systems and full spin- and density-resolution for monolayer systems. Results of the following publication are contained in this chapter:

- **Robust bilayer charge pumping for spin- and density-resolved quantum gas microscopy**.
  J. Koepsell, S. Hirthe, D. Bourgund, P. Sompet, J. Vijayan, G. Salomon, C. Gross and I. Bloch. Physical Review Letters **125**, 010403 (2020).

2.1   Experimental setup

The operation of this cold-atom experiment can be divided into three steps: preparation, simulation, detection. A full cycle through all three steps takes on the order of $\sim 20\,\text{s}$. Every new experimental snapshot requires the full procedure.

The preparation part concerns the production of a trapped 2d or 3d gas at the lowest reachable temperature. Around 80 % of the cycle time of our machine is currently dedicated to the production of such a gas, which is achieved by a combination of laser and evaporative cooling.

The simulation step generally consists of loading the cold gas into a controlled environment, which realizes a desired Hamiltonian for the system. In our case, atoms are exposed to an optical lattice, which is adiabatically turned on and ramped to the desired simulation parameters. In some experiments, the simulation part contains a dynamic quench of the system and a variable time evolution.

Detection in this thesis involves three components. At first, the system is rapidly frozen in the optical lattice, followed by a sequence to encode spin information into a spatial degree of freedom. Then single-site resolved images are taken.

The main apparatus was constructed by the previous generation of students and most details of the current setup can be found in their theses [157–159]. Nonetheless, this section covers recently implemented upgrades and reiterates experimental aspects relevant to this thesis.

2.1.1   Preparation of ultracold 2d gases

Lithium

The fermions used in this experiment are ^{6}Li atoms in their electronic ground state. There are a few reasons, why lithium is currently among the most successful atomic species for fermionic quantum simulation. There is the pragmatic fact that the coldest fermionic samples in terms of T/T_F were so far reported with lithium [132]. The limiting factors for lower temperatures are not fully understood and represent one of the greatest challenges for quantum simulation. Furthermore, the light mass of lithium (six atomic mass units) leads to higher energy scales than with other common laser-cooled elements. This allows for faster experiments through rapid thermalization times but also grants better protection against heating from technical noise at low frequencies. Finally, the existence and benign properties (such as low losses and broad lineshape) of Feshbach resonances for lithium make it an ideal choice for experiments with tunable interactions.

Alkali atoms have a hydrogen-like electronic structure with one valence electron, whose D_1 and D_2 transitions are well suited for laser cooling. As shown in Fig. 2.1, these transitions are around $\lambda = 671$ nm for ^{6}Li and have a natural linewidth of $\Gamma = 2\pi \cdot 5.87$ MHz [160]. A magneto-optical trap (MOT) on the D_2 transition produces atomic samples at temperatures $\sim 300\,\mu$K. Further laser cooling is achieved by an ultraviolet (UV) MOT, operating on the $2S$-$3P$ transition at $\lambda = 323$ nm. The smaller linewidth of $2\pi \cdot 754$ kHz of this transition [161] enables cooling to $\sim 60\,\mu$K.

The ratio between fine-structure splitting $\Delta_F \sim 10$ GHz and natural linewidth Γ of the D_1 or D_2 transition is much smaller than for other alkali atoms. This means vector light shifts, i.e. spin-dependent optical potentials, cannot be used for lithium with high fidelity because off-resonant scattering is much higher than with other species.

Hyperfine states of lithium are used to realize pseudospin systems. Throughout this thesis, the lowest states $|1\rangle$ and $|2\rangle$ (i.e. the two $F = 1/2$ states) are used to represent spin-1/2 fermions. Feshbach resonances between atoms in the three lowest hyperfine states are shown in Fig. 2.1b. By applying a magnetic offset field, the scattering length a_{sc} can be tuned to induce strong repulsive interactions. Repumping after laser cooling ensures atomic samples with an equal number of both spin (hyperfine) states, therefore realizing spin-balanced samples.

a

b
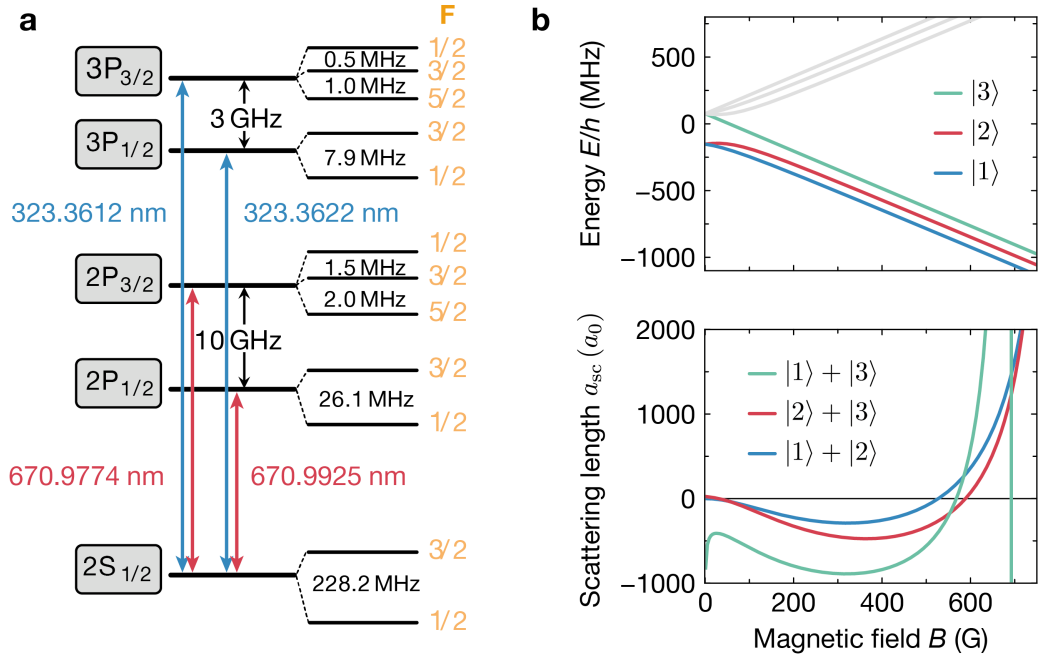
Figure 2.1: Properties of lithium. a, Electronic level structure of fermionic ^{6}Li. Laser cooling is performed on the D_1 and D_2 transitions around $\lambda = 671$ nm and on the narrower ultraviolet transition at $\lambda = 323$ nm. Illustration based on [157]. **b**, ^{6}Li in a magnetic field. A Breit-Rabi calculation of the energy splitting of the lowest hyperfine states is shown in the upper panel. The mutual scattering length between the lowest three states changes in a magnetic field (due to a Feshbach resonance) and is shown in the lower panel (based on data of [162]). Fermi-Hubbard systems are typically realized at high magnetic fields around 650 G, while spin splitting for detection is performed at low fields well below 30 G.

Glass cell

All final steps of the experimental sequence take place in a glass cell with maximal optical access, as shown in Fig. 2.2. The full vacuum assembly, in which cooling and manipulation of lithium atoms take place, can be found in [157]. Pre-cooled spin-balanced atomic samples are transported into this glass cell, by trapping atoms in the focus of a dipole trap and physically moving the focus of this trap into the cell. The atoms are then handed over to a crossed dipole trap, which is projected from the bottom through the microscope objective with numerical aperture (NA) of 0.5. The cross trap uses laser light at $\lambda = 1064$ nm and vertically crosses the horizontal transport beam to provide tight confinement in the xy-plane. In the next step, a strongly-elliptical beam (light sheet) at $\lambda = 780$ nm strongly increases the vertical confinement.
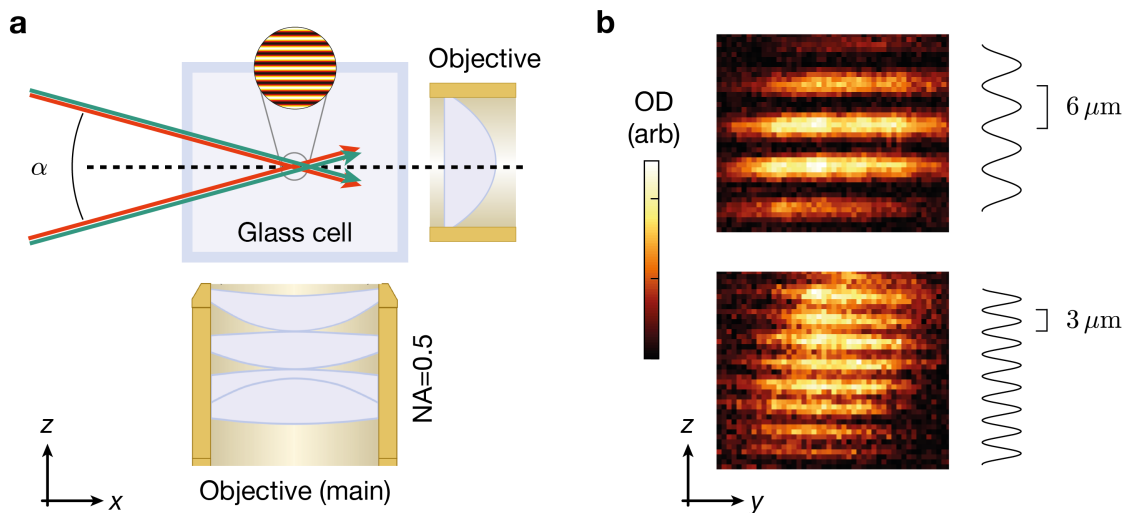
Figure 2.2: Preparation of individual atomic layers. a, At the final stage in the experimental cycle, the atomic cloud is manipulated and detected in a glass cell under ultra-high vacuum. The high-resolution objective (NA= 0.5) is used to take single-site fluorescence images. A lens with a lower resolution is used for absorption imaging from the side. Two different vertical lattices, created by the interference of red or green beams at angle α, can be used to confine atoms in a single two-dimensional layer. **b**, Absorption images from the side, when atoms are loaded into the large-scale (upper panel) or small-scale (lower panel) vertical lattice. By transferring atoms into an elliptical dipole trap prior to lattice loading, all atoms can be prepared in a single layer of the large-scale lattice.

This beam is tightly focused by a lens of focal length $f = 40$ mm from the side, which enables a gaussian waist in the z-direction of $1.7\,\mu$m. The light sheet squeezes the vertical extension of the atomic gas to around $3\,\mu$m.

Loading the vertical lattice

A quasi-2d gas is prepared in the next step. To this end, a vertical lattice with a long spacing $a_z^l = 6\,\mu$m is turned on and adiabatically ramped to a depth of $100\,E_R^l$, where E_R^i is the recoil energy of the respective lattice i. The lattice is created by interfering two beams of $\lambda = 1064$ nm under an angle $\alpha = 10°$, as indicated in Fig. 2.2. Both beams are transmitted through the walls of the glass cell at an angle of $\sim 27°$ in the horizontal plane, which is not visible in Fig. 2.2. If the location of the light sheet falls into a plane of the vertical lattice, atoms are successfully transferred into a single layer. If the light sheet was not used before loading, multiple layers of the vertical lattice are populated, see Fig. 2.2b.

A second vertical lattice with a shorter spacing $a_z^s = 3\,\mu$m can be generated by interfering two beams of $\lambda = 532\,$nm also under an angle $\alpha = 10°$. In fact, the beams for the short and long lattice are overlapped and guided by the same optics in a bichromatic setup. The two commensurable lattices, where $2 \cdot a_z^s = a_z^l$, form a superlattice, which is described in detail in the next section. Once a single layer of the long lattice is loaded, the atoms are transferred into the short lattice by adiabatically increasing the short lattice depth to $50\,E_R^s$ and tuning one of its layers to coincide with the atomic plane. The result is a quasi-2d gas, with a vertical trapping frequency of $12\,$kHz. The radial xy trapping frequency at this point is set to a few hundred Hz by controlling the strength of the cross trap.

Final evaporation

Evaporative cooling is the last preparation step. A strong magnetic gradient along the y-direction tilts the potential experienced by the atoms and allows the hottest particles to escape. The magnetic offset field during the evaporation is $600\,$G and realizes the Paschen-Back regime (decoupling of nuclear spin I and electronic angular momentum J). In this limit, both spin states experience an equal force from the magnetic gradient in the same direction, which preserves the spin balance of the mixture. Once a hot particle is ejected from the cloud, the system re-thermalizes at a colder temperature than before. This re-thermalization process represents a limiting factor for the cooling power of the evaporative process. With decreasing temperature, collisions between same-spin fermions are strongly suppressed and spin-polarized systems stop thermalizing. Even in two-component fermionic mixtures, Pauli blocking leads to a slower thermalization rate at quantum-degenerate temperatures [163]. Eventually, constant heating rates, such as three-body losses or collisions with background particles, become larger than the cooling rate and place a lower bound on the achievable temperatures.

It remains unclear, which aspect represents the limit to currently achievable temperatures. The duration of the final evaporation used in this thesis was $5\,$s and achieves temperatures around $T/T_F \sim 0.1$. It is puzzling that many related lithium-based experiments in research groups end up at similar temperatures [54, 58, 60], despite significantly different optical setups and evaporation sequences. A promising route for reaching lower temperatures is sympathetic cooling with another, ideally bosonic, species [164]. Unfortunately, the complexity of experiments with multiple species increases significantly. The quest for colder samples is therefore more easily tackled with other means, such as entropy redistribution [61, 165, 166].

2.1.2   Lattices for simulation and detection

Physics lattice

Fermi-Hubbard systems are realized, by exposing the quasi-2d cold gas to an optical lattice along the xy-direction. Such an in-plane lattice is created by interfering two $\lambda = 1064\,$nm beams for the x- and y-lattice respectively. The angle of interference is chosen to obtain a lattice spacing of $a = a_x = a_y = 1.15\,\mu$m. All laser beams for the xy-lattice are sent to the atoms from the bottom through the main microscope objective. Projecting the lattice through such high NA optics has the advantage of a very high positional stability of the laser beams on the atoms. On the other hand, the high-resolution optics leads to corrugations of the optical potential on the atoms. These defects most likely originate from defects on the optical elements (such as dust or microscopic scratches on mirrors) before the objective and are imprinted onto the optical potential by the high optical resolution. Careful cleaning of the optical path keeps such defects at a minimum in this setup. Nonetheless, to fully mitigate such problems in the potential landscape a new xy-lattice generation is currently being designed.

In a typical procedure, the xy-lattice is turned on and linearly ramped to a final depth of $\sim 7\,E_{\mathrm{R}}^{xy}$, such that the tight-binding limit is realized. The ramp duration is usually chosen to be 100 ms. This time scale ensures the quantum system is adiabatically transformed from a harmonically trapped gas to a Fermi-Hubbard system. In reality, such a ramp can never be fully adiabatic, since energy gaps might open and close within the many-body spectrum. Simultaneously to the lattice ramp, the magnetic offset field is linearly increased from 600 G to a final value of 650-700 G to realize strong repulsive interactions. This corresponds to a typical final scattering length of $a_{\mathrm{sc}} = 810$-$1660\,a_0$, where a_0 denotes the Bohr radius. Representative values for achieved Fermi-Hubbard parameters are $t/h \sim 200\,$Hz, $U/t = 8$ and superexchange $J/h \sim 100\,$Hz.

After the desired Fermi-Hubbard system is realized, the wavefunction is projected onto the Fock basis of the lattice by non-adiabatically turning off the hopping. This is achieved, by quenching the lattice depth to $V \sim 40\,E_{\mathrm{R}}$ within less than a hopping time ($< 1\,$ms). To take single-particle resolved fluorescence images, atoms need to be pinned by even higher lattice depths. Raman-sideband cooling requires the realization of the Lamb-Dicke regime.

Pinning lattice

A unique feature of this experiment is the decoupling of simulation and detection. There is an optical lattice for the physics and a dedicated lattice for pinning during

Physics lattice: ● ● ● $1.15\,\mu\mathrm{m}$
Pinning lattice: · · · · · · $0.532\,\mu\mathrm{m}$
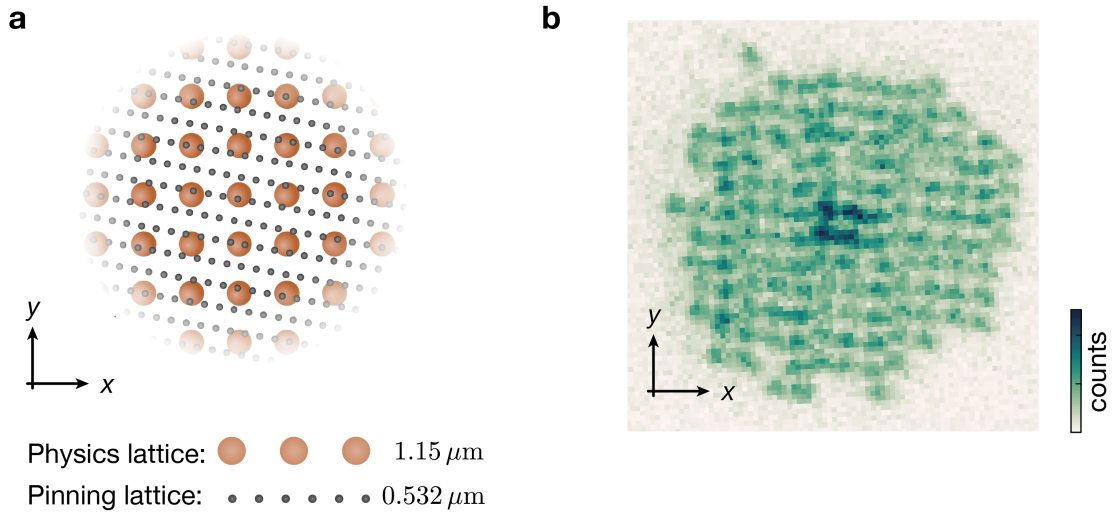
Figure 2.3: Single-site resolved fluorescence imaging. a, To perform fluorescence imaging, atoms are transferred from the physics lattice to the pinning lattice. The pinning lattice has a much smaller spacing, which leads to an oversampling effect and preserves the atomic position. In addition, parity projection can be avoided by turning on strong repulsive interactions during the loading from physics to pinning lattice. This forces double occupations on a physics lattice site to distribute into different pinning lattice sites. Illustration taken from [157]. **b,** Sample fluorescence image of a Mott insulator, obtained by Raman-sideband cooling. The pinning lattice spacing is optically not resolved. In the center of the system, a few doublons (sites with twice the signal) are visible, which demonstrates the absence of parity projection.

detection. In this way, the pinning lattice parameters are tailored to the detection process.

The pinning lattice (PL) consists of three retro-reflected lattices at $\lambda = 1064\,\mathrm{nm}$, whose orientation is rotated compared to the physics lattice [49]. After the recently implemented upgrade in 2019, each lattice reaches a power per beam of $\sim 30\,\mathrm{W}$ on the atoms at a focused gaussian waist of $w = 50\,\mu\mathrm{m}$. The generated lattice sites have an on-site trap frequency up to 1.8-2 MHz. To obtain single-site resolved snapshots, Raman-sideband cooling is applied to atoms in the PL to collect fluorescence photons with the high-NA objective [49]. A sample image of a Mott insulator is shown in Fig. 2.3b. The PL has a spacing of $0.532\,\mu\mathrm{m}$, which is significantly smaller than the

physics lattice. Thus, the PL sites oversample the physics lattice sites, see Fig. 2.3. By adiabatically loading the PL from the physics lattice in the presence of repulsive interactions, parity projection can be avoided [49]. A double occupation consisting of two spins on a physics lattice site is separated into two different PL sites. As shown in Fig. 2.3, PL sites are optically unresolved, such that the two separated spins appear as twice the fluorescence signal.

Since detection is performed in the PL, the physics lattice can potentially be optimized for large and homogeneous systems. So far, the current physics lattice does not particularly maximize homogeneity in this respect. The next subsection explores the potential impact and limits of a physics-lattice optimization.

2.1.3   Limits of square optical lattices

The decoupling of simulation and detection has many advantages. It gives the physics lattice much more freedom in terms of lattice structure, beam-shaping, and laser source. In the following, the optimal design and general scalings of a square physics lattice in terms of system size and homogeneity are explored. The maximum system size is found to be independent of the choice of lattice spacing. With current commercial laser sources, 2d Mott insulators with up to $\sim 10^6$ atoms could be realized for heavier elements and with up to $\sim 10^5$ atoms for lithium.

The following derivations for homogeneity and system-size scalings will make two assumptions:

- Fermi-Hubbard systems are realized at a physics-lattice depth of $9\,E_{\mathrm{R}}$.

- At maximum laser power, the physics lattice is always $40\,E_{\mathrm{R}}$ deep (to allow for a regime with frozen dynamics).

The homogeneity (or physical system size) of 2d Fermi-Hubbard systems in plain square optical lattices is fundamentally limited by the radial harmonic confinement ω, which is caused by the gaussian-beam profile of the laser beams. The full Hamiltonian contains the Fermi-Hubbard-part and the harmonic contribution as a function of the radius R

$$\mathcal{H}_{\mathrm{ho}} = \frac{1}{2} m \omega^2 R^2. \tag{2.1}$$

For the Mott-insulating regime, restrictions on system size caused by this trapping potential are easy to understand. When the harmonic term at some radial distance R becomes larger than the on-site repulsion U, it is energetically more favorable for a particle to form a double occupation in the center. Therefore, Mott insulators can

only extend over some maximum number of lattice sites $N^\star$ because additional atoms would fall into the center. In a doped system, the harmonic confinement competes with the energy scale t and indirectly with J or smaller many-body energy gaps at much lower temperatures. It is therefore highly desirable, to create optical lattices with minimal harmonic confinement.

A useful quantity to estimate the homogeneity of a system is the ratio ρ between the energy offset one lattice site away from the center $R = a$ and the single-particle bandwidth $W = 8t$. The smaller ρ, the flatter the optical potential. At $U = 8t$, the maximum system size $N^\star$ and ρ are related by

$$N^\star = \pi/\rho = \frac{\pi 16 t}{m\omega^2 a^2}. \tag{2.2}$$

Based on two assumptions, this equation can be expressed for any atomic species in terms of maximum available laser power per beam P, the atomic mass m and the real part $\alpha(\lambda) = \mathrm{Re}(\tilde{\alpha})$ of the complex polarizability $\tilde{\alpha}$. The first assumption concerns the lattice depth, at which Fermi-Hubbard systems are realized. Fermi-Hubbard systems need a sufficiently high lattice depth, which realizes the tight-binding limit. Since the tight-binding limit is universal in units of the recoil energy, we choose to consider Fermi-Hubbard systems at a fixed depth of $V = 9\,E_R$. Note that the recoil energy $E_R = h^2/8ma^2$ depends on the mass and chosen lattice spacing. The second assumption states that the symmetric waist of lattice beams will always be adjusted, such that at maximum power P a depth of $40\,E_R$ will be realized. Under these two conditions, Eq. 2.2 can be transformed into (for a detailed derivation see appendix A.1)

$$N^\star_{9,40} = b \cdot \alpha \cdot m \cdot P \ , \tag{2.3}$$

where $b = (128(9)^{3/4}e^{-6})/(45\sqrt{\pi}h^2\epsilon_0 c)$ is a constant, ϵ_0 the vacuum permitivity and c the speed of light. There are some important insights to Eq. 2.3, which are worth spelling out.

Scaling with P

In 2d Fermi-Hubbard systems, the size $N^\star$ scales linearly with laser power per beam P and linearly with polarizability α. When engineering optical lattices, there is very little freedom in the choice of laser wavelength and therefore in the control of α. The best quality and highest power lasers are mostly available at 1064 nm. Azurlight Systems currently offers a 130 W fiber amplifier at this wavelength. As shown in Fig. 2.4a, at this wavelength and power, Mott insulators with up to one million atoms could be realized with heavy elements and on the order of 10^5 atoms with lithium. With this
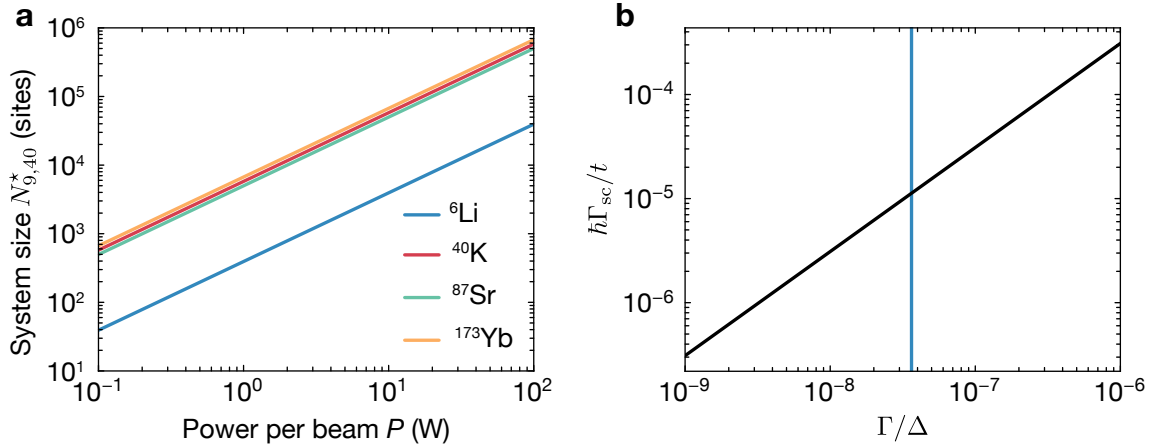
Figure 2.4: System-size scalings for 2d lattice simulators. a. The maximum Mott-insulator size ($U/t = 8$) in square optical lattices as a function of available power per beam for different fermionic species at a laser wavelength of 1064 nm and lattice depth of $9\,E_R$. This calculation assumes a separate lattice for detection, see text. **b**, Off-resonant scattering rate from an optical lattice compared to the tunneling time scale as a function of detuning from an atomic transition (two-level approximation). The blue vertical line corresponds to the detuning of $\lambda = 1064$ nm from the main D1 and D2 transitions of ^{6}Li. The electronic ground-state polarizabilities at 1064 nm (linear polarization) for fermionic (lithium, potassium, strontium, ytterbium) used in these calculations are (270.8, 597.5, 237, 160) atomic units [167–171].

respect, current quantum gas microscope setups underperform by almost three orders of magnitude because their simulation and detection lattices are identical. Under optimal conditions and dedicated engineering, extremely homogeneous systems could be realized with a machine, where a separate physics and pinning lattice are used.

Scaling with α

If there was a way to choose the laser wavelength freely, Eq. 2.3 suggests using laser light as resonant as possible with an electronic transition. In a two-level system, the polarizability increases with smaller detuning Δ according to

$$\alpha = 2\epsilon_0 c \frac{3\pi c^2 \Gamma}{2\omega_0^3 \Delta} \quad . \tag{2.4}$$

A larger polarizability leads to higher efficiency in the conversion from laser power to depth of the optical potential, which means larger beam waists can be used. The price to pay is a higher off-resonant scattering rate $\Gamma_{sc} \propto I/\Delta^2$ of the atom from the lattice light, c.f. Eq. 1.4. A useful quantity for this unwanted heating effect is the ratio

between Γ_{sc} and the tunneling amplitude t at $9\,E_R$. The smaller this ratio, the lower the effective heating. As shown in Fig. 2.4b, in a $9\,E_R$ lattice the scattering rate scales linearly with α and does not depend on the lattice spacing a, see appendix A.1. Since a higher α means less intensity I is needed for $9\,E_R$, the scattering rate scales like $\propto 1/\Delta \propto \alpha$ at constant lattice depth. The heating rate for lithium atoms in a 1064 nm lattice at $9\,E_R$ is five orders of magnitude smaller than the tunneling timescale. This heating poses a fundamental limit on the lowest achievable temperature. This limit can be traded for a higher or smaller achievable system size. In practice, high optical powers are available at limited wavelengths, which only allows for a very discretized choice of α.

Scaling with a

The system size is independent of the choice of lattice spacing. When a larger lattice spacing is chosen, the tunneling amplitude is smaller, but the waist of the beams can be larger to reduce the harmonic confinement. Both effects cancel each other. The lattice spacing therefore only sets the absolute energy scale of the Fermi-Hubbard system, but not its size. In Fig. 2.5, the absolute tunneling amplitude and the corresponding waist are shown as a function of the lattice spacing. The same relative homogeneity ρ can be achieved with small or large lattice spacings. There are, of course, other considerations, which dictate the final choice of lattice spacing. Large spacings simplify the optical resolution, but a pinning lattice might be limited to single-site imaging within a fixed volume. A high absolute energy scale is furthermore desirable to avoid heating from technical noise.

Scaling with m

Heavier atomic species lead to larger system sizes than lighter species (assuming the same polarizability). This scaling originates from the smaller recoil energy for heavier particles. Heavier elements yield a larger $N^\star$, but the price is a lower absolute hopping amplitude.

This paragraph highlighted how the decoupling of detection and simulation is a powerful feature, which enables very homogeneous systems in quantum gas microscope setups. This technique still bears great potential and a new generation of physics lattices is underway to significantly improve the homogeneity of Fermi-Hubbard systems on the MPQ machine. Imaging very large systems with single-particle resolution is a separate topic, for which tailored detection cavities might play an important role. But already a system homogeneity equivalent to $\pi/\rho = N^\star = 10^5$ would dramatically improve the quality of the simulated system, even if in the end only a smaller subsystem of e.g. 10^3 atoms is imaged with single-site resolved detection.
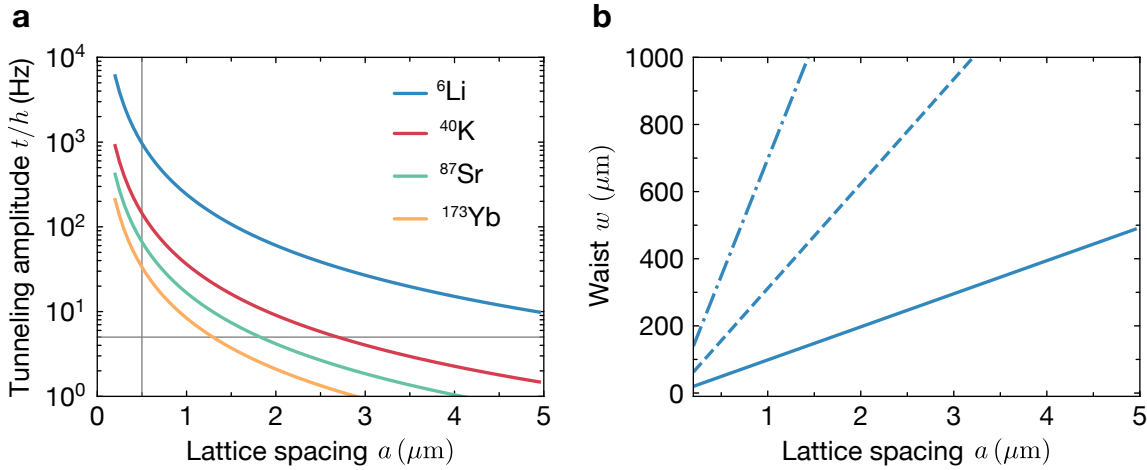
Figure 2.5: Scaling of tunneling amplitude in square optical lattices. a. Tunneling amplitude in a square lattice of $9\,E_R$ depth as a function of lattice spacing for different fermionic species. The gray vertical line denotes the typical limit of optical single-site resolution ($\sim 0.5\mu$m). The gray horizontal line marks an arbitrarily chosen 5 Hz tunneling amplitude threshold. **b**, Gaussian-beam waist of 1064 nm lattice beams, which optimizes the system size and satisfies a freezing condition (see text), as a function of lattice spacing. Solid, dashed and dash-dotted lines correspond to available laser powers of 1, 10 and 50 W.

2.2   Engineering optical superlattices

Two lattices along the same spatial direction with different, but commensurate, spacings form a superlattice potential, see Fig. 2.6. This section highlights, how relative-phase stability is of utmost importance for such lattices. A bichromatic in-vacuum design of a vertical superlattice is presented, which achieves high relative-phase stability while maintaining full tunability.

   Superlattices are interesting for multiple reasons. In this experiment, spacings of the shorter and longer lattice are related by $a_l = 2 \cdot a_s$. Such superlattices were proposed as a route towards accessing colder temperatures of Fermi-Hubbard systems through entropy engineering [172, 173]. Furthermore, the 1d superlattice with spinless particles realizes the paradigmatic Su-Schrieffer-Hegger (SSH) model with nontrivial topological properties, which was initially introduced to explain the behavior of polyacetylene [174]. Spinful versions of this model in the presence of interactions and its extension to two dimensions represent exciting research avenues in the future.
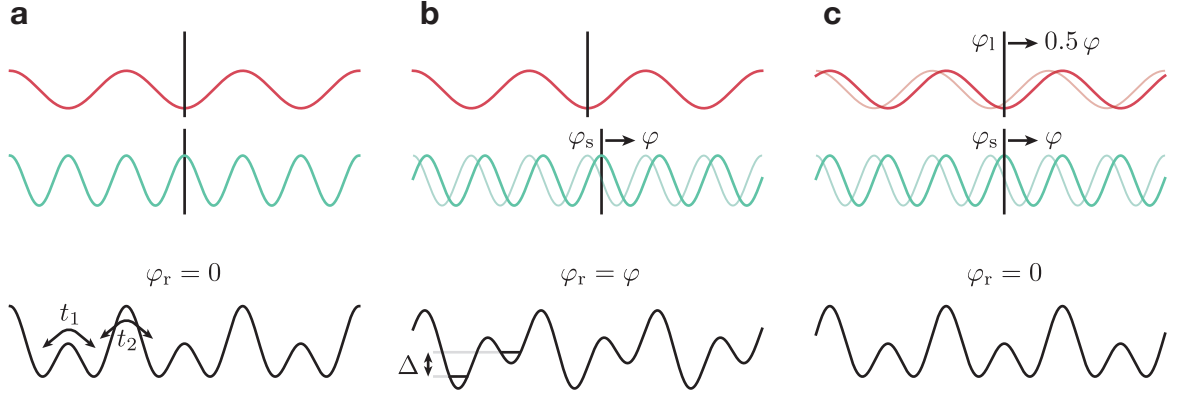
Figure 2.6: Superlattice potential. a, A superlattice is the combination of two different lattices with commensurable lattice spacings. Here, the long lattice (red) has twice the spacing of the short one (green). The relative phase φ_r between the lattices determines the pattern of the combined potential, which in the depicted case forms an array of double wells with intra- and inter-double-well hopping amplitudes t_1 and t_2. **b**, A phase shift of one of the two lattices leads to a shift in φ_r. The initially symmetric double well is tilted by a detuning Δ. **c**, If both lattices experience a phase shift with a fixed relation $\varphi_s/\varphi_l = 2$, φ_r and therefore the superlattice pattern is preserved.

2.2.1 Relative phase stability

The superlattice potential is given by

$$V_{SL} = V_l \cos^2(\pi x/a_l + \varphi_l) + V_s \cos^2(\pi x/a_s + \varphi_s) \tag{2.5}$$

and has four parameters in total. The long and short lattice depths V_l, V_s and phases φ_l, φ_s. For this choice of definitions, the lattice phases φ_s, φ_l are related to the phase difference of the interfering electromagnetic fields by $\varphi_s = \varphi_s^E/2$. The shape, i.e. the topography of the potential, is controlled by the relative phase between the two lattices

$$\varphi_r = \varphi_s - 2\varphi_l. \tag{2.6}$$

Using $x_0 = \varphi_l a_l/\pi$, the potential can be expressed as

$$V_{SL} = V_l \cos^2(\pi(x - x_0)/a_l) + V_s \cos^2(\pi(x - x_0)/a_s + \varphi_r) \tag{2.7}$$

The relative phase φ_r directly relates to the energy offset Δ between neighboring sites, see Fig. 2.6. For $\varphi_r = 0$ the potential resembles an array of double-well potentials. As long as the phase relation of Eq. 2.6 stays constant, the superlattice shape is
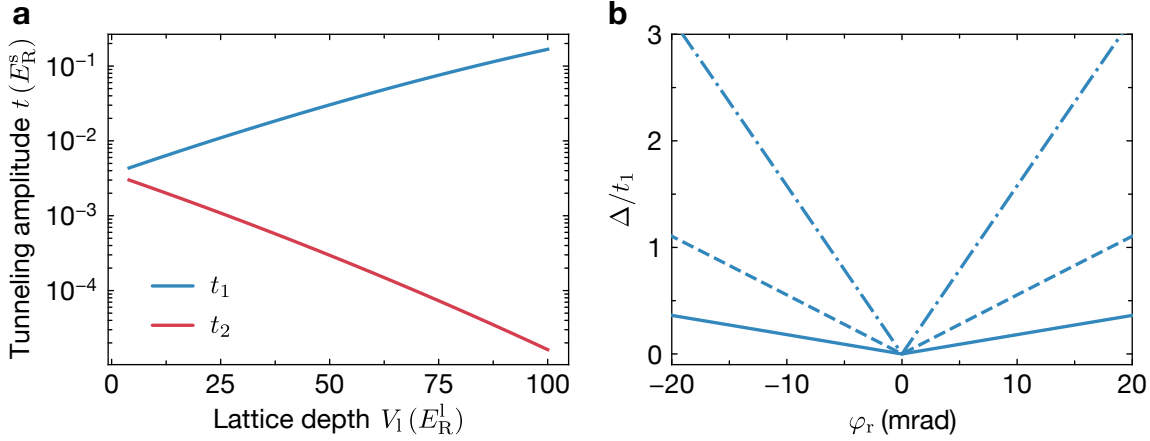
Figure 2.7: Double-well tunnelings and tilt. **a**, Wannier-function calculation of intra- and inter-well tunneling amplitudes t_1 and t_2 for fixed depth of the short lattice at $V_s = 18\,E_R^s$ as a function of the long lattice depth V_l in a symmetric double-well configuration. A deeper long lattice enhances intra-well tunneling and suppresses inter-well tunneling. **b**, Double-well tilt Δ in units of intra-well tunneling as a function of relative superlattice phase at fixed long-lattice depth of $100\,E_R^l$. Symmetric double wells are realized at $\varphi_r = 0$. Solid, dashed, dash-dotted lines correspond to short lattice depths of 11, 15, 19 E_R^s.

preserved. If $\varphi_r = $ const, the remaining total change in lattice phases merely leads to a spatial translation of the fixed superlattice pattern, quantified by x_0.

The intra- and inter-well tunneling amplitudes t_1, t_2 (see Fig. 2.6) are related to the absolute depths of both lattices, their ratio and the relative phase. At zero large lattice depth $V_l = 0$, the two tunneling amplitudes t_1, t_2 are equal. Upon increasing the power of the large scale lattice in a symmetric double well $\varphi_r = 0$, t_1 strongly increases, while t_2 decreases, see Fig. 2.7a. This effect enables an enhancement of t_1 by almost an order of magnitude and can be used to generate strongly-coupled wells or bi-layer systems as discussed in the next sections. Note that this enhancement is partly due to the long lattice pushing the two wells of the double well closer together. In the limit $V_l/V_s \to \infty$, only a single well exists and the double-well picture breaks down. For a superlattice in double-well configuration at fixed lattice depths, the double-well detuning Δ/t_1 scales linearly with a change in the relative phase, see Fig. 2.7b. The slope depends on the lattice depths and decreases for shallower short lattice depths V_s.

Noise or spatial gradients of φ_r lead to a temporally or spatially varying phase $\delta\varphi_r$ and, thus, to varying energy offsets Δ between potential wells. There can be sources of short-term noise on the time scale of the system dynamics and drifts of the experi-
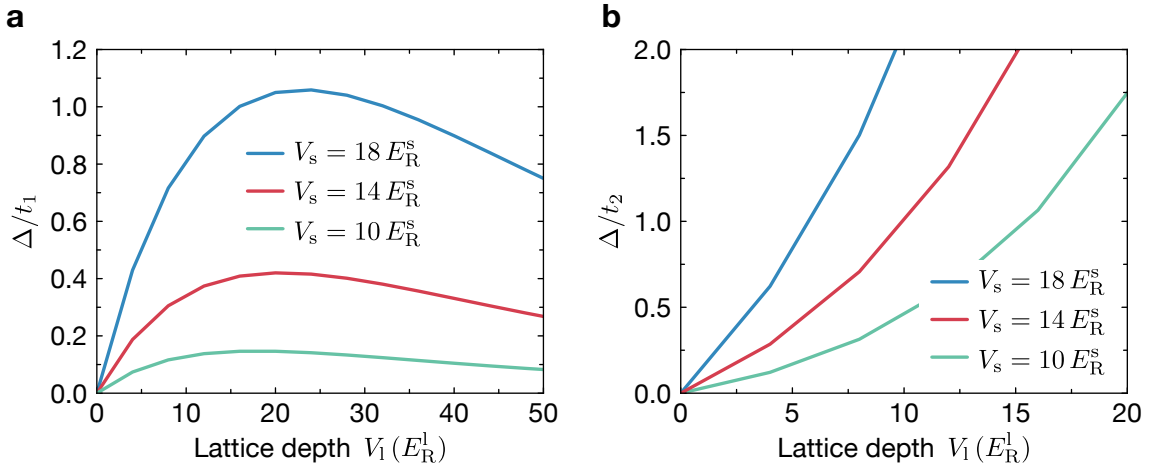
Figure 2.8: Sensitivity to relative phase noise. a. Wannier-function calculation of the double-well detuning caused by a 1 mrad shift in relative phase away from the symmetric case ($\varphi_r = 0$) in units of the intra-well tunneling as a function of the long-lattice depth. For low depths, the double-well sensitivity initially increases. For high depths, the intra-well tunneling enhancement dominates and stabilizes the double well against relative phase fluctuations. **b**, Double-well detuning compared to the inter-well tunneling as a function of long-lattice depth. The sensitivity of the inter-well system continuously increases with higher lattice depths.

ment causing long-term noise. When phase-noise induced changes of tilts are on the order of the hopping amplitude, the superlattice cannot be operated successfully. Depending on the application, the tilt from phase noise should, therefore, be compared to t_1 and/or t_2.

The absolute amplitude of phase noise usually does not depend on the used lattice depths, but originates from fluctuations of the environment. The conversion of phase noise to fluctuating detunings Δ/t_1 can be very different, depending on the exact choice of lattice parameters. Therefore, it is worthwhile to investigate for which settings a superlattice is the most susceptible to phase noise.

The double-well tilt induced by a 1 mrad phase change around $\varphi_r = 0$ is shown in Fig. 2.8. Different ratios and absolute depths of short and long lattice have a different sensitivity. When starting with a short lattice and turning on the long lattice, the intra-well and inter-well sensitivity to phase noise increases quickly. For the intra-well system though, the enhancement of t_1 scales much faster at some point than the sensitivity of Δ with φ_r. As an effect, the sensitivity of the intra-well system decreases for very high depths of the long lattice. A general property of the double-well system is that a deeper short lattice always leads to a higher sensitivity for the intra- and

inter-well system. The inter-well system sensitivity increases with increasing power of either lattice. In several manipulation schemes (such as the ones used in this work), the inter-well sensitivity is not relevant.

Requirements for phase stability $\delta\varphi_r$ vary between applications. Separating two spins with a magnetic gradient to the left and right side of a double well requires no coherent tunneling. As long as the strength of the magnetic gradient creates a tilt much stronger than the tilt from phase fluctuations, spin splitting can be performed. The spin-splitting sequence presented in this works is robust up to phase variations of $\delta\varphi_r \sim 300$ mrad. For bilayer physics and charge pumping demonstrated in the following sections, only the intra-well system is relevant. In that case, a phase stability of $\delta\varphi_r \lesssim 25$ mrad is sufficient to guarantee $\Delta/t_1 < 1$, see Fig. 2.7b. For a connection from band insulator to Mott insulator [172] or for staggered systems the sequence involves coherent inter-well tunneling. Therefore, to ensure $\Delta/t_2 < 1$ much better phase stability on the order of a few mrad is required, see Fig. 2.8b. In this work, a setup with $\delta\varphi_r \leq 25$ mrad is demonstrated. This is an upper bound and might not be the actual limit of the implementation. Spatial inhomogeneities limited the measurement resolution.

2.2.2   Bichromatic superlattices

Bichromatic superlattices grant passive protection of the relative phase from a fluctuating environment. This is a direct consequence of the condition $\varphi_s = 2\varphi_l$. The condition implies that if short and long lattice fluctuate at this ratio, the phase φ_r will be preserved. In a bichromatic superlattice, the wavelengths for generating short and long lattice differ by $2\lambda_s = \lambda_l$. Changes in the environment alter the refractive index by δn. The phase of a lattice is thus affected by $\delta\varphi \sim \delta n/\lambda$. The factor of two between the wavelengths of the lattices therefore automatically ensures the phase stability condition.

We consider the common choice $\lambda_s = 532$ nm and $\lambda_l = 1064$ nm. Both lattices require the same interference angle α, since the factor of two in wavelength automatically leads to a two times smaller spacing for the shorter wavelength. To optimize stability, laser beams for both lattices can share the same optical path and elements. It is therefore only necessary to generate a single bichromatic beam, which is then split into two bichromatic beams. These two beams, representing two arms of an interferometer, are then directed and interfered at the position of the atoms. The only relevant optical phase contributing to the absolute and relative phase depends on the path and environment between the point of splitting and the position of the atoms.
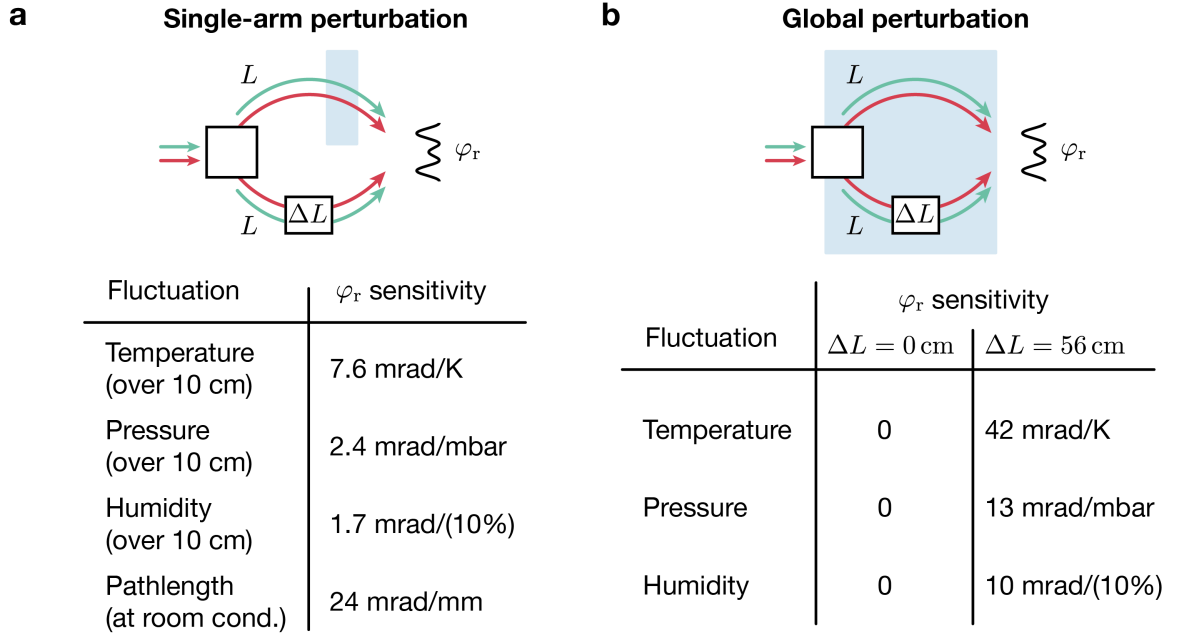
a   **Single-arm perturbation**   **b**   **Global perturbation**

Fluctuation	φ_r sensitivity
Temperature (over 10 cm)	7.6 mrad/K
Pressure (over 10 cm)	2.4 mrad/mbar
Humidity (over 10 cm)	1.7 mrad/(10%)
Pathlength (at room cond.)	24 mrad/mm

Fluctuation	φ_r sensitivity	
	$\Delta L = 0\,\mathrm{cm}$	$\Delta L = 56\,\mathrm{cm}$
Temperature	0	42 mrad/K
Pressure	0	13 mrad/mbar
Humidity	0	10 mrad/(10%)

Figure 2.9: Relative-phase noise considerations (in air) for bichromatic setups. A single bichromatic beam is split into two bichromatic beams, which are interfered at the atom position to create a superlattice potential. The two bichromatic beams form an interferometer with two arms of length L and $L + \Delta L$. Here we assume the interferometer to be filled with air at room conditions (23 K, 1 bar, 50 % humidity). **a**, Sensitivity of φ_r to local fluctuations in a single arm. **b**, Sensitivity of φ_r to a change of the global environment affecting both arms. Refractive index changes were calculated based on [175] and can be found in A.2.

Stability in air

The dispersive properties of a medium break the perfect stability of bichromatic superlattices and introduce a residual sensitivity to the environment. Fluctuations like turbulences, pressure waves, or thermal gradients in optical setups can therefore lead to variations of the relative phase. However, compared to monochromatic superlattices, the induced phase noise in air is strongly suppressed in bichromatic setups.

To analyze the impact of environmental fluctuations, let the length of the two interferometer arms be $(L, L + \Delta L)$. The refractive indices for the short or long wavelength in the ith arm are denoted by n_i^s, n_i^l. If the difference in refractive index between both arms for short or long lattice is $\delta n_{12}^{s,l} = n_1^{s,l} - n_2^{s,l}$ respectively, then

$$\varphi_r/\pi = (\delta n_{12}^s - \delta n_{12}^l)L/\lambda_s + (n_2^s - n_2^l)\Delta L/\lambda_s. \qquad (2.8)$$

This expression can be used to demonstrate stability features of bichromatic super-lattices. In the following, the medium is taken to be air to exemplify the behavior in different situations, as summarized in Fig. 2.9.

For a balanced interferometer ($\Delta L = 0$), absolute (global) changes in the environment affecting both arms equally ($\delta n_{12} = 0$) do not affect the relative phase, no matter the medium. However, local changes in a single arm of the interferometer do have an effect, see Fig. 2.9a. One example is small displacements δL through moving elements, such as mirrors. At room conditions in air, φ_r changes by 24 mrad for a change in optical path length in one arm of one millimeter. For small displacements $\delta L \ll 1$ mm the impact on the relative phase is therefore small. If the temperature, pressure, or humidity of air change in a small region of length 10 cm in one of the arms, the relative phase is weakly affected. For a one Kelvin increase in temperature, φ_r changes by 7.6 mrad in bichromatic setups, whereas in a monochromatic setup the change is 271 mrad.

For an imbalanced interferometer ($\Delta L \neq 0$), the same stability conditions for local fluctuations apply as in the balanced case. Furthermore, global changes also impact the relative phase, as summarized in Fig. 2.9b. The path imbalance ΔL makes the relative phase susceptible to global drifts in temperature, pressure or humidity, albeit with small sensitivity. As an example, an imbalance of $\Delta L = 56$ cm is considered. This corresponds to the setting realized for the vertical in-vacuum superlattice, as described in the upcoming section. A global temperature increase of one Kelvin leads to $\delta \varphi_r$ of 42 mrad. This means, even in the presence of extreme global fluctuations of the environment, a bichromatic in-air superlattice should enable a robust spin-splitting sequence in this experimental setup ($\delta \varphi_r < 300$ mrad).

The considered in-air scenarios demonstrate that under laboratory conditions in a well-controlled environment, bichromatic superlattices are ideally suited to ensure high stability of φ_r. In vacuum, the perfomance of bichromatic implementations increases even further.

Handling bichromatic beams

To design bichromatic optical setups several complications need to be overcome.

Beam shaping of bichromatic beams is fundamentally limited by the behavior of gaussian beams. To keep foci and divergence of both colors the same, the beam waists of the long and short lattice beam need to fulfill the requirement $w_l = \sqrt{2}w_s$. This is particularly important for optical paths $L/z_R \geq 1$, where z_R is the Rayleigh range of either color.

The dispersion of glasses used for lenses leads to chromatic shifts in beam shaping. At low optical intensities, multi-component lenses can be used to construct achro-

matic lenses, which mitigate this effect. Available achromatic lenses always contain glasses with strong thermal lensing properties, most severe for short wavelengths such as $\lambda = 532\,\mathrm{nm}$. In particular with green light and at the intensities required for optical lattices, only fused silica should be used as a material. Therefore, no appropriate achromatic lenses exist.

Precise polarization control of bichromatic beams at high optical intensities is not straightforward, due to the lack of zero-order waveplates. Besides, every transmission through a strongly dispersive element, such as fused silica used for lenses, windows, or polarizing beamsplitters, represents a source of mutual misalignment between the two colors. In particular, elements with wedged surfaces should be avoided, since they introduce a relative angle between the two colors which is difficult to reliably compensate afterward.

2.2.3 Delay line

On the one hand, superlattices should be built with an extremely stable phase φ_r. On the other hand, there needs to be a knob to tune φ_r in an experiment, ideally dynamically. Three approaches to enable controlled tuning of φ_r are considered, while only the delay-line concept was eventually implemented in the experimental setup.

The first solution is to place a rotatable dispersive glass plate with planar surfaces into one of the interferometer arms. Depending on the thickness of the plate, a rotation leads to a shift $\varphi_\mathrm{s} \neq 2\varphi_\mathrm{l}$ and as a trade-off introduces an additional spatial offset between the two colors in this arm. We do not pursue this technique in this work because the required physical movement limits the speed and precision of the phase control. In principle, this technique is well suited for a coarse and slow adjustment of φ_r and might be pursued in the new generation of xy-superlattices.

A second approach is to place an electro-optical modulator (EOM) in one of the interferometer arms. The basic idea is to apply an electric voltage V to the EOM crystal and to control the relative phase by changing the refractive index through the linear electro-optic effect [176, 177]. This technique is not as straightforward as it sounds. The applied voltage alters the refractive index of both colors by the same amount $\delta n_\mathrm{s} = \delta n_\mathrm{l} \propto V$. But from Eq. 2.8, this will not affect φ_r. This can be remedied, by using orthogonal polarizations for the two colors. The EOM can be engineered to change the refractive index only along one polarization axis, which would then allow control of φ_r. But as pointed out in the previous section, polarization control for bichromatic beams is complicated. Furthermore, typical EOM crystals do not withstand high optical intensities and can suffer from severe thermal lensing or optical corrugations. In an initial design for the bichromatic superlattice presented in this work, such an EOM-based control was tested. As documented in [178], the required

high voltages $V \sim 0.1\text{-}1\,\text{kV}$ were found to cause problematic instabilities in the used potassium dideuterium phosphate crystal (custom EOM from Qubig), if applied for durations longer than $\sim 100\,\text{ms}$.

The last approach, which is eventually implemented in this work, is based on a heavily imbalanced interferometric setup. One arm propagates for an extra optical path ΔL, referred to as the delay-line length. When the optical frequency ν of, for example the green lattice, is changed by $\Delta\nu$, the underlying lattice acquires a different phase φ_s and the spacing a_s changes. As long as $\Delta\nu/\nu \ll 10^{-5}$, the lattice spacing mismatch with a_l induces a spatial gradient of the relative phase less than 1 mrad per 100 sites and can be neglected. The shift in relative phase caused by this frequency shift, on the other hand, is sizable

$$\Delta\varphi_r = \pi \cdot \Delta\nu \cdot \Delta L/c. \tag{2.9}$$

A major advantage of this technique is the absence of physically movable elements in the optical beam path and the high accuracy and speeds achievable in optical frequency control. As a trade-off, ΔL introduces sensitivity to drifts and noise in the global environment of the interferometric setup as described before and seen in Eq. 2.8. Furthermore, a high dynamical tuning range of $\Delta\nu$ to keep ΔL small is challenging to achieve.

2.2.4 A vertical superlattice

A bichromatic superlattice with a delay-line technique for controlling φ_r was built into the experimental setup in 2019. To achieve maximal phase stability, a dedicated in-vacuum design was developed. Almost the entire interferometric path and its optics are located in an evacuated aluminum chamber. Two Master students, M. Höse and D. Bourgund, significantly contributed to engineering this lattice. Initial developments of the laser system and exploration of techniques are documented in [178]. Details on the final implementation and the design of the vacuum setup are described in [179]. The most important features are outlined below.

Laser source and frequency shifting

The laser system requires $\sim 8\,\text{W}$ of a Mephisto MOPA system (Coherent) at 1064 nm. As shown in Fig. 2.10, around 7 W are used for the long lattice. For the short lattice $\sim 1\,\text{W}$ are split off and sent through a frequency shifting module. This fully fiber-coupled module uses two acousto-optical deflectors (Gooch&Housego, AOD 4225-2) with extremely large single-pass bandwidth of 130 MHz and center frequency 225 MHz in a double-pass configuration. The output frequency of this module, therefore, obtains a constant offset and can be tuned by $> 400\,\text{MHz}$, which in combination
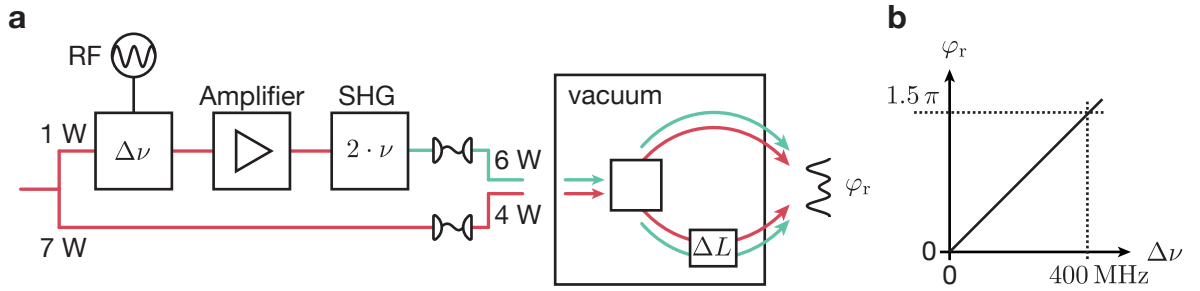
Figure 2.10: Laser setup and phase control. a, Around 8 W of 1064 nm light are used as an input for the bichromatic superlattice setup. 7 W are used for the long-scale lattice. 1 W is sent to a frequency-shifting module, which enables tunability of the frequency by up to 400 MHz. A fiber amplifier re-amplifies the power to 40 W. In a SHG module, around 12 W of 532 nm light are generated. A bichromatic beam is obtained by overlapping both colors on a dichroic mirror. The bichromatic beam is coupled into an evacuated setup, where two bichromatic arms for the superlattice are generated and launched onto the atoms. The path-length difference is $\Delta L = 56$ cm. **b**, The 400 MHz shift afforded by the shifting module enables tuning of φ_r in a range of $1.5\,\pi$.

with a $\Delta L = 56$ cm delay line setup enables a tuning range of $\sim 1.5\,\pi$ of the superlattice phase φ_r. The remaining power of the light after the AOD setup is around 40 mW at the fiber output and varies, depending on the frequency settings of the AODs.

The output of the frequency-shifting module seeds a fiber amplifier (Azurlight Systems), which re-increases the power to 40 W. Fiber amplifiers have to remain seeded at all times (during operation), which means the AODs inside must never stop diffracting. This demands a frequency drive with always-on output at an appropriate frequency, i.e. no micro shutdowns are allowed during frequency changes. Frequency stability and linewidth of the RF drive have a direct impact on the relative phase stability. Since the RF drives two AODs in double-pass configuration simultaneously, the phase sensitivity with respect to the RF frequency is $2 \cdot 2 \cdot 12$ mrad/MHz. This slope of $48\,\mu$rad/kHz means a stability and linewidth < 20 kHz of the RF drive is required for an impact on $\delta\varphi_r$ by less than 1 mrad. The current implementation uses a frequency generator from Stanford Research Systems (SG384) in external voltage bias mode in the GHz range, which is mixed down to the 200 MHz scale with a fixed frequency source from an Agilent E4432B.

More than 12 W of 532 nm light is generated from the 40 W at 1064 nm in a single-pass second-harmonic generation (SHG) through a periodically-poled Mg-doped stoichiometric LiTaO$_3$ crystal (length=30mm, 1° angle, Oxide). Peak powers

of $> 14\,\text{W}$ are possible with optimized beam waist and alignment, but long-term operation showed 10-12 W is more reliably achieved. Neglecting the frequency-shifting module, SHG ensures perfect commensurability $\lambda_l = 2 \cdot \lambda_s$ of the superlattice. The SHG module also doubles the frequency shift of the AOD setup.

The red (1064 nm) and green (532 nm) light are separately fiber-coupled and intensity stabilized. For the green light, a photonic crystal fiber (NKT, LMA-PM-15) with 5m length is used, while the red light currently uses a fiber (Schäfter-Kirchhoff, PMC-E-980) with an extra-large core. On the main experimental table, both colors are overlapped to form a single bichromatic beam with a dichroic mirror.

Evacuated lattice setup

An aluminum chamber with a removable lid encloses the optical setup and most of the optical path relevant for the bichromatic superlattice, see Fig. 2.11. The entire chamber is continuously pumped by a membrane pump (Pfeiffer, MVP 020-3 AC) to maintain a constant weak vacuum ($< 1\,\text{mbar}$). The pump is connected to the chamber via several meters of plastic tubes. No measurable effect of possible vibrations, originating from the continuous pumping, on the phase stability was found. Without pumping, the vacuum lifetime is on the order of a few days.

The single collimated bichromatic beam is coupled into the chamber through an anti-reflective (AR) coated fused silica window. The beam is subsequently divided into two bichromatic beams, using a non-polarizing $50 : 50$ beamsplitter (NPBS). The splitter consists of a fused silica substrate and a tailored narrow-band dielectric coating. Dual-band mirrors guide the bichromatic beams through the chamber with a $\Delta = 56\,\text{cm}$ delay line length for one arm. This length yields a dynamic tuning range of φ_r by $\sim 1.5\,\pi$. A spatial offset between both colors within a bichromatic beam is inevitably introduced by the transmission through dispersive material under an angle. The strongest displacement of order $\sim 10\,\mu\text{m}$ is introduced by the experimental glass cell, the beam splitter, and the output windows. To compensate for this effect, AR-coated planar fused-silica substrates are placed in the beam paths under specific angles.

Each arm is focused onto the atoms with an achromatic lens of focal length $f = 400\,\text{mm}$ (Thorlabs, AC254-400-B-YAG, custom V-coated). Beam sizes on these lenses are kept large enough to keep thermal lensing to a minimum. The collimation of each color before their combination was optimized, such that both foci are as close as possible to the atomic position. The designed beam waists at the lattice position for green and red are $\sim 90\,\mu\text{m}$ and $\sim 130\,\mu\text{m}$, respectively. 50 mm after these achromatic lenses, a $f = 350\,\text{mm}$ cylindrical lens in each arm prevents the waist in the horizontal plane from focusing. This creates strongly elliptical bichromatic beams. The green and red beams have horizontal waists of $\sim 600\,\mu\text{m}$ and $\sim 900\,\mu\text{m}$, respectively, which
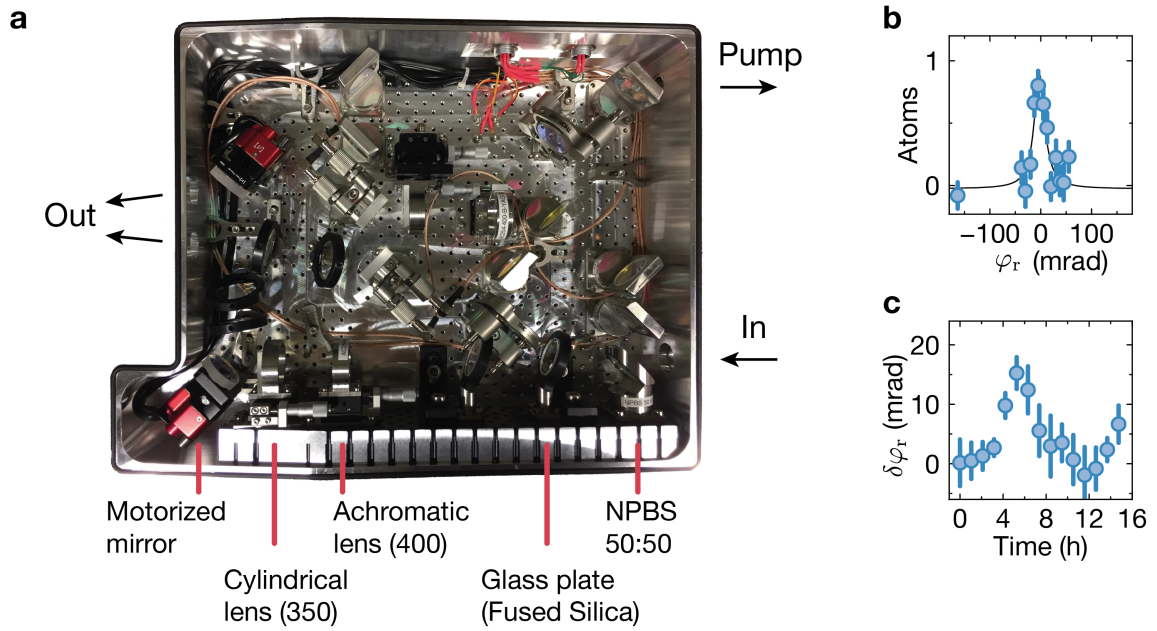
Figure 2.11: In-vacuum implementation of a bichromatic superlattice. a, A bichromatic beam (In) enters a closed aluminum box (lid was removed for the photo). The optics inside are under vacuum and realize beam splitting, shaping, and launching onto the atoms (Out). The beam-path difference between both arms within the box is 56 cm. **b**, A spectroscopic sequence measures the width of phases, for which a resonant transfer between two layers of the superlattice occurs in the weak-coupling limit. The lorentzian linewidth (solid black) of 25(7) mrad represents a worst-case value for the short-term stability, see text. **c**, The long-term phase stability of the transfer resonance was tracked in time. Drifts on the order of 10 mrad are visible.

leads to a vanishing contribution to the harmonic confinement in the xy-plane.

After both lenses, two externally tunable mirrors per arm launch the bichromatic beams onto the atoms. Mirrors with pico-motors (Newport, picomotor piezo optical mount 8885) have a large tuning range, but suffer from hysteresis. Classical piezo mirrors (Thorlabs, Polaris-K05P2) have a small tuning range, but can be used with zero hysteresis. In the current implementation, the short arm is equipped with two picos and the long arm with two piezos. The pico motor can be used for large steps while scanning with the piezo mirror ensures the possibility to always come back to the initial starting position.

A mutual opening angle between the bichromatic beams of $\alpha = 10°$ creates a short and long lattice spacing of $a_s = 3\,\mu m$ and $a_l = 6\mu m$. Around 15 cm before reaching the atoms, the beams exit the evacuated chamber and travel the same distance in free

space. The out-coupling windows are AR coated fused silica substrates, which are glued with vacuum-compatible glue (TorrSeal) onto holes in the aluminum frame of the chamber.

Characterization

We characterized the vertical bichromatic superlattice with the atomic system, see appendix A.3. Enhanced intra-well tunneling amplitudes of up to $t_1/h = 876(1)\,\text{Hz}$ were measured in a Rabi-flopping sequence. Upper bounds for relative-phase fluctuations in this setup were obtained with a spectroscopic sequence, as described in appendix A.3. The (short-, long-) term $\delta\varphi_r$ was found to be better than or equal to $(25, 10)\,\text{mrad}$, see Fig. 2.11b,c. Spatial potential inhomogeneities from other optical traps and residual mutual misalignment of the short and long lattice limited the measurement resolution for these upper bounds.

Stability of the absolute phase

In particular for vertical lattices, an additional requirement is long-term stability of the absolute lattice phase. A stable absolute vertical position is necessary for high-resolution microscopy of individual layers. In contrast to the relative superlattice phase φ_r, the absolute phase is not passively protected and therefore sensitive to environmental changes of the imbalanced ($\Delta L \neq 0$) interferometric setup.

Peltier elements and temperature sensors are mounted on the outside of the evacuated chamber to actively stabilize the absolute temperature of the lattice setup with a temperature controller. Furthermore, the absolute frequency of the Mephisto seed light at $1064\,\text{nm}$ drifts. The finite delay line causes a conversion of such frequency fluctuations into changes of the absolute lattice phase (note that φ_r remains unaffected). We use this effect to our advantage by biasing the temperature setpoint of the Mephisto laser, which changes the absolute frequency of the light. This temperature bias gives us a knob for slow feedback on the absolute lattice phase. We determine the vertical position of layers every ~ 3 minutes during operation with absorption images from the side. This information is then used to feedback onto the temperature of the Mephisto seed. These measures enable consistent data taking over several days in a thermalized setup.

2.3 Charge pumping for bilayer microscopy

Microscopy of multilayer systems is extremely difficult if atoms are tightly spaced compared to the imaging wavelength. When the fluorescence light of different dense layers cannot be suppressed, their combined signal renders a reconstruction of the

underlying occupations challenging. For this reason, quantum gas microscope experiments are normally performed on monolayers.

Several approaches have tried to resolve multilayer-imaging difficulties, but a high-fidelity and species-independent method for fermionic atoms is lacking. If scatterers are very dilute, the layer an atom is located in can be identified by the spatial extent of the collected light [180–182]. If the atomic species permits the suppression of fluorescence from individual layers during imaging, a potential solution was demonstrated for bosonic rubidium in [141].

Here, we demonstrate a technique for species-independent, high-fidelity, and robust microscopy of bilayer systems. The vertical bichromatic superlattice is employed to realize a charge pump, which increases the distance between two initially 3 μm separated layers to 21 μm. The large separation enables independent microscopy of each layer. At a distance of 21 μm, the out-of-focus layer contributes only a weak and homogeneous background, due to the shallow depth of field of our high-NA imaging system.

2.3.1 Charge pump

Charge pumping can be intuitively understood with a single particle in a double well, see Fig. 2.12a. The double well can be represented as a two-level system, whereby the left ($|L\rangle$) and right well ($|R\rangle$) represent the two possible states. A double-well tilt Δ creates an energy difference between both states. The intra-well tunneling $t_z = t_1$ corresponds to a Rabi coupling between the left and right state, which changes the eigenstates of the system. In the resonant case $\Delta = 0$, the eigenstates $|G\rangle$, $|E\rangle$ are equal superpositions of the atom in the left and right well. In the far detuned limit $|\Delta/t_1| \gg 1$, $|L\rangle$ and $|R\rangle$ become the eigenstates. In analogy to a Landau-Zener transfer in two-level systems, a passage from $\Delta/t_1 \ll -1$ to $\Delta/t_1 \gg 1$ transfers an atom initialized in one well to the opposite well. The condition for a successful transfer is adiabaticity with respect to t_1. Therefore an atom initialized in the left/right well experiences transport to the right/left upon the same modulation of parameters.

In an infinite array of double wells in a non-interacting many-body system, a process similar to the adiabatic transfer in the single double well can take place. In certain cases, this is referred to as topological charge pumping [183–185], which was initially introduced by Thouless [186]. The two states $|G\rangle$, $|E\rangle$ of the two-level picture now become the ground band G and excited band E, which have opposite Chern number [184, 187]. These bands cause transport in opposite directions upon the same adiabatic passage of the double-well tilt Δ. This is referred to as geometric pumping and lies at the heart of topological charge pumping in adiabatically time-modulated superlattices [183, 185, 188, 189]. As shown in Fig. 2.12b, an atom initialized in G can
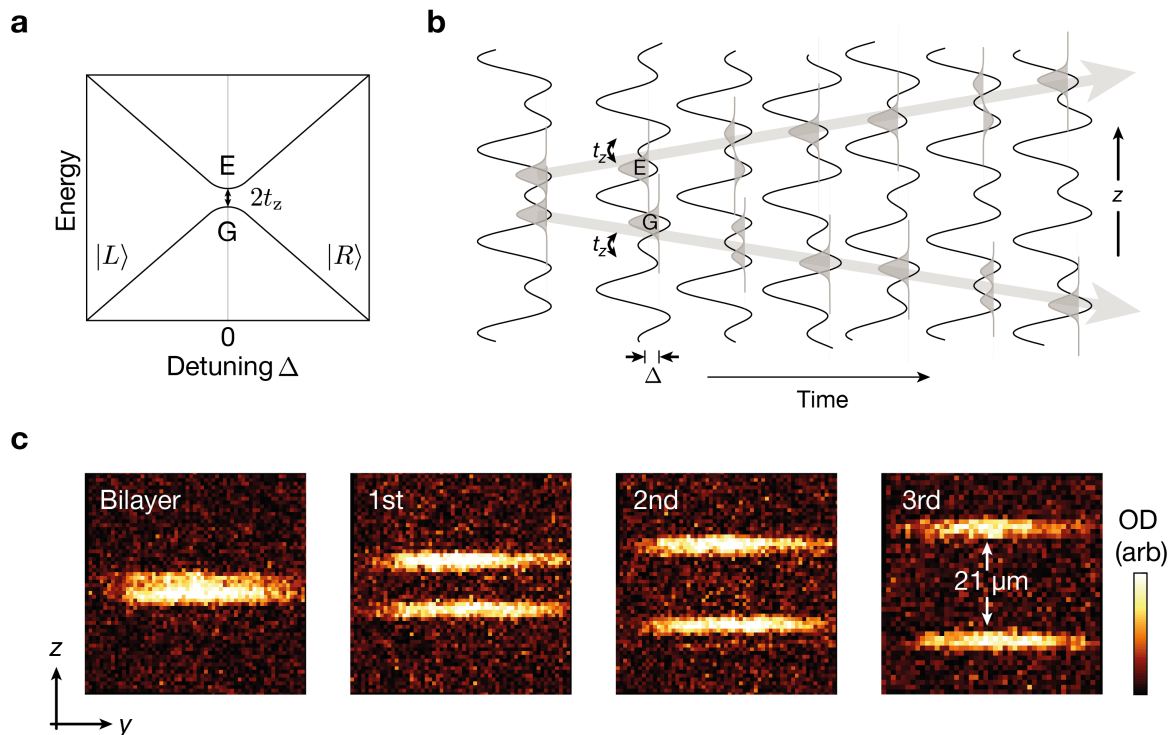
a

b

c

Figure 2.12: Bilayer charge pump. a, Energy level diagram in a single double well with tunnel coupling t_z as a function of the detuning Δ. Upon an adiabatic passage of the detuning, a particle initialized in the left/right well undergoes transport to the right/left well. **b**, In an infinite array of double wells, an adiabatic time-periodic modulation of the superlattice parameters can be used to transport atoms initialized in opposite wells into opposite directions. **c**, Absorption images from the side at different pumping steps for a bilayer system. The two initially unresolved adjacent layers separate by 6 µm for every pumping step.

be transferred to a neighboring well by adiabatically changing the energy offset Δ between the wells at a constant intra-well tunneling amplitude t_z. For the same ramp, an atom in E will be transported to a neighboring well in the opposite direction. Performing j such adiabatic pumping steps can be used to separate two initially adjacent layers (separated by a_s) by large distances $a_s + j a_l$. In Fig. 2.12c, charge pumping of a bilayer system with up to three steps is shown with absorption images from the side. The initially unresolved and adjacent layers increase their separation by one large lattice spacing a_l after each step and become well resolved.

A single pumping step is not the same as a closed loop in parameter space. Thou-

less charge pumping refers to an adiabatic and closed loop. The experimentally implemented sequence differs from this strict definition and pump parameters were optimized for high-fidelity transport.

The sequence to separate a bilayer system with initial spacing of $3\,\mu$m closely resembles Fig. 2.12b. The current procedure contains three pumping steps and is performed within less than $400\,$ms, during which the motion in the xy-plane is frozen out ($V_{x,y} = 43\,E_{\mathrm{R}}^{xy}$). The dynamic tuning range of φ_{r} allows realization of two distinguishable symmetric double-well configurations at phases φ_1 and $\varphi_2 = \varphi_1 + \pi$. To initialize the first pumping step, short and long lattice depths are ramped to $49\,E_{\mathrm{R}}^{\mathrm{s}}$ and $100\,E_{\mathrm{R}}^{\mathrm{l}}$ respectively. If the bilayer system was created at $\varphi_{\mathrm{r}} \simeq \varphi_1$, φ_{r} is ramped within $5\,$ms from φ_1 to $\varphi_2 - \theta/2$, where $\theta = 0.15\,\pi$. Then the intra-well tunneling amplitude t_z is turned on, by ramping the short lattice down to $11\,E_{\mathrm{R}}^{\mathrm{s}}$ in $20\,$ms. The first pump is performed by sweeping the phase φ_{r} within $3\,$ms by an amount θ across the symmetric configuration φ_2 to a final value of $\varphi_{\mathrm{r}} = \varphi_2 + \theta/2$. During this phase sweep, the transport of atoms to opposite adjacent layers occurs. Eventually, the short lattice is ramped back to $49\,E_{\mathrm{R}}^{\mathrm{s}}$ and the next pump is performed at φ_1. Every subsequent pumping step is performed similarly at an alternating double-well configuration φ_1 or φ_2. These parameters were optimized for highest overall pump fidelity. Every pumping step separates the two initial layers by an additional distance $a_{\mathrm{l}} = 6\,\mu$m. Three pumps are used to reach a separation of $21\,\mu$m.

2.3.2 Bilayer imaging

A separation of $21\,\mu$m between two layers enables individual single-site resolved microscopy of each layer in our setup.

To demonstrate bilayer imaging, a bilayer Mott insulator was prepared and imaged. To this end, atoms were prepared in a single layer of the long vertical lattice and harmonically confined in the xy-direction. At fixed superlattice phase $\varphi_{\mathrm{r}} = 0$ for a balanced double well, the short lattice was ramped to a depth of $V_{\mathrm{s}} = 19\,E_{\mathrm{R}}^{\mathrm{s}}$ while at the same time the xy-lattice was ramped to $V_{xy} = 11\,E_{\mathrm{R}}^{xy}$. These lattice depths realize a ratio between the tunneling amplitudes of $t_z/t = 1.3$. The interaction strength was set to $U/t \simeq 50$. The motion of atoms was then quenched rapidly, by ramping to lattice depths $V_{\mathrm{s}} = 50\,E_{\mathrm{R}}^{\mathrm{s}}$ and $V_{xy} \simeq 40\,E_{\mathrm{R}}^{xy}$.

After three charge pumps, two successive fluorescence images were taken in the pinning lattice, as shown in Fig. 2.13. The imaging focus was adjusted from one layer to the next between the two images, by using a piezo-driven closed-loop objective scanner. In each image, the other layer contributes only a weak and homogeneous background, since the distance from focus is large compared to the $\sim 3\,\mu$m depth of focus of the imaging system. The background in each of the two images is neg-
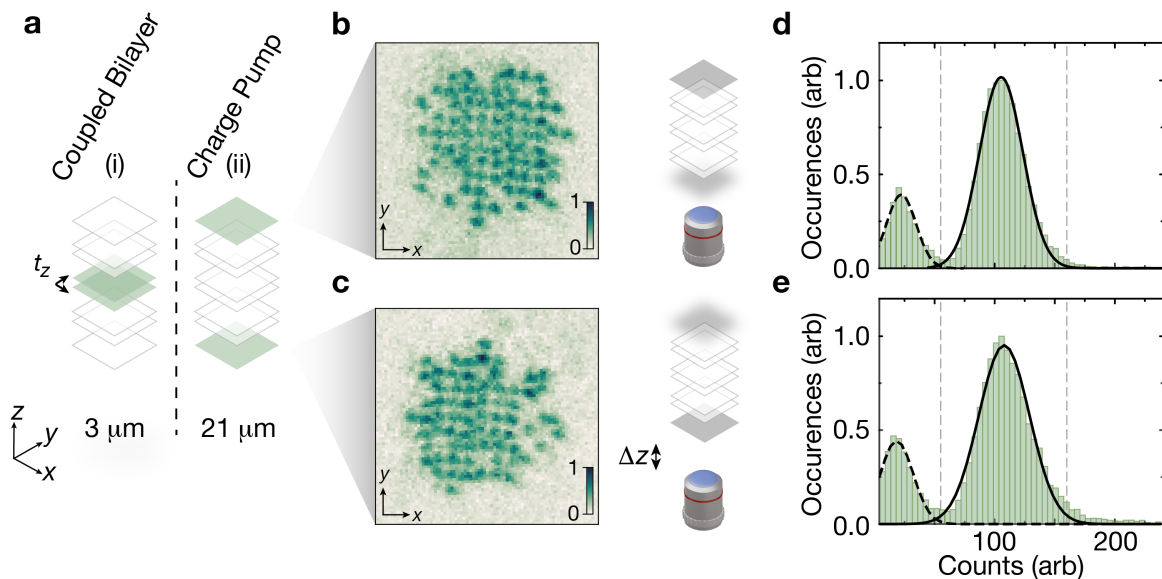
Figure 2.13: Bilayer microscopy. a, The two layers of an initially coupled bilayer Mott insulating system are separated by 21 μm in three charge-pumping steps. **b**, **c**, The large separation between both layers enables independent site-resolved microscopy of both layers in the pinning lattice by shifting the focus of the microscope objective between two subsequent images. **d**, **e**, Histogram of the counts per lattice site for each layer in a measurement run after deconvolution. Solid and dashed black lines are gaussian fits to the peaks of single and zero occupation. Vertical dashed gray lines denote the threshold for single and double occupation.

ligible, such that the previously used monolayer reconstruction algorithm [159] can be applied. Holes and occupied sites can be distinguished with 99.4 % fidelity, see Fig. 2.13d,e. The exposure per image was 2 s and is required to guarantee stable image quality.

There are possible routes to reduce the required exposure time in future experiments. Increasing the number of pumping steps and therefore a larger separation between layers can significantly boost the contrast between in- and out-of-focus layers. More laser power in Raman-cooling beams could enable a higher fluorescence rate. Finally, and probably most complicated, a second objective from the top would allow simultaneous imaging of both layers. With NAs higher than the 0.5 used here, a much more shallow depth of field would require less pumping steps.
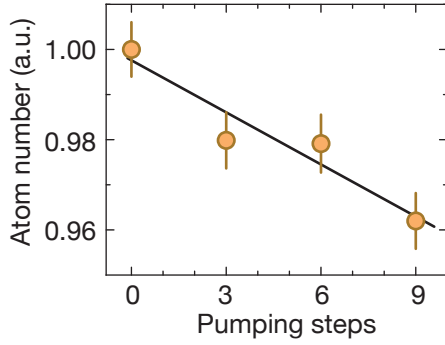
Figure 2.14: Charge-pump transfer fidelity. Averaged and normalized number of atoms in a monolayer system as a function of pumping steps. A fit to the data (black line) yields a transfer fidelity for each pumping step of $\eta = 0.996(1)$. Error bars denote one s.e.m..

2.3.3 Pump fidelity

To characterize how well the charge-pumping process preserves the physical system, several benchmarks were performed.

The probability η for a successful adiabatic transfer of an atom per pumping step was measured. Atoms were initialized in a single layer and the average total number of atoms in a target layer was tracked as a function of j pumping steps $j \in [0, 3, 6, 9]$. To avoid leaving the cooling region of the pinning lattice, the pump direction was reversed after $j = 3$. As shown in Fig. 2.14, a fit of the data to the exponential η^j yields a high single-pump efficiency of $\eta = 0.996(1)$.

The main limitations for η are the vertical harmonic confinement and vertical potential corrugations, originating from the current xy-lattices. The spatially changing potential landscape causes different conditions for both pumping directions with an increasing number of pumping steps, such that the optimal pumping parameters for opposite directions start to differ strongly. This is one of the reasons, why pumping is currently restricted to $j \leq 3$. Another reason for the limit to 21 μm is the finite cooling region available, which is set by the pinning lattices and their waists of 50 μm.

The xy-motion of atoms is frozen out during the pumping procedure. To confirm that the density and its fluctuations of the initial physical system are preserved, the properties of a monolayer system with and without pumping were compared. The excellent agreement found in appendix A.4 indicates the conservation of all relevant observables. Furthermore, the strong antiferromagnetic correlations measured with an extended method, as presented in one of the following sections, demonstrate the high fidelity of the bilayer-imaging technique.

Figure 2.15:　Bilayer Fermi-Hubbard systems. Fermions can hop between neighboring sites between layers with amplitude t_z and within a layer with amplitude t. The vertically-summed occupations across both layers can be represented as the occupation of a super site. As shown in this snapshot, the occupation of individual layers can strongly fluctuate, while the super-site occupation shows a suppressed fluctuation. Such a reduction in super-site fluctuations indicates insulating behavior and is expected in the strong coupling regime $t_z/t \gg 1$.
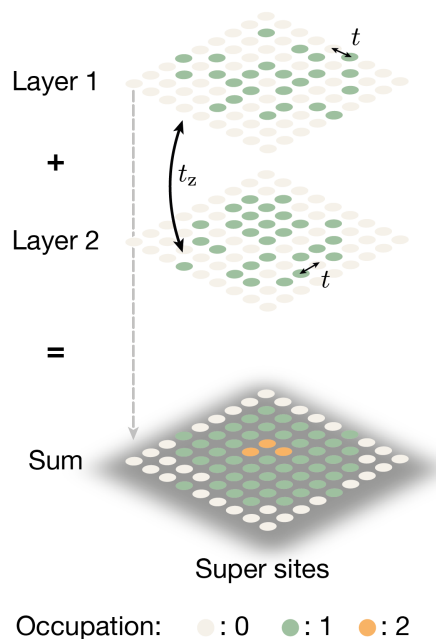
2.4　Bilayer Fermi-Hubbard systems

High-T_c materials often consist of weakly-coupled bi- or even tri-layers. The critical temperature was found to increase with an increasing number of layers and this layered structure is considered an important ingredient to explain several experimental features [13, 190, 191]. Bilayer imaging enables exploration of the microscopic physics of bilayer Fermi-Hubbard systems. This section gives a brief introduction to the parameter regimes accessible with the experimental setup. In addition to the bilayer Mott insulator from the previous section, snapshots of a bilayer band insulator and a dimer Mott insulator are presented. This demonstrates that also strong inter-layer couplings $t_z/t \gg 1$ can be realized to study the effect of layered structures on the competition between magnetism and doping with fully tunable couplings in the future.

The bilayer Fermi-Hubbard model is obtained by vertically coupling two 2d Fermi-Hubbard systems with a nearest-neighbor hopping amplitude t_z between layers, see Fig. 2.15. This model is the most basic attempt to capture the physics of layered materials and it could so far be studied numerically [192–199].

Most interestingly, weakly coupled doped Fermi-Hubbard layers $t_z < t$ might have a factor ~ 2 higher T_c, as compared to uncoupled layers [196, 198]. The bilayer Fermi-Hubbard model and its two Fermi surfaces were also proposed as an approach to interpolate the physics from cuprates to pnictides [200].

At half filling and strong repulsive interactions, a Mott insulator emerges with antiferromagnetic spin couplings between nearest-neighbor sites. In the Heisenberg limit, the vertical tunneling amplitude t_z drives a quantum phase transition from antiferromagnetic long-range correlations at $J_z/J < 2.53$ to a disordered phase at $J_z/J > 2.53$ [201–203]. The critical tunnel-coupling therefore corresponds to $t_z/t \simeq 1.6$. This transition connects to a metal to band insulator transition at weak interactions, which was numerically explored in [192, 199]. In the case of weak interactions and at strong tunnel couplings $t_z > t$, a dimerization process takes place, which turns a half-filled system into an insulator. This dimerization phenomenon is relevant for oxide heterostructures [204] and is considered an important building block of 2d organic salts, where the dimerization leads to the formation of effective 2d triangular lattice systems [205, 206].

In the experiment, bilayer Fermi-Hubbard systems can be realized by creating a vertical double-well potential with an enhanced intra-well coupling $t_z = t_1$ and suppressed inter-well coupling $t_2 = 0$. Particles can therefore only hop within and between exactly two layers.

2.4.1 Band insulator

A bilayer system can turn into an insulator at half filling without interactions. This state emerges through dimerization when $t_z/t > 4$ and is called a band insulator [192, 199]. Similar to other fermionic band insulators at unit filling, the driving mechanism is the Pauli-exclusion principle.

In a non-interacting bilayer system, particles have a bandwidth $W = 8t$ within a single layer. When the tunnel coupling t_z is sufficiently strong, two vertically nearest-neighbor sites form a super site with two local orbital-like states. These orbital-like states correspond to the symmetric and antisymmetric superposition of the upper and lower layer, see Fig. 2.16a. The energy difference between the two states is $2t_z$. In the extreme case of $2t_z > 8t$, the energy splitting of the two orbital states exceeds the inter-layer bandwidth.

At half filling and in the limit $2t_z > 8t$, one two-dimensional band of width $8t$ is completely full and the other band, separated by $2t_z$, completely empty. The bilayer system, therefore, transforms into an insulating quasi-2d system. Each fermion is fully dimerized between the two layers. The system can be thought of as a 2d lattice of super sites, on which each particle occupies the lower orbital. Since there are two spin states available, the band insulator has exactly two particles localized on a super site.

An experimental snapshot of a band insulator is shown in Fig. 2.16b,c. The lattice depths in this setting were $V_x = V_y = 11\,E_R^{xy}$, $V_s = 12\,E_R^s$ and $V_l = 105\,E_R^l$. The scat-
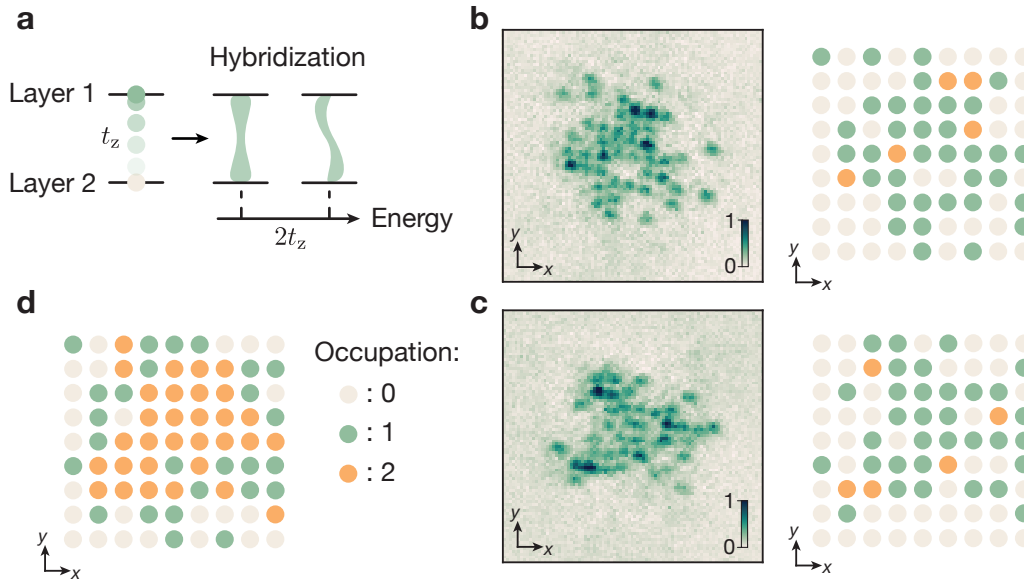
Figure 2.16: Bilayer band insulator. a. At strong inter-layer coupling $t_z/t > 4$ and weak interactions, atoms hybridize between both layers. A single atom occupies the sites of both layers at the same time and another same-spin atom cannot hop on any of those sites because the energy cost $2t_z > 8t = W$ is higher than the single-particle bandwidth W in a 2d layer. **b,c**, Bilayer-resolved snapshot of a band-insulating state. Individual layers show strong fluctuations in occupations. **d**, The sum layer reveals a core of supersites with fixed occupation of two (two spin states), indicating band-insulating behavior.

tering length was $a_{sc} = 137\,a_0$, such that $2t_z = 1246\,\text{Hz}$, $U = 320\,\text{Hz}$, $8t = 760\,\text{Hz}$. The occupation in each layer fluctuates strongly, as if the system was in a metallic state. But the super-site occupation reveals the strong correlation between both layers. Already the single snapshot features suppressed density fluctuations in its central super-site core.

2.4.2   Dimer Mott insulator

In the presence of strong inter-layer coupling $2t_z > 8t$ and strong interactions $U > 8t$, dimerization and repulsion lead to the emergence of a quasi-2d Mott insulating state at quarter filling. The resulting state is referred to as dimer Mott insulator [205, 206], whose charge gap is determined by a combination of both mechanisms [207]. Similar to the band-insulating state, the 2d system is comprised of super sites and particles in the lower orbital on each site, see Fig. 2.17a. The strong repulsion prevents two opposite spins to dimerize on the same super site.
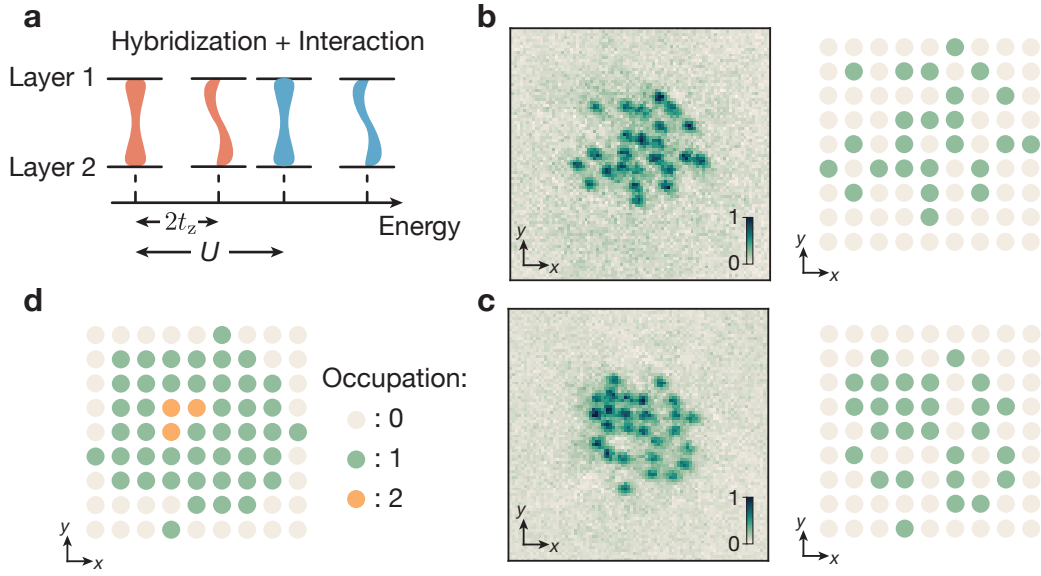
Figure 2.17: Dimer Mott insulator. a, At strong inter-layer coupling $t_z/t > 4$ and strong repulsive interactions $U/t > 8$, atoms hybridize between both layers, similar to the bilayer band insulator. Hybridization prevents same-spin atoms to occupy the same supersite, while the strong repulsion does not allow opposite-spin atoms on the same supersite. **c, d**, Bilayer-resolved snapshot of such a dimer-Mott-insulating state. Individual layers show strong fluctuations in occupations. **d**, The sum layer reveals a core of supersites with fixed occupation of one, indicating insulating behavior.

A snapshot of a dimer Mott insulator is shown in Fig. 2.17b,c. The lattice depths in this setting were $V_x = V_y = 11\,E_R^{xy}$, $V_s = 12\,E_R^s$ and $V_l = 105\,E_R^l$. The scattering length was $a_{sc} = 2000\,a_0$, such that $2t_z = 1246\,\text{Hz}$, $U = 4692\,\text{Hz}$, $8t = 760\,\text{Hz}$. The system features metallic fluctuations of occupations in the individual layers. However, in the combined super-site system the local suppression of fluctuations is visible, see Fig. 2.17d. In the central core super sites have a fixed occupation of one.

Conclusion

The novel vertical superlattice setup and its application for bilayer microscopy extend the realm of quantum simulation to layered structures. The presented states demonstrate the access to tunable bilayer systems, which enables future studies of the quantum phase transition at half filling [201] or the competition of magnetism and doping in bilayer systems [196, 198].

2.5   Spin and density resolution for a monolayer

Resolving the density and spin information (full resolution) in 2d cold-atomic Fermi-Hubbard systems is highly desirable. Fully-resolved static [57, 58] and dynamic studies [69] of the spin-charge separation phenomenon in 1d demonstrate the unique observables and capabilities afforded by the access to complete information.

Traditional quantum gas microscopy lacks the ability of full resolution. Parity projection during imaging leads to indistinguishability of holes and doublons [46, 47]. The collected fluorescence light is independent of the spin and Raman-sideband cooling methods for common atomic species do not preserve the hyperfine state. Therefore, it is only possible to collect information on one spin component in a single snapshot by removing the other spin component before imaging. The removed spin then appears as holes in the image [54, 55]. These circumstances severely limit observables for doped 2d Fermi-Hubbard systems, in which the most important mechanism is the interplay between holes and spins.

Some approaches to spin-resolved detection include the use of vector light shifts [145] or dark states [208]. Unfortunately, such species-dependent tools are not available for some of the most common fermionic atoms, such as ^{6}Li. As discussed in section 2.1.1, the small electronic level splittings of lithium complicate state-dependent optical manipulation schemes.

Here, we show how bilayer microscopy can be used to obtain full resolution of a monolayer system. The idea of spin resolution based on multilayer readout was demonstrated for bosonic rubidium before [141], but its fidelity relied on the ability to suppress the fluorescence rate in individual layers during the imaging process. The charge pump employed in our scheme overcomes this problem and realizes a species-independent solution.

In contrast to our previous scheme for spin and density resolution [56], the bilayer method can also be used for non-lattice 2d systems by using an ancillary detection lattice. Furthermore, the new technique enables higher energy scales of the underlying 2d Hubbard system and more than doubles our system size at full resolution.

2.5.1   Spin splitting

Full resolution of a monolayer with two spin components is achieved, by first splitting the spins into adjacent planes of a bilayer system with a magnetic gradient. Then bilayer readout is performed and the single-site resolved information of both layers is combined to reconstruct the state of the parent monolayer system.

In the experiment, full resolution is implemented for 2d Fermi-Hubbard systems,
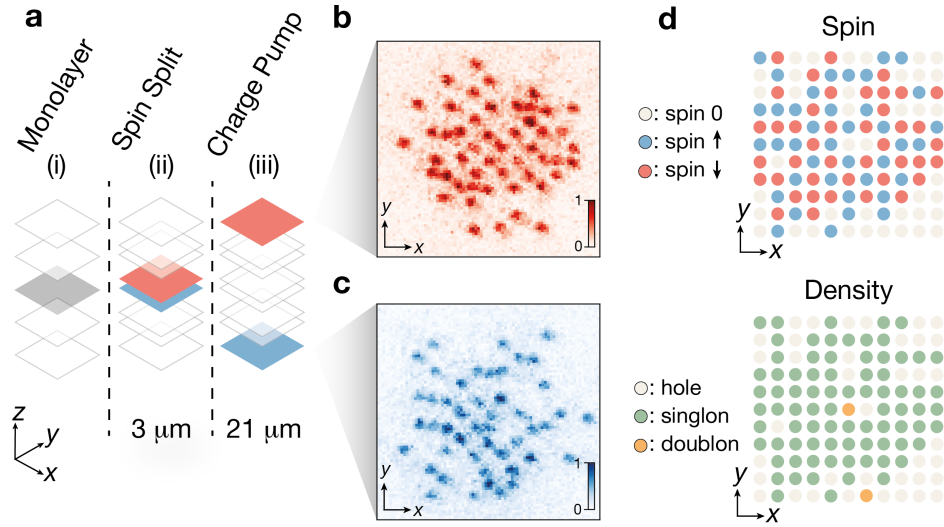
Figure 2.18: Spin and density resolution of a monolayer. a, The two different spin states of a monolayer spin mixture (here a 2d Fermi-Hubbard system) are split into different layers (red/blue) of a bilayer system with a vertical magnetic gradient. Subsequently, charge pumping and bilayer readout is applied with single-site resolution. **b,c**, Snapshots of the two spin components of a single 2d Fermi-Hubbard realization. **d** Reconstructed spin (upper panel) and density (lower panel) information of the underlying 2d parent state.

see Fig. 2.18. First, the motion of atoms is frozen in a deep xy-lattice and the monolayer is prepared in a single layer of the long vertical lattice. Then a strong vertical magnetic field gradient of $45\,\mathrm{G/cm}$ is applied to exert a force on the two spin states in opposite directions. The magnetic offset field is kept below $13\,\mathrm{G}$ to maximize the differential magnetic moments between the two lowest hyperfine states of $^{6}\mathrm{Li}$, c.f. Fig. 2.1b. The superlattice phase is set to the symmetric double-well configuration $\varphi_{\mathrm{r}} = 0$ and the short lattice is turned on adiabatically to $49\,E_{\mathrm{R}}^{\mathrm{s}}$. This sequence realizes a Stern-Gerlach type separation of the two spin components into two adjacent planes of the bilayer optical lattice. In combination with three charge pumps and bilayer microscopy, each spin state can be read out separately and the full spin and density information of the parent system can be reconstructed. How the correct combination of the two spin layers is ensured to recover the initial system is described in appendix A.5.

To confirm accurate spin splitting into a bilayer system, the occupation imbalance of the resulting two spin layers is measured for a broad range of different phases φ_{r}. A strong magnetic gradient creates an opposite double-well tilt for each spin, which upon adiabatic turn-on of the short lattice initializes spins in opposite wells. In a spin-

Figure 2.19: Spin splitting. Number of atoms detected in the upper (red) or lower (blue) layer as a function of the relative superlattice phase used for spin splitting. A strong magnetic gradient is present during the adiabatic ramp-up of the short lattice. Accurate splitting for a balanced spin mixture is realized across a width of phases $\sim$ 300 mrad.
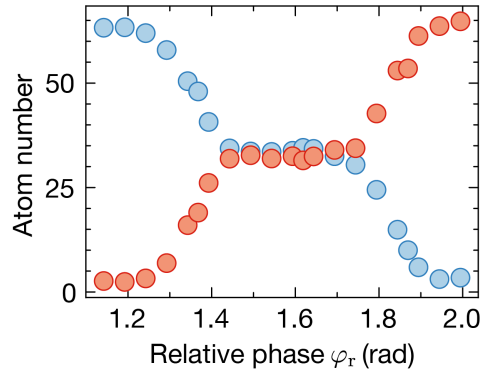
balanced system, splitting manifests itself as a balanced occupation in both layers for a large range of superlattice phases during ramp-up of the short lattice. As long as the spin-dependent tilt is stronger than the tilt from a phase $\varphi_r \neq 0$, spins will be separated deterministically. Successful splitting of spins is achieved in the experiment for a width of phases $\sim$ 300 mrad, as shown in Fig. 2.19. The spin detection is therefore robust against superlattice phase changes by more than an order of magnitude more than the upper bounds for phase noise and drifts in this setup.

To further benchmark the fidelity of the bilayer technique for full resolution, density observables of a Mott-insulating system can be compared between two different detection methods. As analyzed in appendix A.4, the density and its fluctuations measured with monolayer spin-unresolved imaging and with bilayer-based full resolution are in excellent agreement.

2.5.2 Spin-spin correlations

A first more stringent test for the bilayer spin-resolution technique is the measurement of spin correlations in a 2d Mott insulator. Antiferromagnetic correlations are expected to arise in such a system when the temperature drops below the superexchange energy J, c.f. chapter 1.

Mott insulating systems with about 90 atoms were realized at lattice depth of $6.9(1)\,E_R^{xy}$ and interaction strength $U/t = 9.3(4)$. Two point correlations ($\eta = 4$) are computed from fully-resolved snapshots, c.f. chapter 1.4. As shown in Fig. 2.20, strong antiferromagnetic correlations are found, whose sign alternates as a function of the distance d between spins. The spin-structure factor $S(\boldsymbol{q})$ features a peak at the antiferromagnetic quasimomentum $\boldsymbol{q} = (\pi, \pi)$.

The detection of these intricate correlations furthermore underlines the fidelity of the bilayer method. The next section discusses, how such spin correlations at half
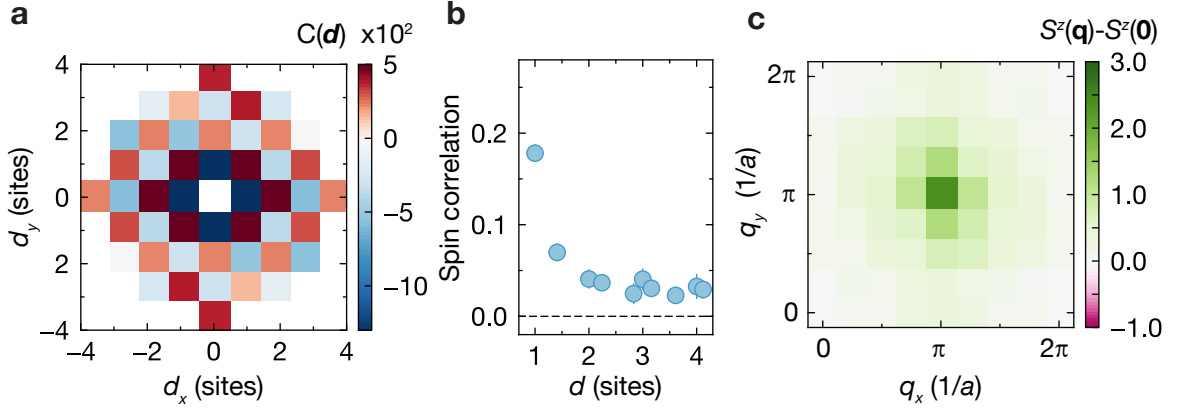
Figure 2.20: Spin correlations in 2d systems. a. Averaged spin correlations $C(d)$ versus distance d in 2d Fermi-Hubbard systems around half filling at U/t = 9.3(4), obtained by spin- and density-resolved imaging. Sites with density n < 0.84 were excluded from the analysis. The normalization $\eta = 4$ is used for correlations. **b**, Sign-corrected spin correlations $(-1)^{d^2} C(d)$ versus distance d. Error bars, where visible, denote one s.e.m. **c**, Spin-structure factor, exhibiting a strong peak at the antiferromagnetic momentum (π, π). The figure is based on 150 experimental realizations.

filling can be used as a thermometer. Correlations in Fig. 2.20 are compatible with temperatures down to $T \sim 0.8\,J$. This temperature is close to the lowest temperature of $T = 0.5\,J$ [61] reported for ultracold 2d Fermi-Hubbard systems.

2.6 Thermometry

To determine the exact temperature at which atomic systems are realized within this thesis, we compare spin correlations at half filling between experimental data and data from numerical-linked-cluster-expansion (NLCE) calculations of [209]. Observables from NLCE data were obtained by resumming up to ninth order using Wynn's algorithm [210].

The temperature of Fermi-Hubbard systems presented in this work is quantified in units of the hopping amplitude t or the superexchange J. The repulsive on-site interaction U relates both energy scales through $t = U/t \cdot J/4$. A different interaction strength leads to a different ratio t/J. An important consequence is that at fixed entropy a different U/t can e.g. lead to a different temperature in units of J.

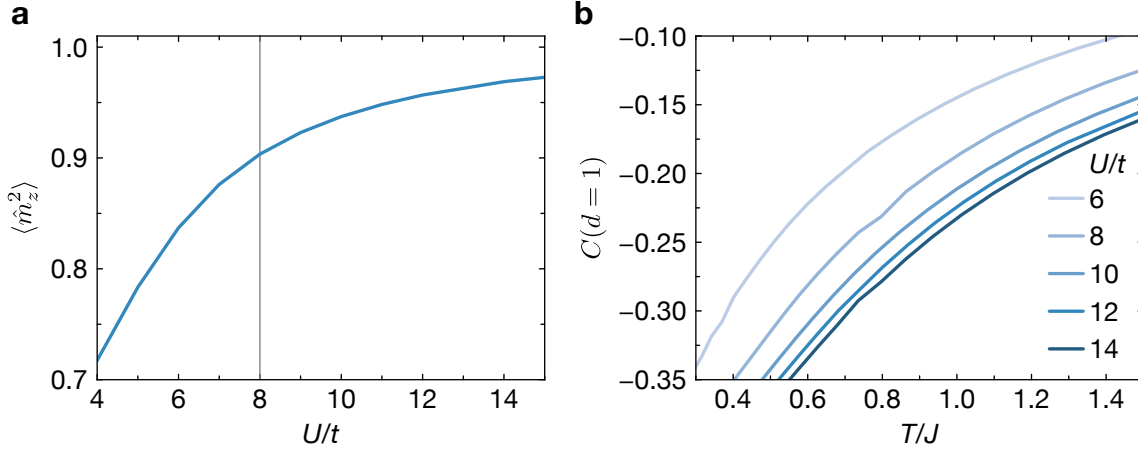The spin physics close to the Mott insulating regime crucially depends on the tem-

Figure 2.21: Thermometry with NLCE calculations. a, On-site magnetic moment in 2d Fermi-Hubbard systems at half filling as a function of interaction strength at a temperature of $T = 0.34\,t$. At these temperatures, the on-site magnetic moment is approximately independent of T. **b**, Nearest-neighbor spin correlation ($\eta = \eta_{\text{Pearson}}$) at half filling as a function of temperature for different interaction strengths. All curves are based on NLCE data of [209], which was resummed up to ninth order with Wynn's algorithm [210].

perature in units of J instead of t. As shown with NLCE data in Fig. 2.21b, the nearest-neighbor ($d = 1$) spin correlation ($\eta = \eta_{\text{Pearson}}$) at half filling and for $U/t > 8$ scales universally as a function of temperature in units of J. For different U/t, the temperature in units of t can be very different, but as long as the temperature is the same in units of J, spin correlations are similar. This universality towards the Heisenberg limit is not surprising, but important to keep in mind, as temperatures are often reported in units of t.

At half filling, an increasing interaction suppresses doublon-hole fluctuations and drives the system into the Heisenberg limit. The on-site magnetic moment measures how close the system is to the limit of localized spin-1/2 particles

$$\langle \hat{m}_z^2 \rangle = 4\langle \hat{S}_i^z \hat{S}_i^z \rangle = 4\sigma(\hat{S}_i^z)^2 = \eta_{\text{Heis}}/\eta_{\text{Pearson}} \ . \tag{2.10}$$

As shown with NLCE data in Fig. 2.21a, an interaction strength of $U/t = 8$ marks the point from which the system asymptotically approaches $\langle \hat{m}_z^2 \rangle = 1$ (Heisenberg limit) with increasing interaction. The on-site magnetic moment is very sensitive around $U/t = 8$ and can therefore act as a probe for the experimentally realized U/t, which is otherwise inferred from our calibrated system parameters.

In particular for temperatures well below J or for doped systems, numerical calculations are difficult to obtain and thermometry independent of such comparisons is

required in the future. A promising approach is based on the fluctuation-dissipation theorem. If the response function and fluctuations of an observable can be measured for a system, the theorem allows the direct and comparison-free computation of the temperature. As an example, the temperature can be extracted from knowledge of the compressibility and all density correlations of the system [63, 64].

3 🔍

Imaging magnetic polarons

A single dopant in a 2d antiferromagnetic Mott insulator causes a fierce competition between kinetic and magnetic energy. As described in chapter 1, experimental and theoretical investigations suggest the dopant forms a magnetic polaron. A textbook feature of polarons is the bubble-like dressing cloud, which constantly surrounds the original impurity (the dopant). In this chapter, a real space observation of such a magnetic dressing cloud is presented. When the competition between kinetic and magnetic energy is artificially suppressed by prohibiting delocalization of the dopant, the dressing cloud is absent. Results of the following publication are contained in this chapter (numerical calculations were performed by our theory collaborators):

- **Imaging magnetic polarons in the doped Fermi-Hubbard model**.
  J. Koepsell, J. Vijayan, P. Sompet, F. Grusdt, T.A. Hilker, E. Demler, G. Salomon, I. Bloch and C. Gross. Nature **572**, 358-362 (2019).

3.1 Introduction

3.1.1 Polarons - dressed charge carriers

When a mobile charge carrier, such as an electron or hole, travels through a medium and strongly interacts with its surrounding, it locally polarizes the medium and thus forms a polaron [211–213], see Fig. 3.1. The polaron is a quasiparticle, which consists of the initial charge carrier and a local cloud of excitations dressing the mobile particle. There are different types of collective background modes, which can dress the charge carrier. Examples are phonons, magnons, or spinons [213]. The properties of a particle change, when it turns into a polaron quasiparticle[1]. The effective mass can be strongly altered and even self-trapping can occur. Also, the mutual interaction between two polarons is different from the bare interaction of electrons, which means under certain conditions polarons can bind to form a bipolaron.

---

[1]Note the difference between polaron quasiparticles and the Fermi-liquid quasiparticles introduced earlier. In a Fermi liquid, quasiparticles form through interactions between charge carriers. Polarons
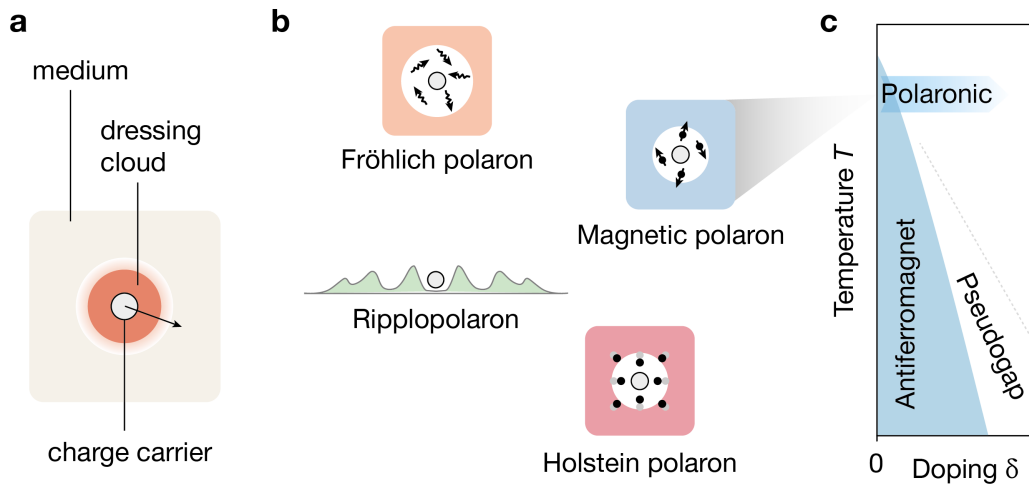
Figure 3.1: Polarons. a, A polaron can emerge when a charge carrier travels through a medium and strongly couples to its environment. A hallmark feature of a polaron is its dressing cloud, which accompanies the charge carrier at all times. **b**, Depending on the medium and its collective excitations, different types of polarons exist. **c**, Doped holes or doublons in Mott insulators can form magnetic polarons. In this case, the dressing cloud consists of a local reduction of antiferromagnetic correlations.

Polarons are ubiquitous in condensed-matter systems and their relevance goes far beyond high-T_c ceramics [213], see Fig. 3.1. Historically, polarons were considered in the context of electron-phonon coupling [211, 212]. Depending on the coupling, there exist Fröhlich polarons [214] or Holstein polarons [215, 216] with large or small dressing clouds. But the polaron concept can be applied to a large variety of different media and couplings, giving rise to a rich zoo of polaron types, see Fig. 3.1. Jahn-Teller polarons occur, when the mobile particle interacts with local rotational or vibrational excitations [217, 218]. When electrons are placed on the 2d surface of liquid ^{4}He, they interact with ripplon excitations of the liquid surface and form ripplopolarons [213, 219], which can experience self-trapping [220]. As discussed in chapter 1.2.3, a dopant in a 2d antiferromagnetic Mott insulator strongly couples to the magnetic environment and can form a magnetic polaron.

In strongly-correlated materials, the presence of polarons often results in the emergence of exotic properties. A possible explanation for colossal magnetoresistance in manganites is a magnetic-field induced breakup of immobile bipolarons into mobile polarons [221–223]. Furthermore, at low temperatures, the polaronic metal in such

---

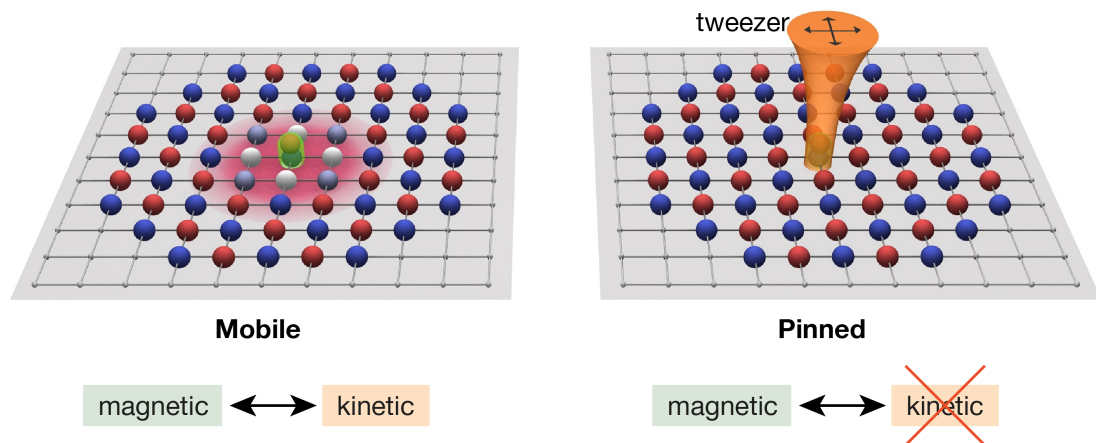emerge from interactions of charge carriers with a background medium.

Figure 3.2: Mobile and pinned dopant in 2d Fermi-Hubbard systems. When a dopant (here doublon) is mobile and able to delocalize, it forms a magnetic polaron and is constantly surrounded by a magnetic dressing cloud. In contrast, when the dopant is pinned and unable to move, the competition between kinetic and magnetic energy is suppressed, which inhibits magnetic-polaron formation.

manganites exhibits pseudogap behavior [224], which is a phenomenon also found close to the magnetic-polaron regime of doped cuprates [15]. In semiconductors, the electron-phonon interaction can be particularly strong. Polarons in some organic semiconductors become self-trapped and give rise to pure spin currents [225], which is an important building block of spintronics. There are many open questions to these exotic phenomena and how they are related to polarons or interacting multi-polaron systems [24, 30, 111, 222].

Individual polarons are often probed with transport or spectroscopic methods. However, a direct image of the dressing cloud and how the medium is transformed by the charge carrier remains inaccessible in traditional solid-state experiments. This chapter reports on a real-space image of the magnetic dressing cloud of individual dopants in cold-atom 2d Fermi-Hubbard systems.

3.1.2 Magnetic polaron: dressing and undressing

The motion of a dopant in a 2d antiferromagnetic Mott insulator leads to a local distortion of magnetic correlations, as discussed in chapter 1.2.3. A single mobile dopant forms a magnetic polaron [101–107] and is constantly surrounded by a dressing cloud of altered spin correlations (spin bag [103]), see Fig. 3.2. It is the motion of the dopant, which couples to the spin sector and creates a competition between kinetic and magnetic energy. This means the mobility of a dopant is expected to be an important

prerequisite for magnetic-polaron formation.

For an immobile dopant, the absence of its motion avoids coupling to the antiferromagnetic correlations in its vicinity, see Fig. 3.2. Consequently, no dressing cloud is expected to form. In cuprates, this scenario of localized non-magnetic impurities corresponds to doping with Zn [226]. Experiments and numerics indicate the absence of polaronic effects, but instead suggest the possibility of enhanced antiferromagnetic correlations through geometric effects [227, 228].

In the experiment, such a mobile and pinned setting was realized in the single dopant regime to reveal the stark contrast between the two settings. Results presented in the following sections demonstrate that dopant mobility is an essential ingredient for magnetic-polaron formation.

3.2   Experimental setting

This section describes the two different experimental settings for which in total 42 671 spin- and density-resolved images were taken. These snapshots are the basis for the analysis of mobile and pinned doublons and their magnetic environment in the next section. Here, the characteristics of the experimental 2d Fermi-Hubbard system and its background spin-spin correlations as well as the pinning procedure are described.

Dopants considered in this chapter are doublons. The harmonic confinement of the optical lattice represents an anti-trapping potential for holes and a trapping potential for doublons. Choosing doublons as dopants, therefore, has two advantages for the following experiments. Doublons are trapped in the central and most homogeneous part of the lattice, where they can delocalize in a flat region. Furthermore, holes created during the detection will not contaminate the signal of doublon dopants.

3.2.1   Mobile and pinned doublons

For measurements in this chapter, the bichromatic superlattice for bilayer readout of chapter 2 was not yet implemented. Full spin- and density-resolution of Fermi-Hubbard systems was achieved by the use of an in-plane monochromatic superlattice [56]. This alternative method implements spin splitting by using a superlattice and a magnetic gradient within the monolayer. The details of this detection scheme are not relevant for the results in this chapter, which is why the reader is referred to [56] for its description. A major drawback of this in-plane method is a longer lattice spacing in the y-direction. This leads to lower energy scales and smaller system sizes when compared to the bilayer method of chapter 2.

In this chapter, lattice spacings (a_x, a_y) in x- and y-direction are $(1.15, 2.3)\,\mu$m. To
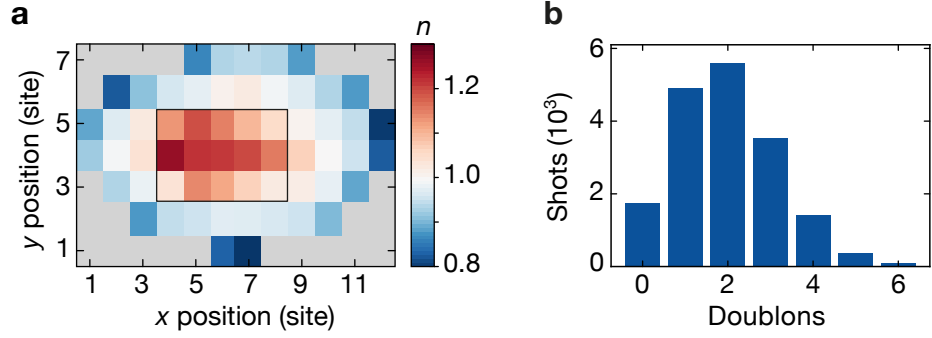
Figure 3.3: Mobile doublons. a Density distribution (n) for the mobile doublon setting. Only sites with density $n \geq 0.7$ are shown. In the doped region (inner black box), on average 1.95(1) doublons delocalize in an area of 5×3 sites. **b,** Number of snapshots with the respective number of doublons in the doped region (black box of **a**).

obtain a symmetric implementation of the Hubbard model, different lattice depths of $(8.6\, E_R^x, 3\, E_R^y)$ in x- and y-direction are used to realize symmetric tunneling amplitudes $t_x/h = t_y/h \approx 170\,\text{Hz}$. The scattering length was set to $2150\, a_0$ to achieve an interaction strength of $U/t = 14(1)$ and a resulting ratio of tunneling and superexchange of $t/J = 3$. The total duration for the adiabatic lattice ramp-up was 210 ms.

Doping was controlled by evaporation parameters, which determine the final number of particles in the lattice. Above a specific number of atoms, the harmonic confinement leads to the formation and delocalization of mobile double occupations (doublons) in the center of the trap. For the given lattice parameters, a calibration curve of the total number of atoms versus doping can be found in appendix B.1.

Mobile

The setting of individual mobile doublons was realized with on average 72 atoms in the lattice. The resulting density n_i in the system for all lattice sites i with $n_i > 0.7$ is shown in Fig. 3.3a. Doublons can also occur in Mott insulators due to short-lived quantum fluctuations. This process is suppressed with increasing U/t, but at our settings a chance of $\sim 3\,\%$ per lattice site for such a fluctuation remains, see appendix B.1 or c.f. Fig. 2.21. Doublon-hole fluctuations can be identified by the hole, which the fluctuation leaves behind on a nearest-neighbor site, see appendix B.2. To distinguish doped doublons from such fluctuations, we consider only doublons without a hole as a direct nearest-neighbor. As shown in Fig. 3.3, on average 1.95(1) doped doublons delocalize on the central 5×3 sites. The full histogram of the number of mobile doublons in all snapshots is shown in Fig. 3.3a. In the cases with more than one doublon,
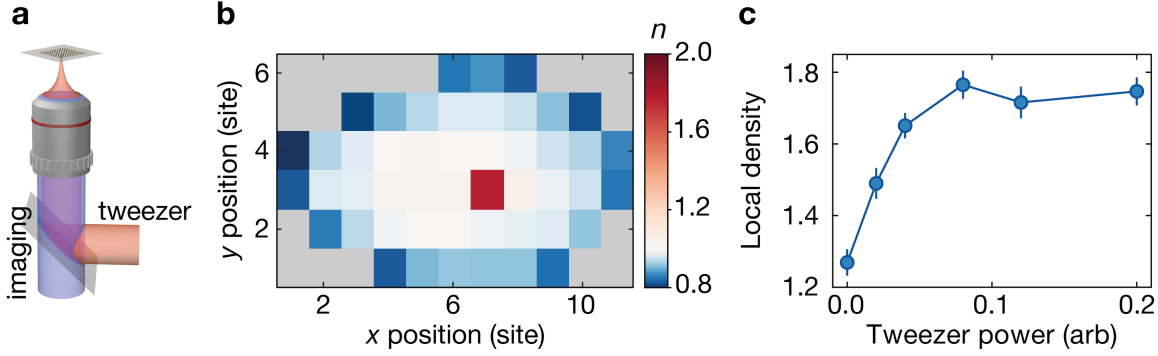
Figure 3.4: Pinned doublons. a. An attractive laser beam (tweezer) is focused by the objective onto a single lattice site. **b**, Density distribution (n) for the pinned doublon setting. Only sites with density $n \geq 0.7$ are shown. **c**, The local density on the target lattice site as a function of the tweezer-beam intensity. At optimized settings, the density on the target site is 1.77(1).

dopants are anti-correlated at nearest-neighbor sites and uncorrelated otherwise in our system, see Fig. B.2. This behavior is akin to free fermions and furthermore justifies an independent treatment of detected doublons in the following analysis. For the mobile setting 33 669 images were taken.

Pinned

Localized doublons were created with a tightly-focused attractive pinning beam, which induces a strong dip in the optical potential when aimed at a single lattice site, see Fig. 3.4a. To this end, a collimated red-detuned beam of $\lambda = 702$ nm was overlapped with the optical path of the fluorescence light and focused through the high-NA objective to a waist of about $0.5 \, \mu$m. The intensity of this beam was turned on adiabatically at the same time the lattices were ramped up to create a double occupation trapped on a single lattice site. The final intensity of the pinning beam was optimized and saturates at an average occupation on the target lattice site of 1.77(1) with a doublon-density of $\langle \hat{d} \rangle = 0.74$, see Fig. 3.4. The residual densities on that site for a hole, singlon and triplon were $\langle \hat{h} \rangle = 0.07$, $\langle \hat{s} \rangle = 0.13$, $\langle \hat{t} \rangle = 0.05$. In particular the triplon occupation is an effect, which arises in these measurements due to the long lattice in the y-direction and its smaller energy gaps. To ensure the presence of only a single pinned doublon, systems of 55 particles were used to avoid doublon doping in the central region. For the pinned setting 9 002 images were taken.

All further analysis was performed in a region of interest, which is given by all lattice sites with a density $n \geq 0.7$. These lattice sites are shown in Fig. 3.3, 3.4. Prior
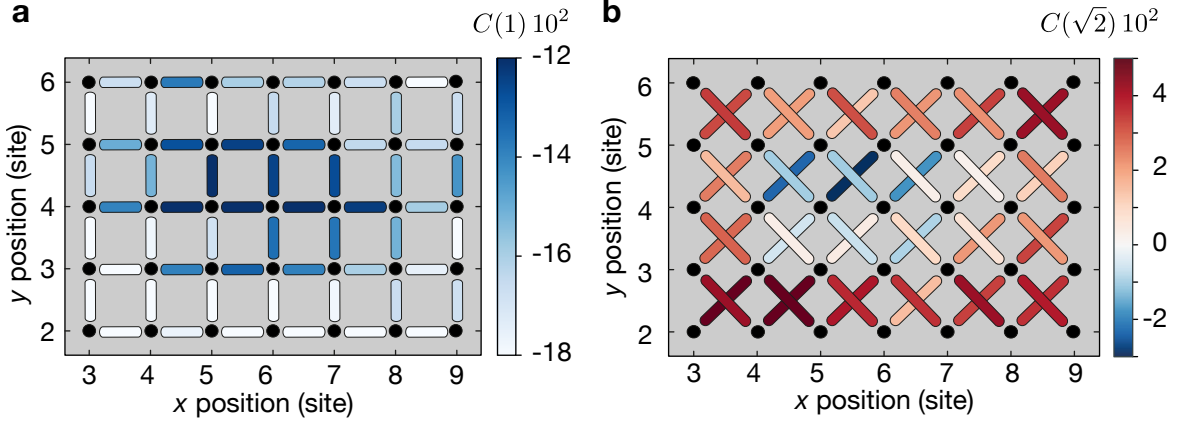
Figure 3.5: Two-point spin correlations. Average spin correlations in the system with mobile doublons for **a**, NN bonds ($d = 1$) and **b**, diagonal bonds ($d = \sqrt{2}$). Doping in the central region significantly alters correlations, as compared to the undoped outer region.

to evaluating correlations in our two different systems, some snapshots were filtered out and discarded from the evaluation for technical reasons, see appendix B.3.

3.2.2 Spin-spin correlations and temperature

A prerequisite for the observation of magnetic polarons is the existence of antiferromagnetic correlations between spins in the Mott insulator, which compete with the delocalization of the doublon.

Spin correlations computed in this chapter use the normalization $\eta = 4$. In addition and exclusive to this chapter, correlations are evaluated on singly-occupied sites. This means the correlation is only computed when a spin is located on each site. Technically, this corresponds to a special normalization of spin correlations with $\eta = 4/\langle \hat{s}_{r_i} \hat{s}_{r_j} \rangle$, where $\hat{s}_r$ is the singlon-density operator on the two lattice sites r_i and r_j. In the absence of singlon correlations (e.g. in the Mott regime) and at very high $U/t \gg 8$, this simplifies to a renormalization by the density.

The spatial variation of two-point spin correlations can be visualized with the bond representation of chapter 1.4.2. The color of a bond connecting two lattice sites quantifies the strength of the spin correlation between those sites.

Correlations for bond lengths $d = 1$ and $d = \sqrt{2}$ are shown in Fig. 3.5 for the system with mobile doublons in the center. As expected for the Mott insulating region, nearest-neighbor spins are negatively correlated and diagonal spins are positively correlated. In the central region, where doublons delocalize, correlation strengths are

strongly reduced. Diagonal bonds even reverse their sign to be negatively correlated between sites of highest doping. This sign reversal of average diagonal two-point correlations has also been observed in [54, 55, 72].

The temperature of the system can be estimated by comparing spin correlations around half filling to NLCE calculations of [209], as mentioned in chapter 2.6. For this set of measurements we find consistency with $T/t = 0.45^{+3}_{-1}$, see appendix B.4.

The average reduction of spin correlations is expected when dopants are added to the system. Mobile doublons hop in the center of the trap and form a delocalized magnetic polaron. Therefore, every bond in the center is reduced on average. On the other hand, when post-selecting on a doublon at a specific position the reduction should always be found in the immediate vicinity of the doublon. Such spin-charge (spin-density) correlations are presented in the following section.

3.3   Doublon-spin-spin correlations

Here, we use a three-point spin-charge correlator to study spin correlations in the reference frame of dopants. A dressing cloud surrounding mobile doublons is revealed with a compact size of around two sites in diameter. For pinned doublons the magnetic dressing is strongly suppressed.

3.3.1   Probing with spin-charge correlators

The presence of delocalized doublons reduces the average antiferromagnetic correlations everywhere in the doped system, as presented in the previous section. If a doublon forms a magnetic polaron, a strong reduction of antiferromagnetic correlations locally surrounds the dopant. Since the magnetic polaron itself is delocalized in the system, the distorted correlations of the dressing cloud should appear in the lattice at different positions for every image, depending on where the doublon is detected. Therefore, spin correlations averaged over all snapshots are reduced because in some cases a magnetic polaron was present in a specific region.

Based on fully spin- and density-resolved snapshots, spin correlations in the reference frame of a doublon can be studied. In each snapshot, the position of a doublon was found and the correlation of spins computed as a function of distance from the dopant. Such an analysis corresponds to evaluating the three-point spin-charge correlator

$$C_{\bullet_{r_3}}(r_1, r_2; r_3) = \eta \langle \hat{S}^z_{r_1} \hat{S}^z_{r_2} \rangle_{\bullet_{r_3}} \,, \tag{3.1}$$
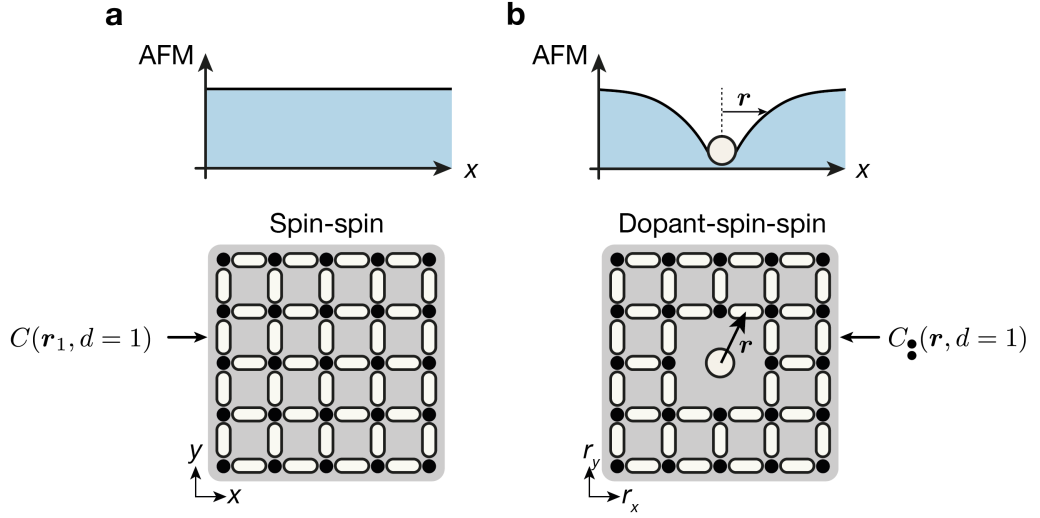
Figure 3.6: Visualizing spin-charge correlations in the bond picture. a, The background medium for magnetic polarons are antiferromagnetic spin correlations in a Mott insulator. Their local strength can be visualized in the bond picture. Here NN ($d = 1$) spin-spin correlations are visualized as white bonds. The measured correlation strength will be represented by the bond color. **b**, The effect of a dopant on the local antiferromagnetic background can be studied by measuring spin-spin correlations in the reference frame of dopants. For a magnetic polaron, the dressing cloud of reduced antiferromagnetic correlations is expected to decrease with increasing bond distance r from the dopant.

which measures the spin correlation between two sites r_1 and r_2, conditioned on a doublon at a third position r_3. This correlator measures bare correlations, i.e. it contains both the connected and disconnected part, c.f. chapter 1.4.3. For now, we are interested in the bare spin environment of dopants, but an analysis of the connected part will be performed as part of the following chapter. As mentioned in the previous section, the used normalization for spin correlations is $\eta = 4$, evaluated on singly-occupied sites only.

Eq. 3.1 can be rewritten in terms of the bond length $d = r_2 - r_1$ and the distance between the bond and the dopant $r = [(r_1 + r_2)/2] - r_3$

$$C_{\bullet_{r_3}}(r, d; r_3) = C_{\bullet_{r_3}}(r_1, r_2; r_3). \tag{3.2}$$

For each experimental snapshot of the mobile setting, doublons are detected at different positions r_3. By averaging Eq. 3.2 over all doublons found at positions r_3 within the finite 5×3 doped region (indicated in Fig. 3.3a), $C_{\bullet}(r, d)$ is obtained. This correlator measures the average bond strength at bond length d as a function of distance

r from a doublon. For the setting of immobile doublons, post-selection is performed w.r.t. doublons on the pinned lattice site.

The visualization of $C_\bullet(r, d)$ with the bond representation is ideally suited to reveal the magnetic dressing cloud. In the previous section, correlation maps for fixed bond length d were used to show the spatial dependence of correlations within the lattice, c.f. Fig. 3.6a. Fig. 3.6b shows how $C_\bullet(r, d)$ can be plotted at fixed $d = 1$ as a function of spatial distance r from the dopant at the origin. This bond representation will be used for different d to visualize results in the following sections.

3.3.2 Revealing the dressing cloud

In order to decide which bond length d of the correlator $C_\bullet(r, d)$ to investigate first, a simple argument can be considered. The four spins, which are the nearest neighbor of a doublon, should be most affected by the motion and delocalization of the dopant. Hence, the largest polaronic signal is expected for correlations between these four neighboring spins of a detected doublon. These correlations are diagonal $d = \sqrt{2}$ and next-nearest neighbor (NNN) $d = 2$ bonds. The NN correlations $d = 1$ closest to the doublon, by contrast, exhibit a larger minimal bond distance r and are less sensitive to polaronic effects. Furthermore, there are eight NN bonds at closest distance to the doublon, over which the polaronic signal will distribute. But there are only four diagonal bonds and two NNN bonds at closest distance. Therefore, we start by analyzing the correlator $C_\bullet(r, d)$ with diagonal bonds as a function of bond distance r from doublons.

Diagonal bonds

The dressing cloud of mobile doublons as detected with diagonal bonds $d = \sqrt{2}$ is shown in Fig. 3.7a. Spin correlations $C_\bullet(r, \sqrt{2})$ are strongly affected in the vicinity of the doublon ($r \sim 1$), while being unharmed at larger distances ($r \gg 1$). This observation confirms the picture of a magnetic polaron, which consists of a doublon locally dressed by a spin disturbance. The dressing effect, therefore, already exists at the elevated temperatures $T = 0.45\,t$ of the experiment. Diagonal bonds at closest distance to the doublon even reverse the sign of their correlation from positive to negative.

When the doublon is pinned to a single site, the spin disturbance almost disappears completely, see Fig. 3.7b. This confirms the competition between kinetic and magnetic energy as the key mechanism behind magnetic-polaron formation. Magnetic correlations around the trapped site are only moderately reduced compared to the undoped background.
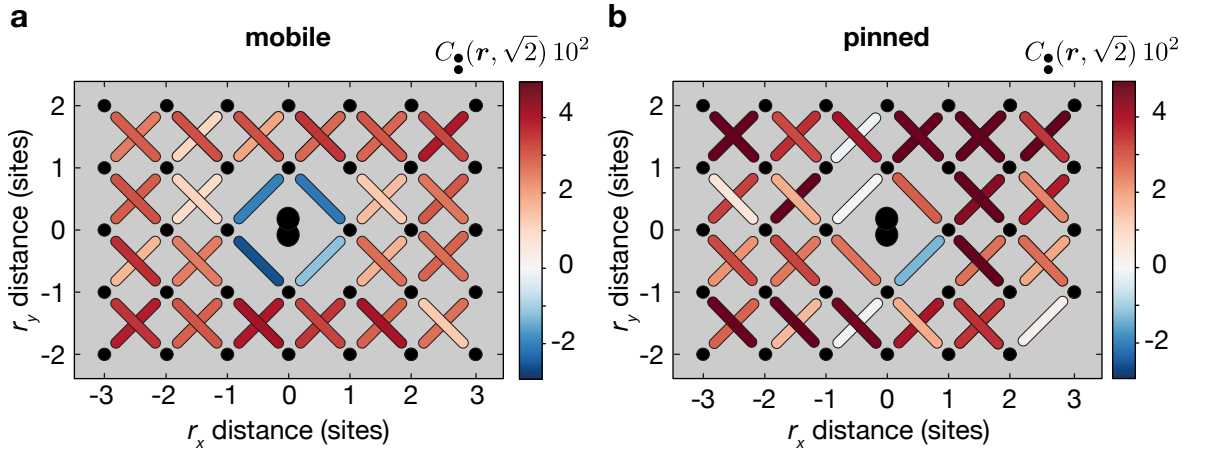
Figure 3.7: Diagonal correlations. Evaluating the spin-charge correlator $C(\boldsymbol{r}, \boldsymbol{d})$ for diagonal correlations $d = \sqrt{2}$. Correlations surrounding **a**, mobile and **b**, pinned doublons. In the vicinity of mobile doublons, correlations reverse their sign from positive to negative.

NN and NNN bonds

The presence or absence of a dressing cloud for mobile or pinned doublons can also be investigated with NN ($d = 1$) or NNN ($d = 2$) bonds. As shown in Fig. 3.8, the two different mobilities lead to very different results.

The strong negative correlation of NN bonds is reduced in the vicinity of the mobile doublon. This ferromagnetic influence on NN bonds (i.e. making a bond more positive) is an important signature effect of polarons, which only exists in the doping regime of magnetic polarons, as outlined in the following chapter. For the pinned doublon, there is no reduction, but a slight increase of NN correlations in the vicinity. This enhancement effect originates from imperfections of the optical tweezer potential, which will be discussed in greater detail at a later stage.

Similar to the sign reversal of closest distance diagonal bonds, the NNN bond across the mobile doublon (see Fig. 3.8c) exhibits a strong negative correlation, while NNN bonds at half filling are positively correlated. Correlations directly across the pinned doublon (see Fig. 3.8d) are not as strong as the background NNN correlations. The pinned doublon effectively blocks a path on which the two sites can exchange their spin, such that at finite temperature the correlation is weakened.
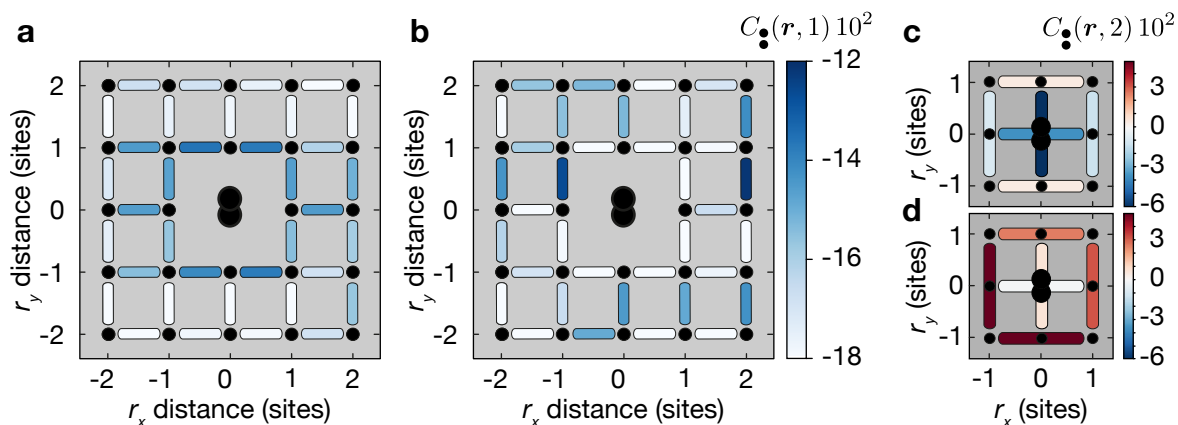
Figure 3.8: Nearest- and next-nearest-neighbor correlations. Nearest-neighbor correlations ($d = 1$) in the vicinity of **a**, mobile and **b**, pinned doublons. A reduction of negative correlations is visible next to mobile doublons. Next-nearest-neighbor correlations ($d = 2$) for **c**, mobile and **d**, pinned doublons. Spins are negatively correlated across mobile doublons.

Sign flip

An interpretation of the sign reversal of diagonal and NNN correlations at closest distance to the dopant is ambiguous. In the context of magnetic polarons, this feature was observed in numerical calculations [111, 229] and has been interpreted as local spin-charge separation and a building block of incommensurate magnetism in two dimensions [229, 230]. In stripe phases found at much lower temperatures, several dopants form a line (stripe) and mutually align their flipped correlations to create a coherent parity flip for antiferromagnetic correlations across the stripe. On the other hand, in chapter 4, negative diagonal correlations are also found next to dopants in the weakly-interacting Fermi liquid, where polarons are absent. However, an important difference between the polaron and Fermi-liquid regime must be emphasized. Average diagonal spin correlations are positive in the magnetic polaron regime and negative in the Fermi liquid. Therefore, a negative correlation close to a dopant only represents a sign flip in the magnetic polaron regime.

An intuitive explanation for the sign flip can be found in the limit where the orientation of spins is frozen (frozen-spin approximation), i.e. $t/J \gg 1$. A single hop of a dopant exchanges NN bonds with diagonal bonds in its vicinity, see Fig. 3.9. Since spins are not allowed to flip within this time scale, the detected diagonal correlation bond next to the doublon is negative. At our finite temperatures, NN bonds are strongly negative, while diagonal bonds are positive at intermediate strengths. Therefore, doublon delocalization mixes strong negative bonds with much weaker positive
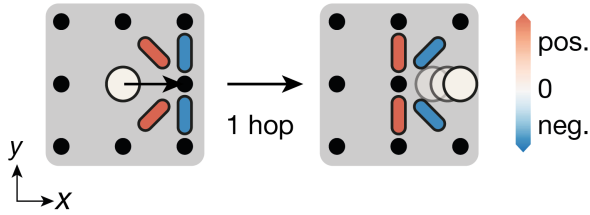
Figure 3.9: Frozen-spin picture. In the limit of $t/J \gg 1$, spins cannot react to the dynamic motion of a dopant. A single hop of a dopant turns diagonal bonds into nearest-neighbor bonds and vice versa.

bonds, which on average results in a negative correlation close to the doublon.

Radial dependence and theory comparison

To enable a quantitative study and to extract the size of the dressing cloud, correlations with the same absolute bond length d and bond distance r are averaged. In Fig. 3.10 a,b,c the dependence of NN, diagonal, and NNN bonds on the bond distance r is shown. Correlations quickly recover towards their undoped value with increasing distance from the mobile doublon. The size of the dressing cloud therefore has a diameter on the order of ~ 2 lattice sites. Furthermore, the sign reversal of correlations in the mobile case is absent for the pinned doublon.

At this point, a comparison to numerical calculations (provided by F. Grusdt and E. Demler) can be performed, see Fig. 3.10 d,e,f. For the mobile scenario, we compare to three-point correlations in the string-model for magnetic polarons at the experimental temperature [231]. As introduced in chapter 1.2.5, this is a simplified model, which describes the polaron as a bound state between a spinon and holon and is motivated by the frozen-spin approximation ($t/J \gg 1$) [107]. Remarkably, similar amplitude changes of correlations, and hence a similar polaron radius, is predicted by the string model (and also the t-J model, as found in the supplementary information of [231]). Furthermore, the sign changes of diagonal and NNN correlations in the vicinity of the doublon are reproduced in this model. Some quantitative differences between experimental and numerical data remain. However, this is expected owing to limitations of the frozen-spin approximation (here $t/J = 3$) and experimental details, such as elevated temperatures, the harmonic confinement, and the occasional presence of more than one dopant.

For the pinned doublon, we compare to exact diagonalization calculations of the t-J model at the experimental temperature and with zero tunneling of the excess doublon in a 4×4 system [231]. In agreement with experiment and numerics, closest-distance diagonal and NNN spins are uncorrelated for the pinned scenario. As mentioned before, this can be explained by the fact that the doublon effectively blocks a path linking the spins next to it. The missing link prevents the neighboring spins from building up a correlation, given the finite temperature of the system. The lo-
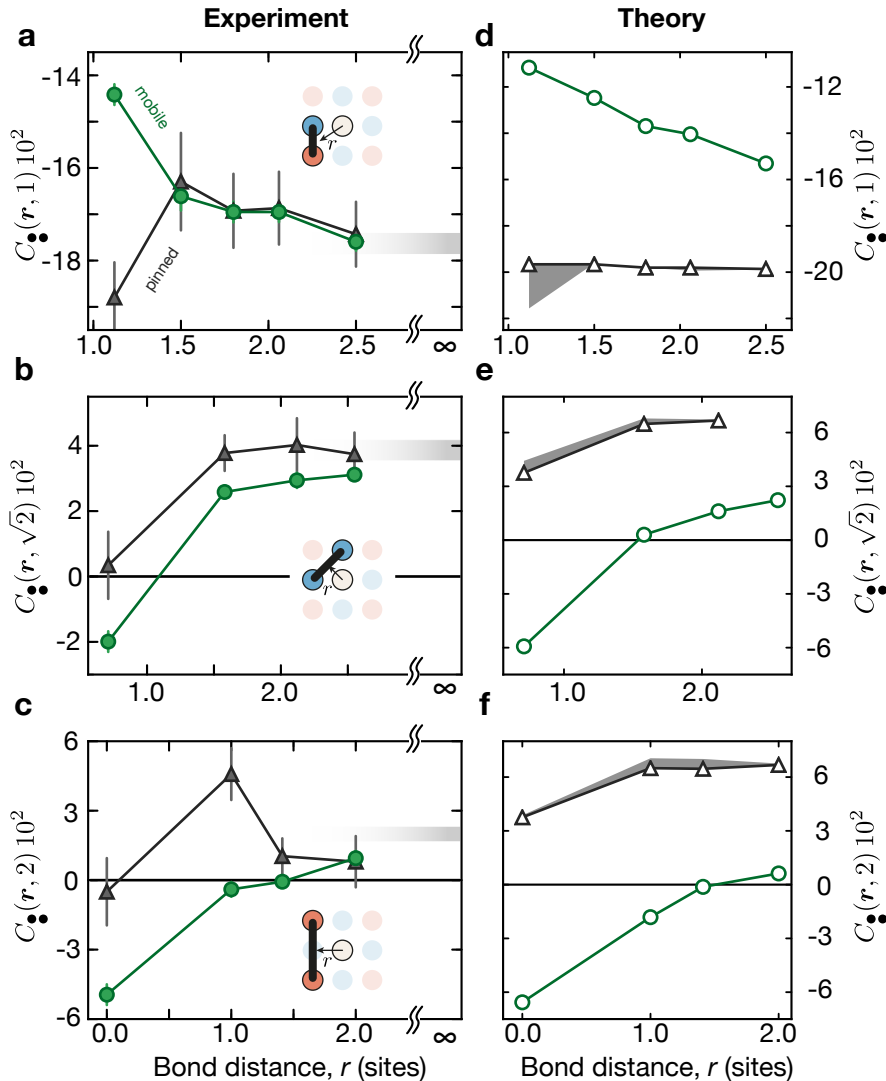
Figure 3.10: Spin correlations versus bond distance from doublons. Comparison between experiment (**a-c**) and numerical calculations at the experimental temperature (**d-f**). The mobile setting (green) is compared to calculations of the string model for magnetic polarons. The pinned setting (black) is compared to exact diagonalization of a single doublon in the *t-J* model without hopping. Considered bond lengths are NN (**a**, **d**), diagonal (**b**, **e**) and NNN (**c**, **f**). The strength of two-point correlations in the undoped regime is indicated as a gray band at distance ∞, with a width corresponding to two s.e.m. The finite size of the tweezer beam leads to a slight enhancement of some NN and NNN correlations next to the pinned doublon (see text). This effect is captured by exact diagonalization with 10% enhanced spin exchange on neighboring sites of the pinned doublon, indicated as a black band in the theory panel.

cal enhancement of NN bonds observed in the experiment close to the pinned site originates from parasitic energy shifts exerted by the optical tweezer on lattice sites in the immediate vicinity, see appendix B.5. Those energy shifts lead to a locally enhanced superexchange coupling J and can, therefore, cause stronger correlations. If an increased superexchange up of to 10 % is taken into account in the exact diagonalization calculations at finite temperature, the experimentally observed enhancement is reproduced. Correlations across the pinned doublon and the shortest bond-distance diagonal correlations are hardly affected by such a 10 % systematic enhancement of the superexchange.

3.4   Conclusion

This chapter presented a real-space picture of the polaronic dressing cloud of single dopants in a 2d Mott insulator. A three-point spin-charge correlator revealed a compact polaron size of about two sites in diameter and an inner structure of sign-reversed spin correlations. By confining the dopant to a single lattice site, the competition between kinetic and magnetic energy could be lifted and the dressing cloud disappeared. Therefore, the magnetic polaron can be understood as a result of this competition.

Dynamic or spectroscopic measurements can be employed to study the effective mass, quasiparticle weight, or formation time of magnetic polarons in cold-atomic systems in the future. First indications of a suppressed timescale for delocalization were found in dynamic experiments [70]. By implementing angle-resolved photoemission spectroscopy techniques for cold atoms [65, 68, 232], the relation between magnetic polarons and the pseudogap could be investigated. Furthermore, the ability of quantum gas microscopes to spatially resolve the dressing cloud could be used to study other polaron types, such as impurities immersed in bosonic [233] or fermionic quantum gases [234, 235].

Another direction of research is the effect of dimensionality on magnetic polarons. 1d systems behave very differently than the 2d systems discussed within this thesis. Spin-charge separation features an independent propagation of holons and spinons in 1d Fermi-Hubbard chains, as studied in [57, 58, 69]. In analogy to the 1d-2d crossover studied in [58], a crossover from 2d to bilayer systems could be studied with the layered readout of chapter 2.

Since this chapter found essential features of the complex interplay between magnetism and doping to be present already at experimental temperatures, intuitive follow-up question in 2d are: What happens if more and more dopants are added? Could potential polaron-polaron interactions be resolved and at which dopant

concentration does the polaron picture break down? Is it possible to detect features reminiscent of the lower-temperature physics? When and how does the system evolve into a Fermi liquid at high dopings? These and other questions will be addressed in the following chapter, which is based on the updated experimental apparatus with larger and more homogeneous systems.

4
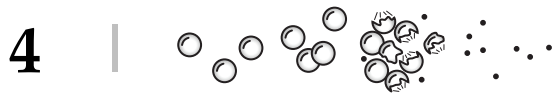
Two metals - polarons dissolving into Fermi liquid

Magnetic polarons reside in 2d Mott insulators at weak dopings. At strong dopings, the system forms a Fermi liquid with conventional quasiparticles. The transformation between these two metallic regimes is the subject of this chapter, which reveals how microscopic correlations at temperatures around $T = 0.4\,t$ evolve as a function of doping. The polaronic dressing cloud of dopants, as revealed in the previous chapter, evolves into a fully negatively correlated environment in the Fermi liquid. Antiferromagnetic correlations surrounding pairs of holes peak at the crossover between both regimes and might be a precursor of the lower temperature physics. Weak incommensurate magnetic fluctuations develop in the Fermi liquid. The transformation between both regimes completes at a doping of around $\delta_{FL} \sim 30\,\%$. Results of the following publication are contained in this chapter (numerical calculations were performed by our theory collaborators):

- **Microscopic evolution of doped Mott insulators from polaronic metal to Fermi liquid**.
  J. Koepsell, D. Bourgund, P. Sompet, S. Hirthe, A. Bohrdt, Y. Wang, F. Grusdt, E. Demler, G. Salomon, C. Gross and I. Bloch. pre-print, arXiv:2009.04440 (2020).

4.1 Introduction

This chapter combines all puzzle pieces introduced within this thesis to explore one of the least understood crossovers of strongly-correlated electrons: the doping-induced transformation of a 2d Mott insulator into a Fermi liquid. This section briefly summarizes important aspects and introduces the connected part of spin-charge correlators, which will be studied in this chapter.
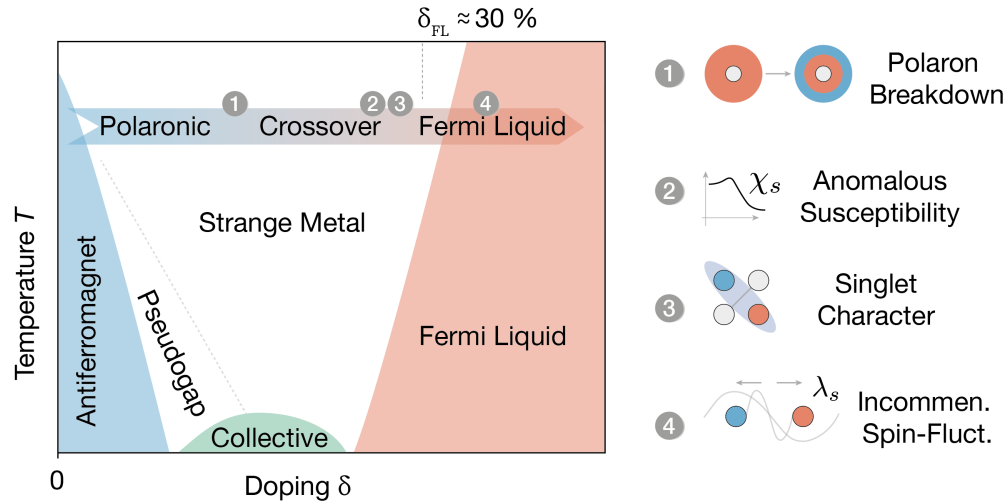
Figure 4.1: From polarons to Fermi liquid in doped Mott insulators. This chapter probes doped Mott insulators along the indicated arrow in the conjectured phase diagram of the 2d Fermi-Hubbard model (c.f. Fig. 1.5). Spin-spin as well as higher order spin-charge correlators are studied. Some of the main results are summarized by the insets.

4.1.1   From polaronic metal to Fermi liquid

Chapter 1 described how increasing doping of Mott-insulating materials at intermediate temperatures, such as cuprates, leads to at least two distinct metallic regimes. Doping induces an anomalous metallic phase, which at some specific doping (for cuprates $\sim 20\%$) abruptly turns into a conventional Fermi liquid [18, 19]. Remarkably, it is this specific doping value at which the highest transition temperatures for d-wave superconductivity occur [10]. The pseudogap and strange metal behavior of the anomalous metallic regime violate the description of conventional metals and pose major questions to their understanding.

The 2d Fermi-Hubbard systems studied in this thesis are closely related to the physics of cuprates [14]. A similar transformation between an anomalous and a conventional metal is expected to occur, which is driven by a competition between magnetic and kinetic energy. The paradigmatic transformation can be studied using novel observables, such as higher-order spin-charge correlators. These correlators are experimentally accessible by the implemented bilayer technique, as demonstrated in chapter 2, which enables spin- and density-resolved microscopy of 2d Fermi-Hubbard systems.

Chapter 3 explored the weak doping limit and employed a three-point spin-charge correlator to reveal the presence of a magnetic dressing cloud surrounding single dou-

blons in Mott insulators. Close to the Mott-insulating regime, doping leads to a metal of magnetic polarons.

Here, we study how the polaronic metal dissolves into a conventional Fermi liquid by doping Mott insulators continuously through all doping regimes, see Fig. 4.1. We track the evolution of two-point correlations and extract the uniform spin susceptibility and the spin structure factor. Three-point hole-spin-spin as well as four-point hole-hole-spin-spin correlations are evaluated to study the interplay between dopants and spins as a function of doping. All these observables undergo a significant change across a specific doping value of $\delta_{\text{FL}} \sim 30\,\%$. We perform a comparison to several numerical calculations such as exact diagonalization and mean-field-inspired approaches. Furthermore, calculations of diverse theoretical concepts such as the string model and RVB states are provided. Particularly in the crossover regime, none of the presented weak-doping concepts describes the experimental data, calling for more efficient frameworks.

Before diving into the experimental settings and analysis, it is helpful to recapitulate some correlators introduced so far. A novel hole-hole-spin-spin correlator is added to the portfolio and increases the maximum correlation order to four. Therefore, it becomes important to analyze correlations in terms of their connected part, which contains the new information of order N gained from an N-point correlator.

4.1.2 Connected spin-charge correlators

Bare multi-point correlations can arise from contributions of lower-order (disconnected) parts. Connected correlations contain the new information carried by a correlator, as discussed in chapter 1.4. When analyzing correlations of different orders it is useful to disentangle their mutual contributions. Therefore, this chapter entirely focuses on connected correlators, which are summarized in Fig. 4.2.

In this chapter, we performed doping with holes, because we are interested in observables at varying doping and the harmonic confinement naturally leads to such a hole-doping variation from the center to the edge of our system. We consider balanced spin mixtures $\langle \hat{S}^z_{r_i} \rangle = 0$ and spin-spin correlations are normalized with $\eta = \eta_{\text{Pearson}} = 1/(\sigma(\hat{S}^z_1)\sigma(\hat{S}^z_2))$.

Spin-spin

In spin-balanced systems, connected and bare spin-spin correlations are identical (c.f. Chapter 1.4)

$$C^c(\boldsymbol{r}_1, \boldsymbol{r}_2) = \eta(\langle \hat{S}^z_{\boldsymbol{r}_1} \hat{S}^z_{\boldsymbol{r}_2} \rangle - \langle \hat{S}^z_{\boldsymbol{r}_1} \rangle \langle \hat{S}^z_{\boldsymbol{r}_2} \rangle). \tag{4.1}$$
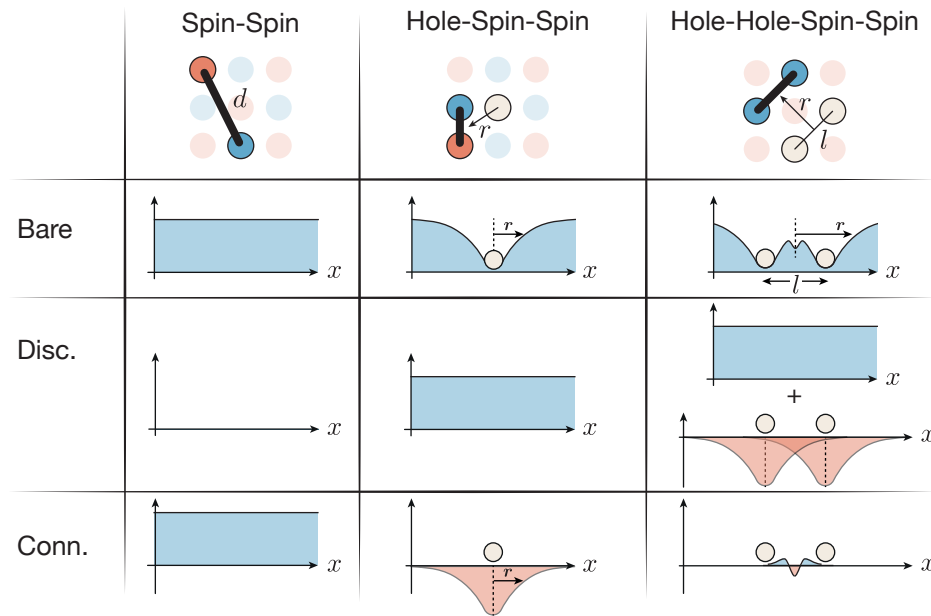
Figure 4.2: Connected spin-charge correlators. Cartoon illustration of correlators and their decomposition. This chapter focuses on connected correlations. Bare correlations can be divided into disconnected and connected part. Their contributions simplify in spin-balanced mixtures and can be understood intuitively as shown here. The weighting factor γ for hole-hole-spin-spin correlations has been neglected in this illustration.

Given a bond length d, the correlator can be averaged over sites within a spatial region Ω for fixed d to yield

$$C^c(d) = \sum_{r_1 \in \Omega} C^c(r_1, d)/\Omega = \sum_{r_1 \in \Omega} C^c(r_1, r_2)/\Omega. \tag{4.2}$$

Hole-spin-spin

The three-point correlator introduced in the previous chapter measured two-point spin correlations in the presence of a dopant at a third position r_3. Now we consider the same correlator, but with hole dopants instead of doublons. Chapter 3 focused entirely on the bare strength $C(r_1, r_2; r_3)_\circ$ of this correlator and compared its value to spin-spin correlations $C^c(r_1, r_2)$ without the dopant. This comparison was an indirect measure of the connected correlation between the dopant and the spin background. In this chapter, we look directly at the connected part of the three-point correlator, which is given by

$$C^c_\circ(r_1, r_2; r_3) = C_\circ(r_1, r_2; r_3) - C^c(r_1, r_2) \ . \tag{4.3}$$

As illustrated in Fig. 4.2, the connected part measures how the dopant changes correlations locally w.r.t. to the two-point value.

Using the definition of bond distance r from the hole (c.f. chapter 3), the correlator can be averaged over holes detected within a spatial region Ω for fixed (r, d) to obtain

$$C_\circ^c(r, d) = \sum_{r_3 \in \Omega} C_\circ^c(r, d; r_3)/\Omega = \sum_{r_3 \in \Omega} C_\circ^c(r_1, r_2; r_3)/\Omega. \tag{4.4}$$

A simple example can be considered to gain an intuition for the connected part of this three-point correlator. In the case of a magnetic polaron, the connected part of the closest-distance NN bond ($r = \sqrt{1.25}, d = 1$) will have a positive sign. The dopant reduces the strong negative NN bond, which means it adds a positive connected correlation on top of the strong negative two-point correlation. The connected part added to the background two-point value yields the bare spin environment surrounding the dopant.

Hole-hole-spin-spin

To search the magnetic environment of two holes for possible interaction effects, we introduce a hole-hole-spin-spin correlator. It measures spin-spin correlations in the presence of a hole at positions r_3 and r_4 each. The bare correlator contains many lower-order contributions, which can all be understood intuitively, see Fig. 4.2. The connected part measures how much the spin bond is affected by the presence of exactly two holes

$$C_{\circ\circ}^c(r_1, r_2; r_3, r_4) = C_{\circ\circ}(r_1, r_2; r_3, r_4) - C^c(r_1, r_2) - \gamma(C_\circ^c(r_1, r_2; r_3) + C_\circ^c(r_1, r_2; r_4)). \tag{4.5}$$

The weighting factor is given by $\gamma = \langle \hat{h}_{r_3} \rangle \langle \hat{h}_{r_4} \rangle / \langle \hat{h}_{r_3} \hat{h}_{r_4} \rangle$. The bare strength $C_{\circ\circ} = \eta \langle \hat{S}_{r_1}^z \hat{S}_{r_2}^z \rangle_{\circ r_3 \circ r_4}$ of a spin-spin bond surrounding a pair of holes is composed out of the background two-point correlation C^c, the impact $C_\circ^c$ on the bond from a single hole at r_3, the impact $C_\circ^c$ on the bond from a single hole at r_4 and finally the two-hole impact $C_{\circ\circ}^c$, which is the connected part of the four-point correlator.

The mutual distance of the two holes can be defined as $l = r_3 - r_4$ and the bond distance r is measured w.r.t. the center of mass of r_3 and r_4. Using these definitions, the correlator can be averaged over holes detected within a spatial region Ω for fixed (l, r, d) to obtain

$$C_{\circ\circ}^c(l, r, d) = \sum_{r_4}^{\Omega} C_{\circ\circ}^c(l, r, d; r_4)/\Omega = \sum_{r_4}^{\Omega} C_{\circ\circ}^c(r_1, r_2; r_3, r_4)/\Omega. \tag{4.6}$$

The above expressions hold for perfectly balanced systems. For all experimental points, the more general expression with imbalanced systems was evaluated to avoid

biases from residual magnetizations. These full expressions can be found in appendix C.3.

4.2 Experimental setting

To evaluate multi-point correlations in 2d Fermi-Hubbard systems at different dopings, spin- and density-resolved snapshots were taken at different settings with the updated apparatus. This section presents the experimental parameters for all datasets and describes how the doping dependence of correlators is extracted from the naturally varying spatial doping distribution within the system and the control of total particle number in the trap. Furthermore, numerical calculations used for comparisons are summarized and an overview of their different expected validity regimes is given.

4.2.1 Continuous doping control

In this chapter, doping was performed with holes. Fermi-Hubbard systems were realized at strong interactions $U/t \sim 8$ and the acquired experimental data can be grouped into four different datasets [D1, D2, D3, D4]. Datasets [D1, D2] have a similar chemical potential with a central Mott insulating region. One strongly doped dataset [D3] with a much lower total number of particles was taken to cover a broader doping regime in the analysis. To investigate the temperature dependence of correlations, dataset [D4] was taken for a system at 40 % higher temperature.

For all datasets, a 2d xy-lattice with spacings $a_x = a_y = a = 1.15 \,\mu$m was used. After the final evaporation and preparation of the quasi-2d atomic cloud, the lattice was ramped from $0\,E_R^{xy}$ to around $6.5\,E_R^{xy}$ within 100 ms. The final scattering length was set to $a_{\rm sc} = 810\,a_0$. The four datasets [D1, D2, D3, D4] comprise a total of [3224, 8667, 9440, 5588] realizations. The final x- and y-lattice depths for dataset D1 were $(6.9\,E_R^x, 6.9\,E_R^y)$. For datasets [D2, D3, D4] the xy-lattice spacings were slightly different $a_x/a_y = 1.02$ and therefore final lattice depths were chosen to be $(6.5\,E_R^x, 6.7\,E_R^y)$ to yield symmetric tunneling amplitudes $t_x = t_y = t$. The short spaced vertical lattice was $50\,E_R^s$ for [D1] and $44\,E_R^s$ for [D2, D3, D4]. We performed a Wannier function calculation to estimate the absolute tunneling amplitude for settings of datasets [D1] and [D2, D3, D4] to be $t/h = 240(10)$ Hz and $t/h = 260(10)$ Hz. The mean particle numbers of the four datasets are [89.8(1), 91.3(1), 52.0(1), 90.8(1)]. For D4, atoms were held in the harmonic trap for 1.75 s before loading the xy-lattice to produce systems at a higher temperature.

In a comparison of NN spin correlations at half filling to NLCE calculations of [209], the four datasets are consistent with temperatures T/t of [0.43(3), 0.52(5),
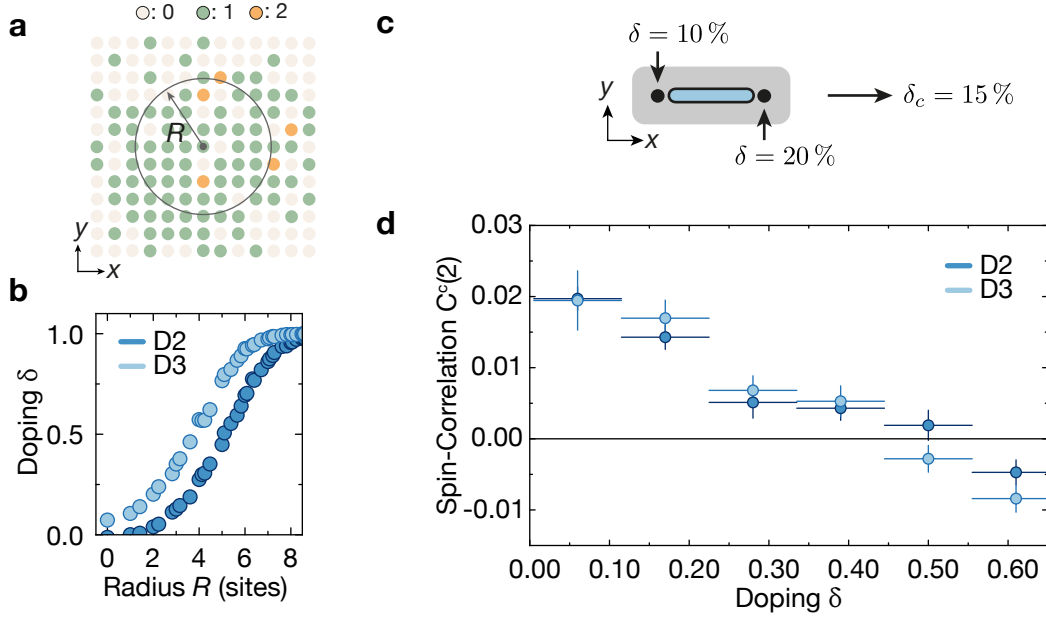
Figure 4.3: Doping control. a, Occupation of lattice sites in a single snapshot. The harmonic confinement of our atoms naturally leads to an increasing hole doping with increasing radial distance R from the center of the trap. **b**, Spatial doping distribution of two datasets with different total particle number. **c**, N-point correlators locally extend over N lattice sites. Here $N = 2$ is shown. A single doping value is assigned to each locally computed correlation value, according to the mean doping δ_c of all its sites. **d**, Extracted doping dependence of NNN spin correlations $d = 2$ from two datasets with different total particle number is shown. The error bar in doping corresponds to the bin size used for averaging local correlations.

$0.52(5), 0.77(7)]$. Interaction strengths U/t of the datasets are estimated to be $[8.9(4), 7.4(8), 7.4(8), 7.4(8)]$. Details of this parameter extraction can be found in appendix C.1.

The harmonic confinement of our atoms leads to an automatically increasing hole doping from the center to the edge of our systems, see Fig. 4.3. By averaging correlations in different areas Ω of the system, the doping dependence of a correlator can be mapped out. An example of the radially increasing hole doping is shown for datasets [D2, D3] in Fig. 4.3.

N-point correlators (in this work $N \in [2, 3, 4]$) locally extend over N lattice sites, of which not all share the same doping concentration, due to the spatial doping gradient in the system. When we compute the local value of a correlator (i.e. for N specific lattice sites), we label the calculated correlation value by the mean density of all its

contributing N sites $n = \sum n_i / N$ and therefore a doping $\delta = 1 - n$, see Fig. 4.3. We then average all local correlations with an assigned doping within a bin of width δ_w and centered around δ_c, such that $\delta \in [\delta_c - \delta_w/2, \delta_c + \delta_w/2]$. In the analysis, we display the averaged value at a doping δ_c with an error bar in doping of width δ_w.

We cross-check the validity of our method for extracting doping dependencies from our experimental system. To this end, we compare the doping dependence obtained for the same correlator between two datasets with very different total number of atoms, i.e. two datasets with a very different spatial doping distribution. In Fig. 4.3b we consider the correlation of spins at distance $d = 2$ apart from each other. A similar extracted quantitative and qualitative doping dependence is obtained from the slightly and more heavily doped dataset. Furthermore, the extracted doping dependence of other correlators presented in the following sections agrees between different datasets. This confirms the validity of our approach in our current parameter regime and for our experimental temperatures, where short-range correlations dominate. With more homogeneous systems obtained through potential shaping in the future, correlators occupying a larger spatial area or a more precise doping resolution will become accessible.

Error bars for all correlator-based observables were found by performing a bootstrap and computing the standard deviation of the mean across the resampled datasets.

4.2.2 Numerical calculations for comparison

There are three different questions, for which we provide answers by comparison to numerical calculations [236]. How much do our quantum simulation results have in common with exact computation at the largest accessible system size on a classical computer? How do popular approximate concepts for the weak-doping regime compare to the experiment at different dopings? Finally, we would like to identify the doping regime at which the system is described by a Fermi liquid.

All numerical calculations are at finite temperature $k_B T = 0.4\,t$ and were performed by A. Bohrdt, Y. Wang, F. Grusdt, and E. Demler. The calculations can be divided into three different categories, as shown in Fig. 4.4. Details of calculations can be found in [236]. The most important aspects are summarized below.

Exact diagonalization of Fermi-Hubbard systems with 4×4 sites was performed. Many observables in such a small cluster suffer from strong finite-size effects. Reasonable agreements with experiment are found for spin-charge correlators in the next section. These calculations furthermore provide important insights on aspects of Hubbard physics, such as the impact of doublon-hole fluctuations.
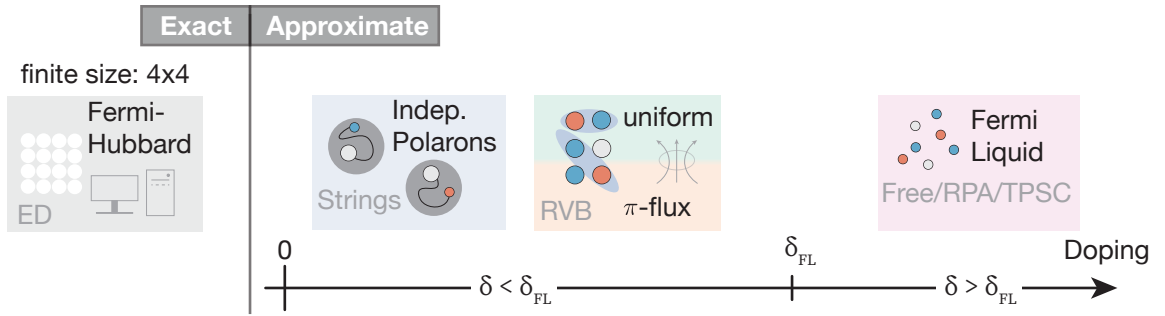
Figure 4.4: Comparison to theory. Experimental correlations are compared to numerical calculations of different theoretical concepts, which can be divided into three different categories. Exact diagonalization of finite size 4×4 Fermi-Hubbard systems, approximate concepts for weakly-doped Mott insulators and finally Fermi liquid related concepts for strong doping. For a detailed description of the concepts see text.

Correlations for three different weak-doping concepts were calculated at finite temperature, see Fig. 4.4: two versions of RVB states, namely uniform and π-flux (c.f. chapter 1), as well as the string model for independent magnetic polarons. Observables for these frameworks are computed from sampled real-space snapshots with the same algorithm as for experimental data.

Many other simplifying concepts for the weak and intermediate doping regime exist, see chapter 1 and [123, 124]. Our work provides a benchmark for some of the most common approaches. In the next section, we find limited overall agreement of the experiment with all three approximate models in particular in the crossover regime between polarons and Fermi liquid. The string model catches qualitative trends close to the Mott insulator.

To identify the Fermi-liquid regime, we are looking for agreement with mean-field inspired methods. In the simplest approach, we compare correlations of non-interacting (free) fermions, which we obtain by sampling real-space snapshots from a Fermi sea and computing observables with the same algorithm as for experimental data. When comparing spin susceptibility or structure factors, the random-phase-approximation (RPA) [237] provides a straightforward formalism to take small finite interactions into account on a mean-field level. Within the RPA, interactions lead to a renormalization, which diverges in the strong-coupling limit (e.g. at $U/t = 8$) already at low densities. A more advanced method is the two-particle-self-consistent (TPSC) approach [238, 239], which goes beyond classical mean-field theory because it assumes different renormalizations for the spin and charge degree of freedom. TPSC calculations describe the experimental spin susceptibility very well for dopings $\delta >$

δ_{FL} and quantitatively capture the incommensurate fluctuations at high dopings.

4.3 Evolution of correlations with doping

4.3.1 Spin-spin correlations - oscillatory behavior

We start by investigating how two-point spin correlations $C^c(\boldsymbol{d})$ evolve in a Mott insulator as a function of increasing hole doping. As shown in Fig. 4.5a, doping quickly reduces the amplitude of antiferromagnetic correlations, as expected from magnetic-polaron formation of mobile dopants. Furthermore, correlations weakly oscillate as a function of doping. Spin correlations at different distances (such as $d = \sqrt{2}, 2, \sqrt{5}, \sqrt{8}$) undergo a sign reversal at dopings $\delta = 20\text{-}40\,\%$.

The uniform-RVB state features similar sign flips of correlations and compares well also for larger dopings. π-flux and the string model behave similarly and show agreement with our data for $\delta < 20\,\%$, in line with observations of [72]. Predictions of different weak-doping concepts for two-point correlations are very similar. This calls for a comparison of higher-order spin-charge correlations, in order to find out which concepts are favored.

Two-point spin correlations of ED calculations show strong finite-size effects, which is why we do not compare them to experimental data at this point.

4.3.2 Spin structure factor - incommensurate fluctuations

Microscopic two-point correlations are related to different macroscopic quantities of the system. As mentioned in Chapter 1, the static spin structure factor $S(\boldsymbol{q})$ can be computed by taking the Fourier transform

$$S(\boldsymbol{q}) = \sum_{d=0}^{d=d_c} C^c(\boldsymbol{d})e^{i\boldsymbol{q}\boldsymbol{d}}/\eta \; . \tag{4.7}$$

Here, we introduced a cutoff distance d_c. For our temperatures, the spin correlation length is short enough to approximate the thermodynamic limit (infinitely large system) of the structure factor with short distance correlations $d \leq d_c$. At a selected doping concentration, correlations with a maximal distance $d_c = \sqrt{10}$ are taken into account. If all neglected distances $d > \sqrt{10}$ have vanishing correlation values, this structure factor estimates the thermodynamic limit. Since the correlation $C^c(\boldsymbol{d})$ falls off with increasing distance d at our temperatures, the contribution of distances $d > \sqrt{10}$ to the structure factor is indeed negligible compared to the much stronger shorter distances (at half filling $C^c(d = \sqrt{13}) = -0.005(3)$). For colder systems with long-range
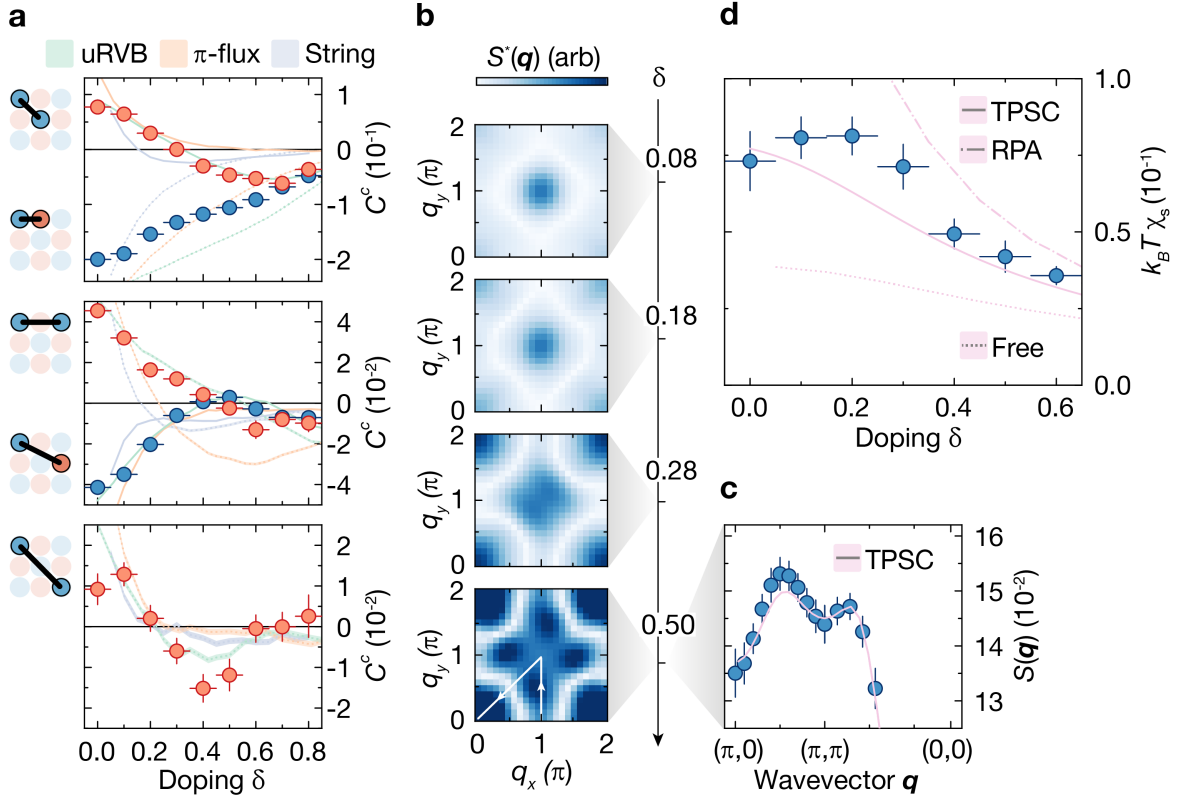
Figure 4.5: Magnetism from Mott insulator to Fermi liquid. a, Connected spin-spin correlations as a function of doping for different spin distances (see insets). Error bars denote one standard error of the mean (s.e.m) and for doping the bin width for averaging. Solid (dotted) lines of numerical calculations indicated in the legend correspond to spin distances of red (blue) data points. Shaded bands indicate the statistical s.e.m. for all calculations where visible. **b**, Offset adjusted static spin-structure factor $S^\star(q)$ for increasing doping with arbitrary scales and **c**, trace through unadjusted spin-structure factor $S(q)$ at 50 % doping. The full width of doping bins for **b**, **c** is 0.14. Solid pink represents a mean-field related TPSC calculation. **d**, Doping dependence of the uniform magnetic susceptibility. Solid, dashed and dotted pink curves correspond to TPSC, RPA and free fermion calculations (see legend). This figure is based on dataset D1 with 3 224 experimental realizations at $T = 0.43(3)\,t$ and $U/t = 8.9(5)$.

correlations this cutoff loses its validity. We keep a high number of points in momentum space, by padding distances up to $d = 14$ with a correlation value of zero, which does not add nor affect any information encoded in our Fourier observables.

In addition to $S(q)$, we compute a version of the structure factor for which a con-

stant and broad offset in momentum space is removed. To this end, we exclude the strong positive on-site term $d = 0$ from the Fourier transform and calculate

$$S^{\star}(\boldsymbol{q}) = \sum_{d=1}^{d=d_c} C^c(\boldsymbol{d})e^{i\boldsymbol{q}\boldsymbol{d}} \ , \tag{4.8}$$

which furthermore differs from $S(\boldsymbol{q})$ by the doping-dependent normalization $\eta = \eta_{\text{Pearson}}$ used throughout this chapter.

Oscillating magnetism, as observed with spin-spin correlations above, manifests itself as visible peaks in $S(\boldsymbol{q})$, which shift from the antiferromagnetic wavevector (π, π) towards $(\pi, 0)$ when the hole concentration reaches 50 %. In Fig. 4.5b, the evolution of $S^{\star}(\boldsymbol{q})$ is shown for different dopings (the evolution of $S(\boldsymbol{q})$ is shown in appendix C.2). The shift of $S(\boldsymbol{q})$ towards wavevectors incommensurate with the lattice spacing in Fig. 4.5c is in excellent agreement with our TPSC calculations. We consider such incommensurate spin fluctuations at large dopings a Fermi-liquid phenomenon, which furthermore confirms Quantum-Monte-Carlo (QMC) calculations of [240, 241]. We interpret this shift of peaks in the structure factor as a stretch of the Fermi wavevector $\boldsymbol{q}_{\text{F}}$ at large doping, which causes such incommensurate fluctuations through interactions on a mean-field level. A possible connection to incommensurate spin-density wave phases (stripes) at weak doping and colder temperatures [242] needs further exploration.

The density structure factor does not feature such incommensurate fluctuations in the experimental data, see appendix C.2.

4.3.3 Spin susceptibility - anomalous hump

In Fig. 4.5d, we extract the doping dependence of the uniform spin susceptibility χ_{s} from the structure factor via the fluctuation-dissipation relation $\chi_{\text{s}}(\boldsymbol{q} = \boldsymbol{0})T = S(\boldsymbol{0})$ [9]. This relation holds in this form only for $\boldsymbol{q} = \boldsymbol{0}$ and is a versatile tool, as mentioned in earlier chapters. In the context of density correlations the relation was used in [62–64]. The doping dependence is computed from dataset D1, which means all different dopings are at the same temperature T as the system is in thermal equilibrium.

The experimental susceptibility in Fig. 4.5d initially indicates a hump with increasing doping, i.e. it is not decreasing, but appears to be increasing. For stronger dopings $\delta > 30$ % the susceptibility continuously drops with increasing doping. We compare this behavior to the three different Fermi-liquid type calculations (free, RPA, TPSC). For free fermions, χ_{s} monotonously drops with doping. To avoid divergences of the RPA calculation, the calculation is performed at a lower effective interaction of $U/t = 4$. For strong dopings $\delta > 50$ % RPA starts to overlap with experimental data. The best agreement is found with our TPSC calculation, which quantitatively matches

for most dopings except the crossover region around $\delta \sim 20\,\%$.

All three mean-field inspired approaches predict a monotonously decreasing susceptibility with doping. Our measurements suggest the susceptibility increases at first before dropping after $\delta \sim 20\,\%$. Such a hump in the susceptibility is reminiscent of the pseudogap phenomenon and not captured by our FL calculations. This anomalous behavior is furthermore supported by QMC results [116] and indicates that the metallic regime below δ_{FL} is of different nature than the conventional Fermi liquid found at higher dopings.

4.3.4   Hole-spin-spin correlations - polaron breakdown

The previous section on two-point spin correlations found signatures of Fermi liquid behavior developing at dopings $\delta_{\mathrm{FL}} \sim 30\,\%$. Now we investigate what happens to the magnetic dressing of dopants. To this end, we track how connected hole-spin-spin correlations $C_\circ^c(\boldsymbol{r}, \boldsymbol{d})$ evolve with increasing doping, as shown in Fig. 4.6.

Weak doping

At weak doping of $10\,\%$, a hole perturbs all bonds in its vicinity with a sign opposite to the antiferromagnetic background. This means, NN spins ($d = 1$) align more ferromagnetically (parallel) and diagonal spins ($d = \sqrt{2}$) more antiferromagnetically (anti-parallel) directly next to the hole, see Fig. 4.6a. Such behavior could already be observed with individual doublon dopants in chapter 3. The effect of a magnetic polaron is to induce correlations, which oppose the antiferromagnetic background. The strength of this polaronic effect can be measured versus bond distance r from the hole. As shown in Fig. 4.6b, the radial dependence reconfirms a polaron size of two sites in diameter.

Strong doping

In the Fermi-liquid regime at large doping $\delta = 50\,\%$, the Pauli exclusion principle is the most important mechanism at play, which prevents fermions with the same spin to occupy sites in a small area [64]. This causes an enhanced antiferromagnetic correlation of all bonds in the vicinity of a hole, see Fig. 4.6. Intuitively, one can think of the hole as reducing the area available for two particles and therefore increasing the effect of the Pauli exclusion principle. A striking difference to the magnetic polaron regime is that the connected correlation of a hole with spin bonds does not oppose the background correlations. For instance, at strong doping, two-point NN correlations are negative and NN bonds also show a negative connected correlation with a single hole.
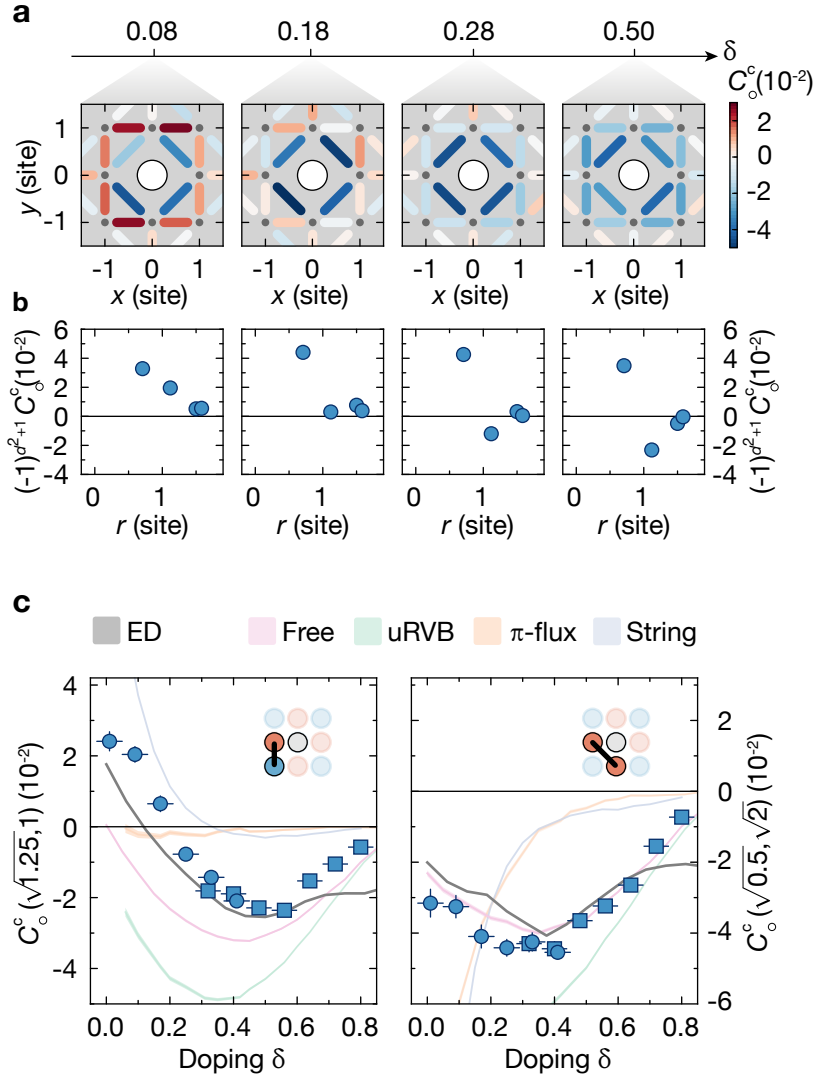
Figure 4.6: Connected hole-spin-spin correlations. a, Connected correlation (represented as bonds) of NN and diagonal bonds in the presence of a single hole (white central dot) for different dopings. **b**, Connected correlations as a function of bond distance r from the hole, where the sign of correlations with bond length $d = \sqrt{2}$ is flipped. Thus a positive correlation indicates a connected signal opposing the two-point correlations at half filling. Error bars denote one s.e.m. and are smaller than the point size. The full width of doping bins for **a**, **b** is 0.1. **c**, Doping dependence of NN and diagonal bonds closest to the hole (see insets). Square (circular) datapoints were extracted from a dataset D2 (D3) with 52.0(1) (91.3(1)) average number of particles. Solid lines represent numerical calculations (see legend) and shaded bands indicate (where visible) their statistical s.e.m. This figure is based on 18 107 experimental realizations at $T = 0.52(5)\,t$ and $U/t = 7.4(8)$.

Polaron breakdown

To monitor the transformation from a metal of magnetic polarons to a Fermi liquid, a useful indicator is to determine the doping at which connected hole-spin-spin correlations stop to oppose the background spin-spin correlations. This specific doping represents a turning point and we interpret this qualitative change as the breakdown of the polaron picture. In Fig. 4.6c, the evolution of closest distance NN and diagonal bonds is shown. The connected correlation of NN bonds continuously evolves from ferromagnetic (positive) to antiferromagnetic (negative) with increasing doping. Since two-point NN correlations remain negative for all dopings (Fig. 4.5a), the point at which these three-point correlations switch from ferromagnetic to antiferromagnetic signals the breakdown of the polaron picture. In our measurements, this takes place at dopings around 20 %. At a similar doping $\delta \sim$ 30 %, connected diagonal correlations are maximally antiferromagnetic.

Comparison to numerics

Correlations obtained with ED compare well with experimental data. The quantitative agreement is surprising at first because two-point spin correlations in ED have strong finite-size offsets. But these spin-charge correlations seem to avoid some of those offsets through the connected composition of these correlations.

Weak-doping concepts (string, RVB) make very different predictions for $C_\circ^c$. Only the polaron model (string) reproduces the experimental ferromagnetic alignment of the closest NN bond close to half filling, while RVB states show strong discrepancies to experiment. Uniform RVB is a prime example of how a theoretical approach can show excellent agreement with experiment in two-point correlations at low doping (Fig. 4.5a), but reveal strong deviations at higher-order correlators. For $\delta > 50$ %, uniform RVB and free fermions are very similar and capture experimental correlations, which in this regime are therefore mainly driven by fermionic statistics.

QMC studies of Fermi-Hubbard systems found the bandwidth of quasiparticle excitations evolves from polaronic ($W \sim 2J$, where J is the superexchange) to Fermi liquid ($W \sim 8t$) at around 30 % doping [117]. Our measurements suggest polaronic dressing persists up to $\delta \sim$ 20 % and smoothly dissolves into Fermi-liquid correlations around $\delta_{FL} \sim$ 30 %.

Effects from doublon-hole fluctuations

Doublon-hole fluctuations contribute a significant amount of holes close to half filling at our interaction parameter $U/t \sim 8$. The connected correlation signal coming
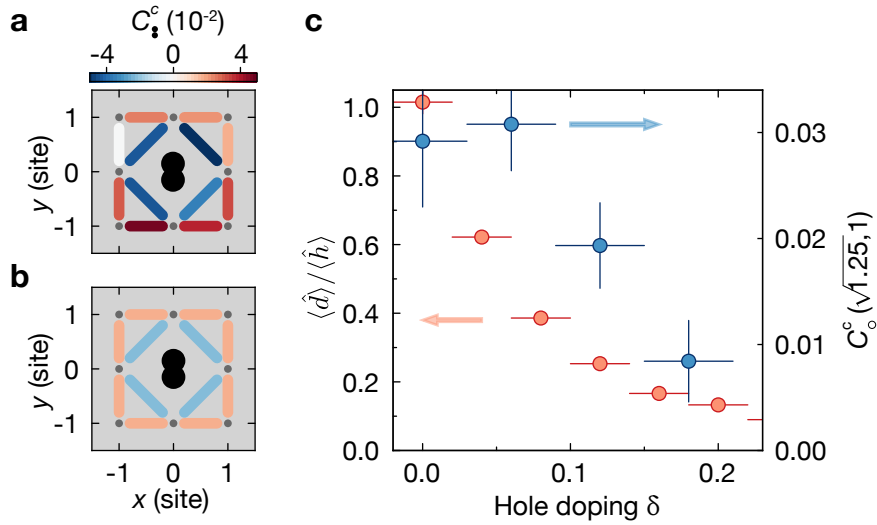
Figure 4.7: Doublon-hole fluctuations and connected three-point correlations. a.
Experimental connected doublon-spin-spin correlations at density $n \in [0.9, 1.0]$. All
doublons are therefore part of a doublon-hole fluctuation. **b**, ED calculation of con-
nected doublon-spin-spin correlations at half filling. **c**, Ratio between doublons and
holes (red, scale as indicated by red arrow) as a function of doping. At half filling,
there are as many holes as doublons. Connected correlation of the closest distance
NN bond next to a hole (blue, scale as indicated by blue arrow) as a function of
doping.

from such holes, therefore, mixes with the ones from doped holes at weak dopings[1].
By analyzing connected doublon-spin-spin correlations $C_{\bullet}^c$ at half filling in experi-
ment and ED, we find such false dopants have an effect qualitatively similar to real
dopants. As shown in Fig. 4.7a,b, correlations in the vicinity of a doublon fluctua-
tion are weakened. This is expected because the doublon has a hole bound to it in its
immediate vicinity. This hole weakens the average correlations around the doublon.
The ratio of doublon-hole fluctuations to the total number of holes rapidly drops with
increasing doping. Fig. 4.7c shows the ferromagnetic connected correlation of NN
bonds with holes decreases much slower than the amount of doublon-hole fluctua-
tions. This reconfirms that the measured correlations $C_{\circ}^c(\boldsymbol{r}, \boldsymbol{d})$ are dominated by actual
hole dopants.

---

[1]Note: In the previous chapter this issue was avoided because the interaction was stronger $U/t =$
14, the number of fluctuations, therefore, smaller, and doublons with holes as nearest-neighbor were
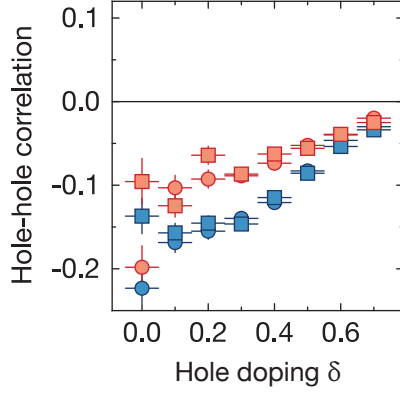discarded in the analysis.

Figure 4.8: Hole-hole correlations. Doping dependence of $g^{(2)}$ correlations between nearest-neighbor holes. Circular (square) data points correspond to $\boldsymbol{d} = (0,1)$ ($\boldsymbol{d} = (1,0)$). Blue (red) points were extracted from dataset D2 (D4) at temperature $0.52(5)\,t$ $(0.77(7)\,t)$.

4.3.5 Two-hole effects - peak at the crossover

The previous section revealed that polaronic effects of doped holes dissolve around 20 % doping and a Fermi liquid forms around 30 % doping. In this section, we search for two-hole effects and their role in the crossover region. When two polarons come close, their dressing clouds overlap, which can lead to the breakdown of polarons or induce effective interactions between them. This is often considered as a possible mechanism for pseudogap behavior [10, 13, 110].

Hole-hole

The simplest observable to detect mutual hole interactions is a two-point hole-hole correlator

$$g_{hh}^{(2)} = \langle \hat{h}_{\boldsymbol{r}_i} \hat{h}_{\boldsymbol{r}_j} \rangle / \langle \hat{h}_{\boldsymbol{r}_i} \rangle \langle \hat{h}_{\boldsymbol{r}_j} \rangle - 1 \ . \tag{4.9}$$

A negative correlation signals hole-hole repulsion, while a positive correlation indicates attraction. Already relative changes of such correlations as a function of temperature could give indications of possible interactions. At current temperatures of cold-atom quantum simulators dopants are negatively correlated (repulsion) at short distances and uncorrelated otherwise, see chapter 3 and [72]. In Fig. 4.8, the correlation of nearest-neighbor holes is tracked as a function of increasing doping and for two different temperatures. A negative signal persists throughout both doping regimes and at our parameters colder temperatures lead to stronger negative correlation.

Hole-hole-spin-spin

Even though mutual hole attraction is not resolved in our experiments, full resolution allows us to study how the spin environment reacts if two holes come close to each other. To perform such an analysis, we post-select on two holes at positions $\boldsymbol{r}_3, \boldsymbol{r}_4$

and measure the correlation between two spins in their vicinity, i.e. we evaluate the connected correlator $C_{\circ\circ}^c(l, r, d)$ introduced at the beginning of this chapter (Fig. 4.2). We focus on the case of NN ($l = 1$) and diagonal ($l = \sqrt{2}$) pairs of holes and consider bond lengths $d = 1, \sqrt{2}$.

To achieve a sufficient signal-to-noise ratio in the experiment, we combine the two pair configurations for NN ($l = (1, 0), (0, 1)$) and diagonal pairs ($l = (1, 1), (1, -1)$) by averaging all bonds with identical bond distance r from holes at fixed l. To spatially visualize the result, we plot these averaged correlations around the (arbitrarily) chosen configuration $l = (1, 0)$ for NN holes and $l = (1, 1)$ for diagonal holes, see Fig. 4.9a. As a result of the symmetric averaging, bonds with identical distance r in the figure share the same strength by definition.

A connected antiferromagnetic correlation exists at closest distance to NN as well as diagonal pairs, see Fig. 4.9a,b. This negative correlation persists in and connects both metallic regimes, albeit a different doping dependence for the two different hole distances is found.

For NN holes ($l = 1$), the closest distance ($r = 1$) NN bond ($d = 1$) starts with a negative correlation already at half filling and slowly fades to zero with increasing doping. At strong doping $\delta > 30\%$, the correlation starts to quantitatively agree with the correlation in a Fermi-liquid (free fermions). At half filling, a negative correlation originates from doublon-hole fluctuations, as described in a later paragraph below. Upon increasing the temperature from $T = 0.52(5)\,t$ to $T = 0.77(7)\,t$, the negative correlation of this bond is only weakly affected.

For diagonal holes ($l = \sqrt{2}$), the closest distance ($r = 0$) diagonal bond ($d = \sqrt{2}$) starts with a very weak correlation at half filling. With increasing doping, a negative correlation builds up, develops a peak in the crossover region, and then fades to zero in the strong doping regime. Doublon-hole fluctuations contribute a positive signal close to half filling, as discussed in a paragraph below. The peak of correlations in the crossover regime is also found in ED calculations. Similar to the case of NN holes described above, Fermi-liquid (free fermion) correlations quantitatively agree with experimental data for $\delta > 30\%$. However, the negative correlation with diagonal holes is much more affected by an increase in temperature.

Approximate weak-doping concepts (string, RVB) predict antiferromagnetic correlations of closest distance bonds but show limited overall agreement to experimental data.

Let us recapitulate what such a negative connected correlation means in terms of the bare spin environment of two holes, c.f. Fig. 4.2. When two holes are detected on a diagonal $l = \sqrt{2}$ at weak doping, the bare correlation of the diagonal bond in between them will be strongly negative. This bare negative strength is the sum of
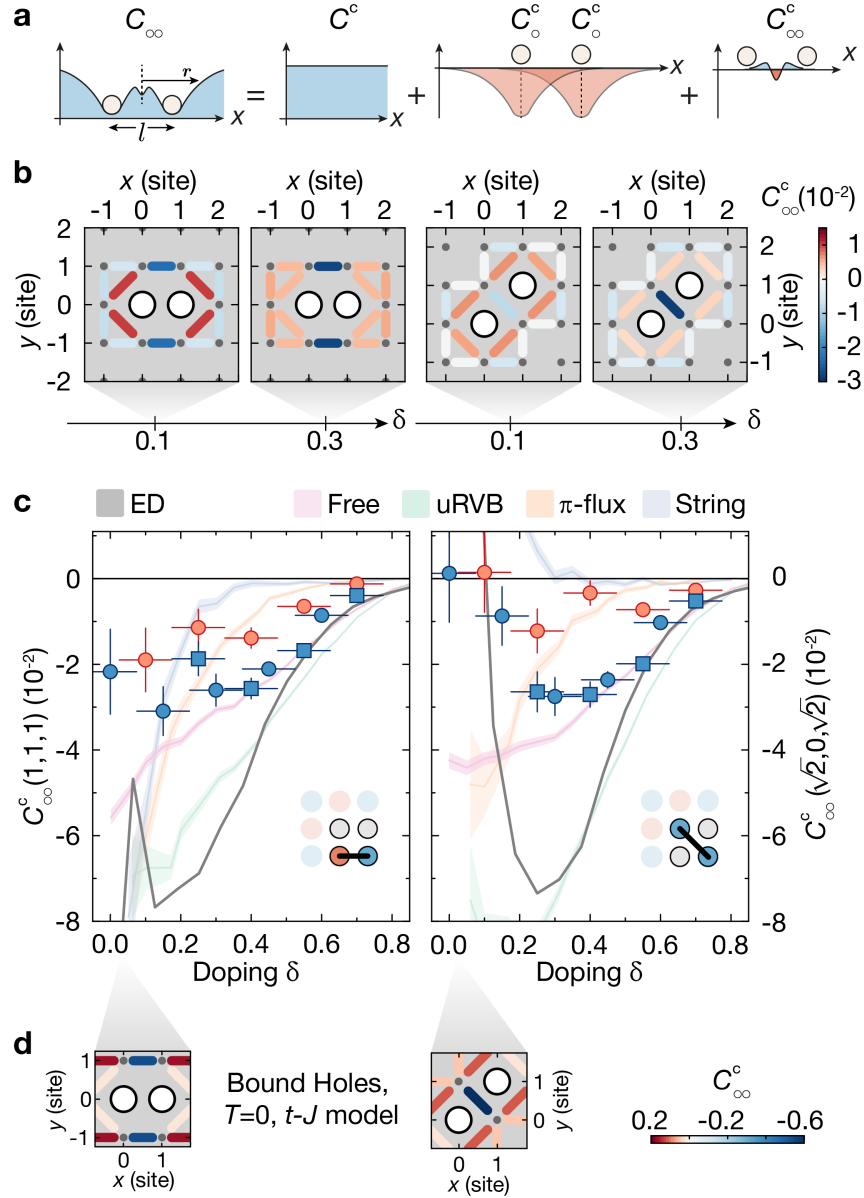
Figure 4.9: Connected hole-hole-spin-spin correlations. a, Decomposition of $C_{\circ\circ}$ into connected and disconnected part. **b**, Connected correlations of NN and diagonal bonds in the presence of two NN or diagonal holes. Two dopings are shown with a full width averaging bin of 0.2. Same bond distances and symmetric spatial hole orientations are averaged together (see text). **c**, Connected correlation of the bond with closest distance to the NN or diagonal hole pair (see insets) as a function of doping. Blue, red points correspond to experimental temperatures of $0.52(5)\,t$, $0.77(7)\,t$. Blue square, circular data points were extracted from datasets D3, D2 with on average $52.0(1)$, $91.3(1)$ particles. Solid lines are numerical calculations as indicated (see legend) and shaded bands their statistical standard error of the mean. **d**, DMRG calculations ($T = 0$) for two holes in the 6-leg ladder t-J model, where binding occurs. This figure is based on $23\,695$ experimental realizations at $U/t = 7.4(8)$.

a strong positive two-point spin correlation, a negative polaronic contribution from each hole separately, and finally the negative correlation with exactly two holes. All contributions together result in a strong negative correlation. Loosely speaking, the diagonal bond turns more negative in the presence of both holes, than it would need to from the average influence of two independent polarons.

To discuss a possible connection of the negative correlation to lower temperature physics, we consider two holes ($\delta \sim 2\,\%$) in the *t-J* model. In this model binding of polarons (holes) occurs at relatively high temperatures [112]. We performed density-matrix-renormalization-group (DMRG) calculations of this scenario at $T = 0$ for a 6-leg ladder and show the connected spin environment in Fig. 4.9c for $l = 1$ and $l = \sqrt{2}$. A striking effect of hole pairing is the emergence of a strong antiferromagnetic spin bond at closest distance to the pair [111, 112]. Our experimental correlations feature similar signatures, but there is no further indication of hole binding from hole-hole correlations. Therefore, we conclude that qualitative features of the zero temperature physics of two holes are already encoded in the finite temperature limit and a strong interplay of spin and charge correlations already precedes hole pairing or formation of other competing orders at colder temperatures.

Effects from doublon-hole fluctuations

Since holes belonging to doublon-hole fluctuations and doped holes are not distinguished in our analysis, such fluctuations contribute a significant part of the experimental signal at half filling. We can independently determine connected correlations arising from doublon-hole-fluctuation holes, by analyzing four-point correlations $C^c_{\bullet\bullet}$ around half filling with doublons, instead of holes. All doublons in this regime originate from quantum fluctuations. In Fig. 4.10, we show these connected correlations with experimental data and from ED at half filling.

Two aspects are relevant to our understanding of four-point correlations presented in Fig. 4.9. For NN doublons, a closest distance antiferromagnetic correlation is visible in the experiment and in ED. The connected correlation of the closest bond of diagonal doublon pairs is positive in ED and close to zero with experimental data. Residual doublon dopants in the experiment might contaminate the signal in Fig. 4.10b with a negative signal, which would lead to a cancellation of the positive signal from doublon fluctuations.

4.4 Conclusion

This chapter harnessed the unique capability of our quantum simulator to study how correlations between spins and charges evolve in a Mott insulator with increasing hole
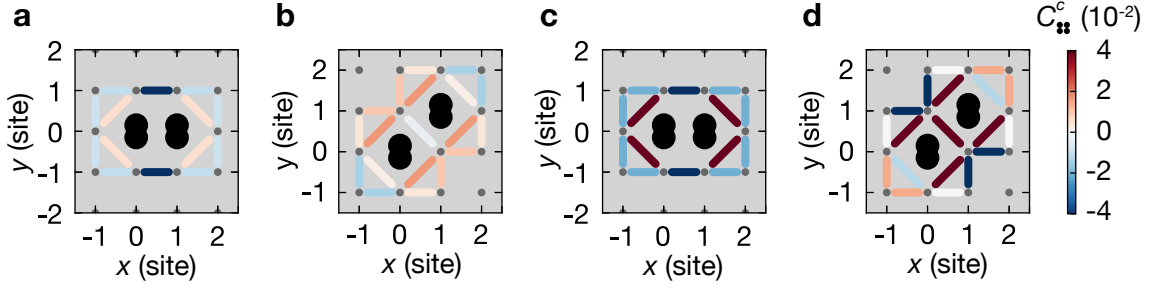
Figure 4.10: Doublon-hole fluctuations and connected four-point correlations. Experimental connected doublon-doublon-spin-spin correlations for **a**, NN doublons and **b**, diagonal doublons, averaged in a region with density $n \in [0.88, 1.02]$ at $U/t = 7.4(8)$. Doublons mainly originate from doublon-hole fluctuations. ED calculations of these correlations with doublons at exactly half filling are shown in **c** for NN doublons and **d** for diagonal ones.

doping at temperatures $T \sim 0.4\,t$. The fully spin- and density-resolved snapshots of doped systems gave access to spin-charge correlations up to fourth order, which are unavailable in traditional solid-state experiments. More conventional observables, such a spin susceptibility and structure factor were computed from two-point correlations in the system.

We confirmed two distinct metallic regimes, which are connected in a crossover at doping around $\delta_{\text{FL}} \sim 30\,\%$. At weak doping, a metal with polaronic correlations was found, while at strong doping the system turns into a normal Fermi liquid. The transition between the two regimes manifests as a change in all studied system observables, of which the most important ones are summarized in table 4.1. How the observed doping δ_{FL} for the crossover in our experiment can be related to solid-state measurements is unclear, since details like band structure and the difference in accessed observables plays an important role.

In a benchmark of three effective weak-doping theories (string, π-flux, uniform RVB), we find limited overall agreement with our system. In particular the crossover regime ($\delta \approx 10\text{-}30\,\%$) calls for more efficient descriptions.

How the measured antiferromagnetic correlation next to pairs of holes is related to effective hole-hole interactions and how collective phenomena at colder temperatures connect to our reported correlations are to be investigated in future experiments. Only modest improvements in colder temperatures might be required for an experimental observation of pairing [112] or pseudogap behavior [209]. Cooling proposals are available [173], which can readily be tested with this setup.

Spin-charge correlators can also be studied in cold atom systems out-of-

Observable	Doping	Behavior
spin-spin	20-40 %	Various distances reverse sign
$S(\boldsymbol{q})$	50 %	Visible incommensurate fluctuations
χ_s	20-30 %	Slope changes
hole-spin-spin $(r = \sqrt{1.25}, d = 1)$	20 %	correlation reverses sign
hole-spin-spin $(r = \sqrt{0.5}, \sqrt{2})$	20-40 %	correlation maximally negative
hole-hole-spin-spin $(l = \sqrt{2}, r = 0, d = \sqrt{2})$	30 %	correlation maximally negative
hole-hole-spin-spin	> 30 %	agreement with free fermions (FL)

Table 4.1: Summary of key experimental results.

equilibrium [69, 70] and with slightly colder temperatures the portfolio of correlators could be extended to fifth-order [243]. Such measurements could continue to inspire our understanding of Fermi-Hubbard systems and their exotic many-body phenomena in the future.

Conclusion and outlook

This thesis reported on cold atom quantum simulation of doped antiferromagnetic Mott insulators at temperatures around the superexchange energy. The full microscopic information on the location and spin of every particle proved to be a powerful asset of quantum gas microscopy. We harnessed the full potential of our spin- and density-resolved machine to reveal the magnetic dressing cloud of single dopants in the Mott insulating regime. This marked a first real-space observation of a magnetic polaron. Furthermore, we could show how magnetic polarons dissolve at stronger doping and found the formation of a Fermi liquid around 30 % doping. In the magnetic environment of pairs of dopants, we found an antiferromagnetic correlation, which peaked at the crossover between the two metallic regimes. The Fermi liquid itself exhibits incommensurate magnetic fluctuations, whose connection to spin-density waves at lower doping and colder temperatures requires further exploration. The spin-charge correlators evaluated within this work uncovered several deficiencies of popular approximate weak-doping concepts close to the crossover between both metals. Measurements within this thesis represent a valuable benchmark for future effective theories of anomalous metallic phases in the context of high-T_c materials.

Optical superlattices were a key technology in this thesis for the manipulation and detection of cold atomic systems. We described the engineering and design of highly-stable bichromatic superlattices, of which an implementation for the vertical direction was built into the apparatus. This enabled robust charge pumping of layered systems. Two applications demonstrated the capabilities of the underlying superlattice design. High-fidelity microscopy of bilayer systems was realized, which paves the way towards quantum simulation of layered materials. For monolayer systems, bilayer microscopy allowed full spin and density resolution of more than two times larger systems than before and access to higher energy scales.

The greatest challenge for cold-atom based quantum simulation of 2d Fermi-Hubbard systems is the quest for lower temperatures. Considering the ultimate reward, i.e. the solution of one of the most paradigmatic models for strongly-correlated electrons, every try seems worth the effort. In this respect, current experiments have built up a dramatic suspense. The coldest temperatures of $T = 0.25\,t$ [61] realize long-range antiferromagnetic correlations and quantum gas microscopes have already shed new light on doped 2d Mott insulators in various ways [59, 60, 70, 72, 231, 236]. These and other experimental setups are on the verge of probing pseudogap and strange metal regimes. Not even a factor of two in lower temperatures might be required to detect hallmark features of such exotic states [116–118]. One order of magnitude lower temperatures could unleash the full power of cold-atom quantum simulators to explore the regime of collective phenomena [119, 120]. Given these scenarios, there will be

a strong impact of experiments per achieved temperature reduction in the years to come.

Most excitingly, there are possible ways to lower the temperature in our existing experimental setup. Most of these ideas revolve around the manipulation of atoms with highly-stable superlattices. Two-component band insulators can be prepared at ultra-low entropy, as demonstrated by [165]. The vertical superlattice could be used to prepare such states with even lower effective temperature, by a much more efficient entropy redistribution [173]. Next, a superlattice within the plane could be used to adiabatically connect such a low-entropy band insulator to a low-entropy Mott insulator [172].

A new generation of bichromatic superlattices for the xy-direction is currently under construction. This will not only enable the aforementioned cooling schemes but also allow for the realization of more exotic Hamiltonians, such as plaquettes and mixed dimensional systems [244]. During the writing of this thesis, a digital-micromirror device has been implemented into the setup. By now, tailored site-resolved optical potentials can be used to engineer Fermi-Hubbard systems with increased potential homogeneity and at almost arbitrary geometry.

I am certain, the future of this experimental setup is bright and many more surprises and great discoveries are yet to come. The entire field of fermionic quantum gas microscopy has delivered an amazing sprint of fantastic results over the last decade. Many groups continue to push the limits of this technique. If the pace continues, I am exhilarated to see how the community will transform our understanding of strongly-correlated systems in the upcoming years.

A

Supplementary information for chapter 2

A.1 Derivations

System size $N^\star$

Here we derive Eq. 2.3, which measures the 2d system size $N^\star_{9,40}$ of a Mott insulator at $U/t = 8$ in a square lattice at $9\,E_R$, given the condition that at maximum laser power per beam P the lattice has a depth of $40\,E_R$. We start by restating the definition

$$N^\star = \frac{\pi 16 t}{m\omega^2 a^2} = \frac{\pi 16 \cdot 8}{h^2} \frac{t \cdot E_R}{\omega^2} \quad , \tag{A.1}$$

where t is the nearest-neighbor tunneling amplitude, m the atomic mass, ω the radial harmonic confinement and a the lattice spacing. Along with the asymptotic analytic expression for the tunneling Eq. 1.8 and the definition of the recoil energy Eq. 1.7 we are going to use the following expressions (see also [176]) for the radial harmonic confinement in red-detuned optical lattices ω, the lattice depth V and single-beam peak intensity I

$$\omega = \frac{1}{\hbar} \frac{2}{\pi} \frac{a}{w} E_R \sqrt{2V/E_R} \tag{A.2}$$

$$V = \frac{1}{2\epsilon_0 c} \alpha 4 I \tag{A.3}$$

$$I = \frac{2}{\pi} \frac{P}{w^2} \quad , \tag{A.4}$$

where w is the gaussian beam waist, α the real part of the complex polarizability $\tilde{\alpha}$ and P the laser power per beam. The expression for the harmonic confinement ω caused by red-detuned optical lattices was derived for a gaussian envelope $I \propto \exp(-2r^2/w^2)$. Note the factor of 4 in the conversion from single-beam intensity to

lattice depth V. The constructive interference of two beams leads to this enhancement in depth.

We start by finding the gaussian beam waist, which leads to a $V = 40\,E_R$ deep lattice at full power P

$$w^2 = \frac{\alpha}{2\epsilon_0 c}\frac{8}{40\pi}\frac{P}{E_R} \quad . \tag{A.5}$$

Now we can use this information to compute the radial harmonic confinement caused by the lattice at a depth of $V = 9\,E_R$. We neglect the contribution to ω from the vertical lattice. Furthermore, we assume retro-reflected lattices. In this case, the x-lattice causes a harmonic trapping along the y-direction ω_y and the y-lattice a harmonic trapping along the x-direction ω_x. Since we assume both lattices have the same parameters, the radial harmonic confinement is given by $\omega = \omega_x = \omega_y$ and therefore

$$\omega^2 = \left(\frac{1}{\hbar}\frac{2}{\pi}\frac{a}{1}E_R\sqrt{2\cdot 9}\right)^2\left(\frac{40\pi}{8}\frac{2\epsilon_0 c}{\alpha}\frac{E_R}{P}\right) \quad , \tag{A.6}$$

which can be simplified to

$$\omega^2 = \frac{1}{\hbar^2}\frac{18\cdot 4\cdot 40}{8\cdot\pi}\frac{a^2 2\epsilon_0 c}{\alpha P}E_R^3 = \frac{1}{\hbar^2}\frac{360}{\pi}\frac{a^2 2\epsilon_0 c}{\alpha P}E_R^3 = 180\pi\frac{2\epsilon_0 c}{m\alpha P}E_R^2 \quad . \tag{A.7}$$

The tunneling amplitude in an optical lattice at $V = 9\,E_R$ is given by

$$t = \frac{4(9)^{3/4}e^{-6}}{\sqrt{\pi}}E_R \tag{A.8}$$

By plugging Eq. A.7 and A.8 into Eq. A.1, we therefore find

$$N^\star_{9,40} = \frac{\pi 16\cdot 8}{h^2}\frac{4(9)^{3/4}e^{-6}}{\sqrt{\pi}}\frac{m\alpha P}{180\pi 2\epsilon_0 c} = \frac{64(9)^{3/4}e^{-6}}{45\sqrt{\pi}h^2\epsilon_0 c}m\alpha P \quad , \tag{A.9}$$

which is the maximum system size at $V = 9\,E_R$ for a typical Mott insulator $U/t = 8$, when parameters are optimized, such that the lattice is exactly $40\,E_R$ deep at maximum laser power. This expression confirms Eq. 2.3 of the main text with a constant

$$b = \frac{128(9)^{3/4}e^{-6}}{45\sqrt{\pi}h^2\epsilon_0 c} \quad . \tag{A.10}$$

As mentioned, this scaling neglects the contribution from the vertical lattice. In the MPQ-machine, the vertical bichromatic superlattice was engineered with elliptical beam shaping to ensure a minimal contribution to the radial trapping from this

Temperature	Pressure	Humidity	$(n(1064\,\mathrm{nm})-1)10^6$	$(n(532\,\mathrm{nm})-1)10^6$
23°C	1 bar	50 %	262.563	266.629
24°C	1 bar	50 %	261.645	265.699
23°C	1.001 bar	50 %	262.826	266.897
23°C	1 bar	60 %	262.460	266.530

Table A.1: Refractive index n in air for 1064 nm and 532 nm under different conditions.

lattice. The derived equations assumed symmetric waists of the optical beams. Elliptical beam shaping for xy-lattices could be used to push system sizes even more, by focusing beams more tightly along the vertical z-direction to a waist w_z and increasing the beam size along the x- or y-direction to w_x, w_y. For retro-reflected square lattices with the settings described above and $w = \sqrt{w_x w_z}$, the system size scales linearly with the ellipticity $w_x/w_z = w_y/w_z$.

Scaling of Γ_{sc}

In the main text, we discussed how off-resonant scattering from the optical lattice scales with lattice spacing and polarizability at a fixed lattice depth of $V = 9\,E_{\mathrm{R}}$. We assumed a two-level system (c.f. Eq. 1.4) and red-detuned optical lattices, such that

$$\frac{\hbar\Gamma_{\mathrm{sc}}}{t} = \frac{\Gamma}{\Delta}\frac{V}{t} = \frac{9\sqrt{\pi}}{4(9)^{3/4}e^{-6}}\frac{\Gamma}{\Delta}. \tag{A.11}$$

This equation shows, the relative off-resonant scattering is independent of the choice of lattice spacing and scales only like $1/\Delta$. The bare scattering rate increases by $1/\Delta^2$.

A.2   Refractive index data

Fig. 2.9 of the main manuscript is based on refractive-index data, which was calculated from the Edlén equation [175] and is summarized in table A.1. The slopes of these refractive index changes are stated in Fig. 2.9 as an estimate for the sensitivity of φ_{r} to fluctuations around typical room conditions (23° C, 1 bar, 50 % humidity).

A.3   Phase-stability characterization

This section verifies the tunneling amplitude and coherence properties between the two layers of a bilayer system, which is realized with the vertical bichromatic superlattice.
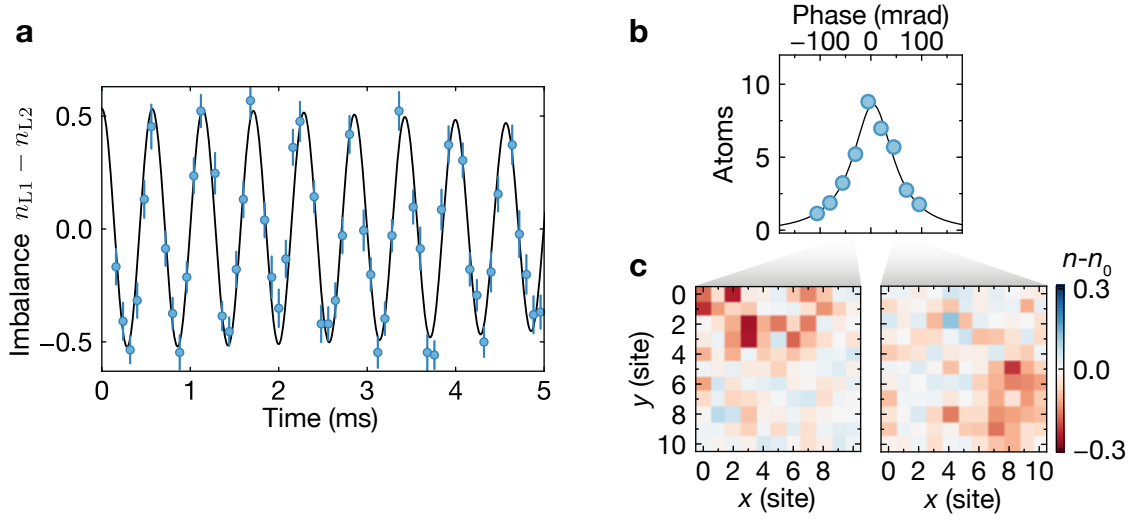
Figure A.1: Characterizing the superlattice. a, Imbalance of the average local densities of two layers ($n_{L1} - n_{L2}$) after quenching on inter-layer tunneling in a resonant double-well system. To avoid damping of the Rabi oscillation from a spatially varying double-well tilt, we average over a region of three sites located in the metallic wing of the cloud with an average density per site of 0.5. By fitting the observed Rabi frequency (solid black), we extract the inter-layer tunneling strength of $t_z/h = 876(1)$ Hz. **b**, Total number of atoms of a dilute cloud transferred in 2 ms to an adjacent layer at very weak coupling $t_z/h \sim 30$ Hz as a function of the superlattice phase. The width of phases is extracted by a lorentzian fit (solid black) and found to be $97(20)$ mrad FWHM, averaging over the entire system and 14 hours of measurement time. **c**, Change in density ($n - n_0$) of each site in the initial xy-lattice system for transfer at two different superlattice phases of **b** as indicated by the gray shadings.

To estimate the tunnel coupling t_z, we measured Rabi oscillations of atoms in the vertical double-well system. To this end, we prepared 2d Mott insulators in a very deep xy-lattice of $26\,E_R^{xy}$ in a single layer without vertical tunnel coupling $t_z = 0$. Then a strong tunneling amplitude to an adjacent layer was quenched on. In a separate scan of the superlattice phase, we confirmed the quench realizes resonant Rabi oscillations without a detuning between layer $\Delta = 0$. After a variable time duration, all tunnel couplings were non-adiabatically switched off and bilayer readout was applied to detect the occupation in both layers with single-site resolution. In Fig. A.1a, the oscillation of the average occupation of three sites in the metallic wing is shown for a quench to $V_s = 11\,E_R^s$ and $V_l = 100\,E_R^l$. By fitting an exponentially decaying sinusoidal function to the imbalance between the average density in layer one (n_{L1})

and layer two (n_{L2}), we extract a tunneling amplitude of $t_z/h = 876(1)$ Hz for those lattice parameters. The error bar denotes the uncertainty of the fit.

To obtain precise values on the coherence properties of the bilayer system, i.e. on the phase stability of the superlattice, we performed a dedicated set of spectroscopy measurements. Similar to the setting for Rabi oscillations, initially a single layer without vertical coupling $t_z = 0$ was prepared. The 2d system in this case was a large and dilute cloud at xy-lattice depth of $26\,E_R^{xy}$. The vertical superlattice was set to $V_s = 25\,E_R^s$ and $V_l = 100\,E_R^l$ in a strongly-tilted double-well configuration. Then the double-well system was quenched rapidly into resonance at variable superlattice phase for a total duration of 2 or 6 ms. The amount of atoms transferred to the adjacent layer is measured as a function of the phase. Since the vertical tunneling amplitude for those parameters is $t_z/h \sim 30$ Hz, this sequence probes the limit of small population transfer between planes. The theoretical full-width-half-maximum (FWHM) width (in terms of φ_r) for a 6 ms duration is 2 mrad. From the experimentally determined linewidth (i.e. phase width) for atom transfer, phase stability down to 2 mrad can therefore be diagnosed in principle. As shown in Fig. A.1b for 2 ms transfer duration, a system of 121 sites exhibits a FWHM of 97(20) mrad. This width is currently limited by spatial inhomogeneities of the local double-well potential, caused by optical corrugations in the xy-lattice and residual misalignment of the superlattice. The superlattice phase for resonant transfer between the two layers depends on the spatial position in the xy-plane, see Fig. A.1c. When the atomic transfer is measured in a region of 9 lattice sites for a transfer duration of 6 ms, the curve of main text Fig. 2.11b is recovered, which has a FWHM of 25(7) mrad. This width, therefore, represents an upper bound for the relative phase stability, even though the actual stability might be better. Higher accuracy of such a phase stability measurement can be obtained in the future, by using xy-lattices without optical corrugations and with improved superlattice alignment.

A.4   Pump fidelity

Chapter 2 described charge pumping and bilayer readout for spin- and density-resolved microscopy of 2d systems. In order to show that no particle motion occurs during spin-splitting and pumping, we compared the 2d density and its fluctuations between the spin-resolved bilayer method and standard single-layer microscopy. For both detection methods, the same Mott insulating system at $V_x = 11\,E_R^{xy}$, $V_y = 12\,E_R^{xy}$ and interaction $U/t \sim 35$ was imaged. As shown in Fig. A.2, the density and its normalized fluctuations are in good agreement for the two methods. This furthermore demonstrates that spin splitting and charge pumping accurately preserve observables of the parent 2d system.
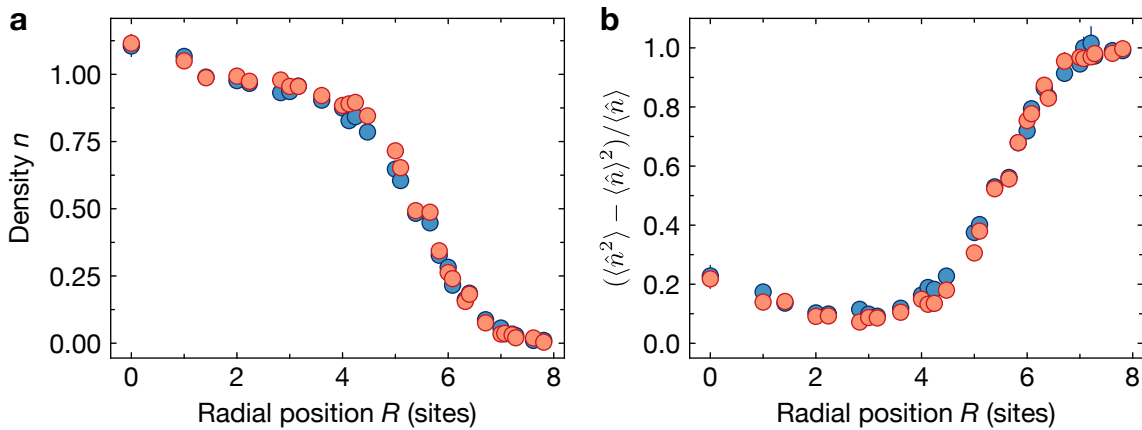
Figure A.2: Comparing pumped and un-pumped systems. Averaged radial **a**, density and **b**, fluctuation profiles of an identical Mott-insulating system, as measured without (red) and with (blue) our spin-resolved technique. Error bars, where visible, denote one s.e.m. and are smaller than the point size otherwise.

A.5   Bilayer reconstruction

Bilayer readout produces two single-site resolved images per experimental realization. These are images of two layers, which can belong to a bilayer system or represent spin information of a 2d system. To fully reconstruct the underlying state and its site-resolved occupations and/or spins, two steps are performed. As described in chapter 2, the first step consists of determining the single-site resolved occupations in each image separately. For this task, the standard monolayer reconstruction algorithm can be used, which uses a deconvolution with a point-spread function [159]. In a second step, the xy-lattice sites of both images need to be paired, i.e. the sites which were initially vertical nearest neighbors need to be identified. Typically, both images have a fixed position on the camera and the mapping of xy-lattice sites in one image to the sites of the other image is constant and needs to be found only once.

For measurements with bilayer readout of chapter 2 and dataset D1 of chapter 4, the microscope objective was physically moved by $21\,\mu$m between two consecutive images. The vertical movement caused small displacements of the objective in the transverse direction. This resulted in shot to shot fluctuations of the location (on the camera) of the two images on the order of up to one lattice site. An initial guess for the pairing of sites is provided, by matching the lattice site at the center of mass of each image. To ensure a correct pairing of sites between both images for the spin-resolution method, we compared 25 different pairing possibilities for each snapshot, which are given by shifting one layer in x and/or y direction by ± 2 lattice sites. Since
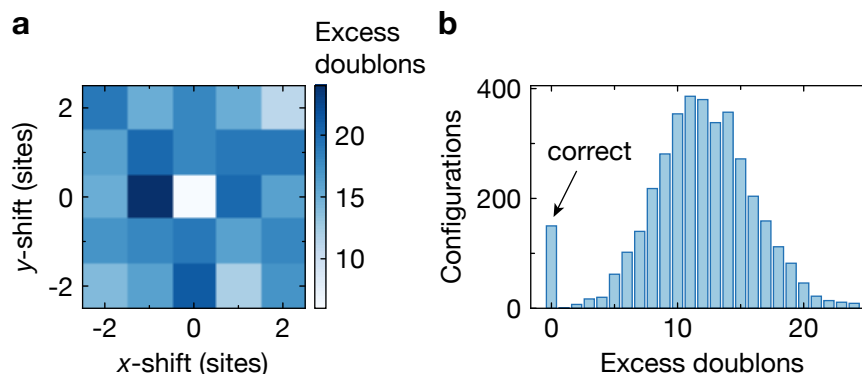
Figure A.3: Correct combination of two spin layers for 2d spin resolution. The correct pairing of xy-lattice sites of both spin layers can be diagnosed by the number of doublons resulting from a possible pairing configuration. **a**, Counting the number of resulting doublons, if the two spin layers are recombined with one layer shifted in x- or y-direction. The number of additional (excess) doublons is counted, as compared to the most likely configuration (centered at $x = y = 0$). For each snapshot, all 25 possible configurations for the reconstruction are considered. **b**, Histogram of the number of possible pairing configurations as a function of excess doublons in this setting for a dataset of 150 snapshots. The 150 most likely pairing possibilities are indeed unique compared to all other possibilities.

our 2d systems have large Mott-insulating regions with unit occupation, we found the right configuration was uniquely given by the lowest amount of reconstructed double occupations. The pairing configuration with the minimum number of doublons is referred to as the most likely configuration. As can be seen in Fig. A.3a, all 25 pairing configurations around the most likely configuration would lead to significantly more reconstructed doublons in a single experimental shot. The correct pairing therefore uniquely minimizes the total amount of reconstructed double occupations. This algorithm reliably reconstructs the spin and density of 2d systems with a large Mott insulating region also for larger datasets, as shown in Fig. A.3b for 150 shots. In only 12.7 % of shots, the initial guess (center-of-mass matching) actually differed from the final configuration.

Recently, the fluorescence imaging path has been rebuilt to avoid physical movements of the objective between two consecutive images. Now, the fluorescence light is split into two paths, which is imaged at different positions of the same camera. By adjusting a lens position in one of the arms, this path can be controlled to have a 21 μm displaced focus position. This way, two layers at two different foci can be imaged simultaneously, see Fig. A.4. The total exposure time for this bi-focus technique shortens by the time, which was previously required for the physical translation of
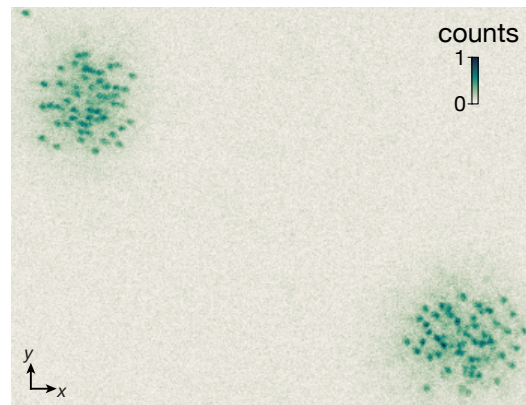
Figure A.4: Bi-focus microscopy in a single image. Spin-resolved snapshot of a Mott insulator. The fluorescence light is equally split into two paths. The focus of one path is 21 μm displaced compared to the other path. This is achieved, by adjusting the position of a lens in a telescope of the second path.

the objective (0.5-1s). The bi-focus method has no physically moving parts during imaging and therefore does not require a matching algorithm for every snapshot.

B |

Supplementary information for chapter 3

B.1 Doping calibration

We performed doping of our systems by controlling the total number of atoms in the harmonically confined lattice. For measurements with mobile doublons, we realized weak doublon doping in the center of the trap. Pinned doublons were created in an otherwise undoped system. To find the correct atom number for each setting, we measured the number of double occupations per number of atoms (doublon fraction) in our system as a function the average number of particles N, see Fig. B.1a. For low N, the doublon fraction saturates below 4 %, which we attribute to quantum fluctuations in the form of doublon-hole pairs. The background of doublon-hole fluctuations is confirmed by discarding doublons with holes as NNs, obtaining the curve of doped doublons versus N shown in Fig. B.1b. For low N, no doped doublons are present. However, at higher atom numbers $N \sim$ 60-70 finite doping sets in. The mean N for the mobile and pinned setting was 72 and 55.

B.2 Density correlations

The positive correlation of doublons with holes and the negative correlation of doublons with doublons at short distances was mentioned in the main text. Here we present those correlations in greater detail.

We computed the $g^{(2)}$-correlation function between doublons (doublon-density operator $\hat{d}_{r_1}$) at position r_1 and holes (hole-density operator $\hat{h}_{r_2}$) at position r_2 as a function of their mutual distance r in the dataset with mobile doublons

$$g_{dh}^{(2)}(r_1, r_2) = \frac{\langle \hat{d}_{r_1} \hat{h}_{r_2} \rangle}{\langle \hat{d}_{r_1} \rangle \langle \hat{h}_{r_2} \rangle} - 1 \quad . \tag{B.1}$$

Correlations at different r are shown in Fig. B.2a. Strong doublon-hole bunching at
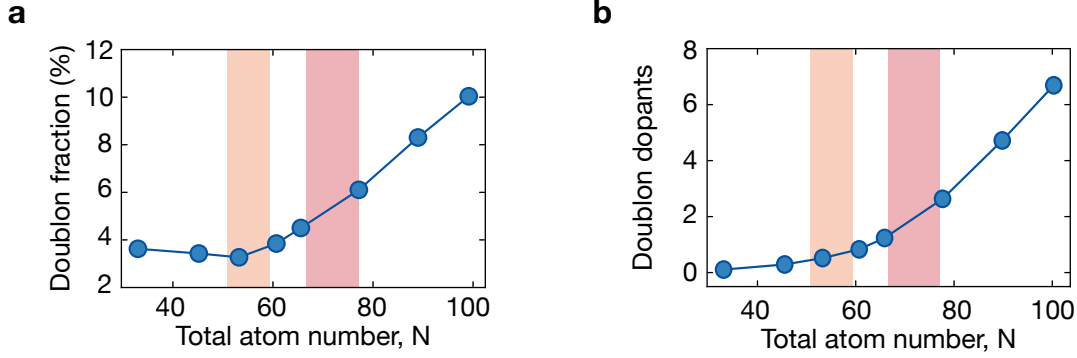
a

b

Figure B.1: Doping calibration. **a**, Fraction of double occupations and **b**, total number of double occupations in the system as a function of number of atoms in the system. The final number of particles was set by our evaporation parameters. Measurements for pinned doublons were taken in an undoped system (orange bar). For the mobile doublon, data was taken at weak doping (red bar). The width of the bars indicates the standard deviation around the mean atom number for the pinned and mobile dataset respectively.

NN distances exists, which originates from doublon-hole fluctuations. To distinguish these quantum fluctuations from doped doublons, we excluded doublons with holes as NNs from the analysis in the mobile setting.

In a similar analysis, we investigate correlations between doublons in the dataset with mobile doublons. The correlator

$$g_{dd}^{(2)}(\mathbf{r}_1, \mathbf{r}_2) = \frac{\langle \hat{d}_{\mathbf{r}_1} \hat{d}_{\mathbf{r}_2} \rangle}{\langle \hat{d}_{\mathbf{r}_1} \rangle \langle \hat{d}_{\mathbf{r}_2} \rangle} - 1 \tag{B.2}$$

is shown in Fig. B.2b for different doublon distances $\mathbf{r}$. Doublons are negatively correlated at NN distances and quickly become uncorrelated within our measurement precision. Such negative correlations are expected for free fermions. Therefore, we do not resolve any interactions between dopants at our temperatures and can treat doublons as independent dopants.

B.3   Data filtering

In a pre-processing step, some snapshots of the bare data were discarded. The monochromatic superlattice used for spin-resolved measurements in chapter 3 showed much stronger relative-phase fluctuations than the current bichromatic vertical implementation. To filter out fluctuations in the spin detection
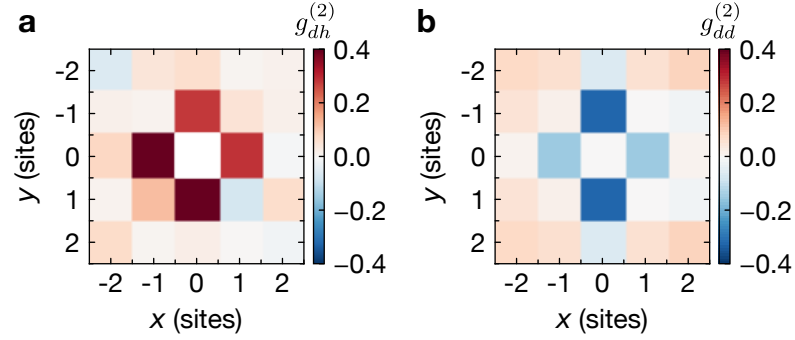
Figure B.2: Density correlations. Correlations between **a**, doublons and holes, **b**, doublons and doublons in the mobile doublon dataset as a function of their mutual distance r.

and strongly-magnetized clouds, we only considered shots with a total spin of $|\sum \hat{S}_i^z| = |\hat{S}_{tot}^z| \leq 3.5$, which corresponds to a maximum allowed magnetization per particle of $|\hat{S}_{tot}^z|/N \approx 0.05$. After this step, 68 % of shots remain. We performed all further analyses in a region of interest (ROI), which is defined as all sites with average density $n \geq 0.7$.

Due to the larger lattice spacing in the y-direction, a relatively high scattering length was required to reach the strongly-interacting regime. To filter out events of inelastic three-body collisions, we filtered on the total number of holes within the ROI, as shown in Fig. B.3. This filter discarded all snapshots with more than 7 holes in the ROI, which amounts to neglecting another 16 % of the data. The final histogram of the number of atoms N and the total spin S_{tot}^z within the ROI after all processing steps is shown in Fig. B.3b,c for the dataset with mobile doublons. The histogram in Fig. 3.3b was also computed after all processing steps.

B.4 Thermometry

To estimate the temperature of the experimental system, comparison to NLCE calculations was performed for NN spin correlations $C(d = 1)$ (with normalization $\eta = 4$) at densities around half filling. We compared to calculations at $U/t = 13$, which is the lower estimate of U for the experimental system. The lower the assumed U/t, the higher will be the estimated temperature in units of t. This lower bound for U takes into account a renormalization for low lattice depths [245] and therefore allows a very conservative estimation of temperature. The experimental spin correlations as a function of density were obtained by averaging over sites with local densities between 0.9 and 1.1 in bins ranging from 0.02 to 0.04 to collect enough statistics. We find that
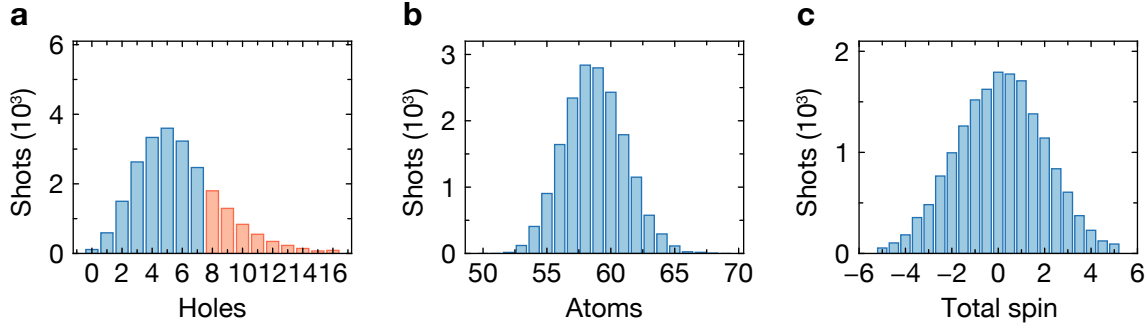
Figure B.3: Histograms of the dataset for mobile doublons. Number of snapshots with a certain **a**, number of atoms, **b**, total spin S_{tot}^z and **c**, total number of holes on lattice sites with density greater than 0.7. Red bars in **c** indicate shots discarded by the applied hole filter (see text).

our experimental correlations compare well with NLCE results at a temperature of $T/t \in [0.43, 0.46]$, see Fig. B.4. Considering the uncertainty in the exact interaction U, we therefore estimate $T/t = 0.45^{+3}_{-1}$.

B.5 Tweezer inhomogeneities

This section elaborates on the effect of tweezer imperfections on spin correlations in the vicinity of the pinned dopant.

The intensity of the 702 nm tweezer light should radially fall off to 30 % at a distance of 600 nm from the maximum, given the point-spread function at a $NA = 0.5$. The lattice spacings for measurements in chapter 3 were $a_x = 1.15\,\mu$m and $a_y = 2.3\,\mu$m. We know from an experimental determination of our point-spread function that two asymmetric distorted side maxima with around 10 % intensity exist. Furthermore, imperfections in the compensation of chromatic focal shifts between our imaging light at 671 nm and the tweezer light will lead to a spot size of the focused 702 nm light at the target lattice site slightly larger than the theoretical minimum. Therefore, finite energy shifts will be imparted on lattice sites, which are nearest neighbor to the target site. We approximate the tweezer depth at the deepest point to be of order U. Therefore we expect energy shifts up to $0.3\,U$ on neighboring sites. The density of the two sites, which are direct neighbors along the shorter-space x-direction, is 1.024(5) and 1.059(5) and therefore slightly increased w.r.t. the surrounding sites at half filling. This confirms that these sites are indeed detuned by the presence of the tweezer beam.

A detuning Δ of the sites neighboring the target site leads to an altered spin ex-
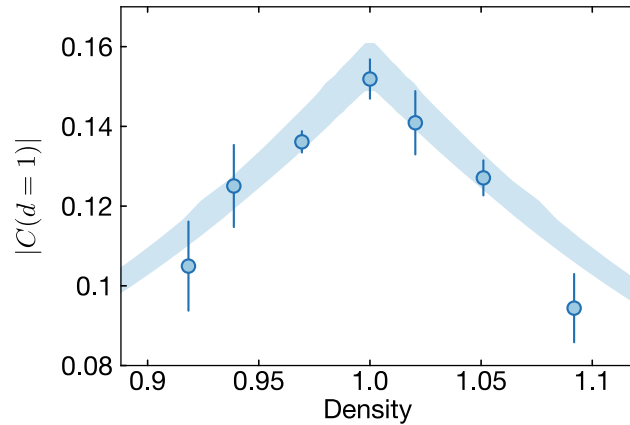
Figure B.4: Temperature estimation. Experimental nearest-neighbor spin correlations as a function of density in the system with mobile doublons. The normalization is $\eta = 4$. Upper (lower) values of the blue band correspond to correlations extracted from NLCE calculations at $T/t = 0.43$ (0.46) and $U/t = 13$.

change of those sites with all of their NN sites. The effective spin exchange between two lattice sites at a mutual detuning Δ is given by $J = 2t^2[1/(U + \Delta) + 1/(U - \Delta)]$ [246]. When performing exact diagonalization calculations in the t-J model for pinned dopants, such an effect could be taken into account by increasing the spin exchange coupling J by 10 % between the sites surrounding the pinned dopant. As discussed in the main text, this adjustment captures the experimentally observed enhancement of NN spin correlations in the vicinity of the trapped dopant.

C

Supplementary information for chapter 4

C.1 Thermometry

To estimate the temperature of all four datasets [D1,D2,D3,D4] of chapter 4, we start by confirming the interaction strength for the experimental settings.

Given the calibration of our experimental parameters, a Wannier function calculation estimates the interaction strength to be $U/t = 9.3$ for D1 and $U/t = 8.2$ for [D2,D3,D4]. As the on-site magnetic moment is very sensitive around $U/t = 8$, we compare $\langle \hat{m}_z^2 \rangle$ at half filling between experiment and NLCE calculations of [209]. The single-particle detection fidelity p is slightly different across datasets and estimated to be $p = 97\,\%$ for D1 and $p = 95\,\%$ for [D2,D3,D4] by comparing occupations in subsequent images of the same realization. When correcting for this detection fidelity, the experimental magnetic moment agrees with numerical data at an interaction of $U/t = 8.6$ for D1 and $U/t = 6.7$ for [D2,D3,D4], see Fig. C.1a. We therefore combine our calibration with the information from NLCE to assess the interaction strength to be 8.9(4) for D1 and 7.4(8) for [D2,D3,D4].

To estimate the temperature of datasets, we compare NN spin correlations $C(d = 1)$ (normalization η=4) at half filling to the NLCE data. Taking into account the detection fidelity for each dataset, we find our data is consistent with temperatures T/t of $[0.43(3), 0.52(5), 0.77(7)]$ for datasets [D1,D2,D4], see Fig. C.1b,c. Uncertainties for the temperature are estimated by the best- and worst-case scenarios, given the statistical errorbar of the spin correlation and the uncertainty in U/t. Dataset D3 does not have a region at half filling, but it was taken in the same measurement run as D2 and spin correlations between D2 and D3 agree at the same doping. Therefore, we infer the temperature of those two datasets to be the same.
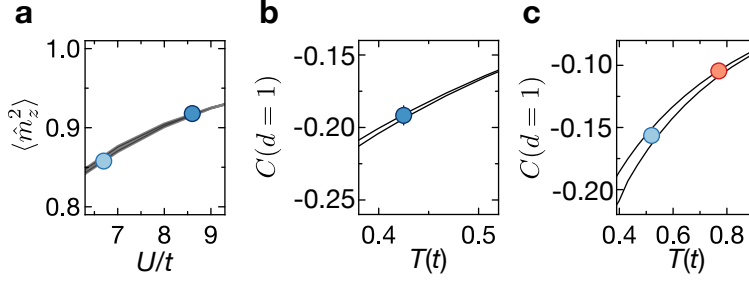
Figure C.1: Recalibration of interaction strength and temperature estimation. a. NLCE data (solid black) of on-site magnetic moment, resummed from [209], as a function of interaction strength U/t at half filling for temperatures of $T/t = 0.76$ (lower line) and $T/t = 0.40$ (upper line). Dark (light) blue data points correspond to datasets D1 (D2), which are plotted at a U/t of 8.6 (6.7), which is where numerical and experimental data coincide. **b, c,** NLCE calculations (solid black) of $C(d = 1)$ ($\eta = 4$) at half filling versus temperature. Upper (lower) curves are at U/t of 7 (9) in **b**, and at U/t of 6 (8) in **c**. Points in (dark blue, light blue, red) were extracted from datasets (D1,D2,D4), for which we estimate a temperature of $(0.43(3), 0.52(5), 0.77(7))$. For experimental data a density filter of $[0.96, 1.03]$ was used for dataset D1 and $[0.92, 0.97]$ for datasets D2, D3, D4.

C.2 Structure factors

Chapter 4 studied the static spin structure factor $S(q)$ along with an offset-adjusted version $S^\star(q)$ and found incommensurate fluctuations, which became visible around quarter filling. Here, we provide further information on $S(q)$ and present the density structure factor $N(q)$.

The bare spin structure factor $S(q)$ and its doping dependence is plotted in Fig. C.2a. Similar to $S^\star(q)$, incommensurate fluctuations are visible around quarter filling, i.e. at $\delta = n = 0.5$.

The density structure factor $N(q)$ was computed in analogy to $S(q)$. In this case, density correlations $\langle \hat{n}_{r_i} \hat{n}_{r+d} \rangle$ were Fourier transformed instead of spin correlations. As shown in Fig. C.2b, there are no incommensurate fluctuations visible at any doping in our measurements. The signal at wavevector (π, π) can be interpreted to originate from negative correlations between fermions at short NN distances.
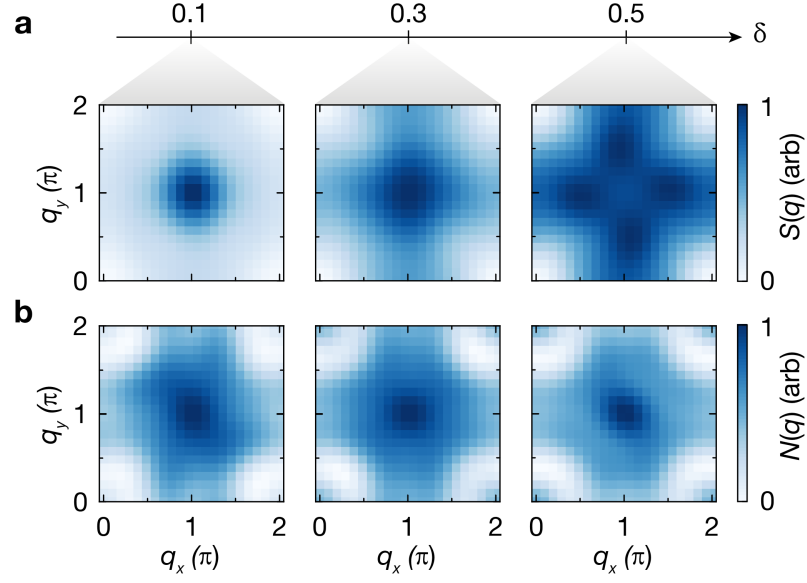
Figure C.2: Spin and density structure factors. a Static spin structure factor $S(q)$ and **b**, static density structure factor $N(q)$ at different hole dopings. Incommensurate fluctuations are visible in $S(q)$ at high doping. Such incommensurate behavior is not detected in $N(q)$. The total width of doping bins for averaging is 0.15. This figure is based on dataset D1. Maximum values of colorscales vary between images, which means colorscales between images are not comparable.

C.3 Connected correlator expressions

For all analyses of chapter 4, the most general expressions ($\langle \hat{S}_r^z \rangle \neq 0$) for connected correlators were evaluated with experimental data. These expressions are

$$
\begin{aligned}
C_3^c(\boldsymbol{r}_1, \boldsymbol{r}_2, \boldsymbol{r}_3) = {} & \langle \hat{h}_3 \hat{S}_2^z \hat{S}_1^z \rangle \\
& - \langle \hat{h}_3 \rangle \langle \hat{S}_2^z \hat{S}_1^z \rangle - \langle \hat{S}_2^z \rangle \langle \hat{h}_3 \hat{S}_1^z \rangle \\
& - \langle \hat{S}_1^z \rangle \langle \hat{h}_3 \hat{S}_2^z \rangle + 2 \langle \hat{h}_3 \rangle \langle \hat{S}_2^z \rangle \langle \hat{S}_1^z \rangle,
\end{aligned}
\tag{C.1}
$$

$$C_4^c(\boldsymbol{r}_1, \boldsymbol{r}_2, \boldsymbol{r}_3, \boldsymbol{r}_4) = \langle \hat{h}_4 \hat{h}_3 \hat{S}_2^z \hat{S}_1^z \rangle \tag{C.2}$$
$$-\langle \hat{h}_4 \rangle \langle \hat{h}_3 \hat{S}_2^z \hat{S}_1^z \rangle - \langle \hat{h}_3 \rangle \langle \hat{h}_4 \hat{S}_2^z \hat{S}_1^z \rangle$$
$$-\langle \hat{h}_4 \hat{h}_3 \rangle \langle \hat{S}_2^z \hat{S}_1^z \rangle + 2 \langle \hat{S}_2^z \hat{S}_1^z \rangle \langle \hat{h}_4 \rangle \langle \hat{h}_3 \rangle$$
$$-\langle \hat{S}_2^z \rangle \langle \hat{h}_4 \hat{h}_3 \hat{S}_1^z \rangle - \langle \hat{S}_1^z \rangle \langle \hat{h}_4 \hat{h}_3 \hat{S}_2^z \rangle$$
$$-\langle \hat{h}_4 \hat{S}_2^z \rangle \langle \hat{h}_3 \hat{S}_1^z \rangle - \langle \hat{h}_4 \hat{S}_1^z \rangle \langle \hat{h}_3 \hat{S}_2^z \rangle$$
$$+2 \langle \hat{h}_4 \hat{h}_3 \rangle \langle \hat{S}_2^z \rangle \langle \hat{S}_1^z \rangle + 2 \langle \hat{h}_4 \hat{S}_2^z \rangle \langle \hat{h}_3 \rangle \langle \hat{S}_1^z \rangle$$
$$+2 \langle \hat{h}_4 \hat{S}_1^z \rangle \langle \hat{h}_3 \rangle \langle \hat{S}_2^z \rangle + 2 \langle \hat{h}_3 \hat{S}_2^z \rangle \langle \hat{h}_4 \rangle \langle \hat{S}_1^z \rangle$$
$$+2 \langle \hat{h}_3 \hat{S}_1^z \rangle \langle \hat{h}_4 \rangle \langle \hat{S}_2^z \rangle - 6 \langle \hat{h}_4 \rangle \langle \hat{h}_3 \rangle \langle \hat{S}_2^z \rangle \langle \hat{S}_1^z \rangle,$$

and their post-selected normalized forms

$$C_\circ^c = C_3^c / (\langle \hat{h}_3 \rangle \sigma(\hat{S}_2^z) \sigma(\hat{S}_1^z)), \tag{C.3}$$

$$C_{\circ\circ}^c = C_4^c / (\langle \hat{h}_4 \hat{h}_3 \rangle \sigma(\hat{S}_2^z) \sigma(\hat{S}_1^z)), \tag{C.4}$$

where we used an abbreviated subscript notation $\hat{O}_i$ for the operator $\hat{O}$ at position $\boldsymbol{r}_i$.

Bibliography

[1] N. W. Ashcroft and N. D. Mermin. *Solid state physics*. Saunders College Publishing (1976). (Cited on page 1)

[2] J. Haschke, O. Dupré, M. Boccard, and C. Ballif. *Silicon heterojunction solar cells: Recent technological development and practical aspects - from lab to industry*. Sol. Energy Mater. Sol. Cells **187**, 140–153 (2018). (Cited on page 1)

[3] G. Aad et. al. *Observation of a new particle in the search for the Standard Model Higgs boson with the ATLAS detector at the LHC*. Phys. Lett. B **716**, 1–29 (2012). (Cited on page 1)

[4] S. Chatrchyan et. al. *Observation of a new boson at a mass of 125 GeV with the CMS experiment at the LHC*. Phys. Lett. B **716**, 30–61 (2012). (Cited on page 1)

[5] H. v. Löhneysen, T. Pietrus, G. Portisch, H. G. Schlager, A. Schröder, M. Sieck, and T. Trappmann. *Non-Fermi-liquid behavior in a heavy-fermion alloy at a magnetic instability*. Phys. Rev. Lett. **72**, 3262–3265 (1994). (Cited on page 1)

[6] Y. Kurosaki, Y. Shimizu, K. Miyagawa, K. Kanoda, and G. Saito. *Mott Transition from a Spin Liquid to a Fermi Liquid in the Spin-Frustrated Organic Conductor $\kappa-(ET)_2Cu_2(CN)_3$*. Phys. Rev. Lett. **95**, 177001 (2005). (Cited on page 1)

[7] C. M. Varma, P. B. Littlewood, S. Schmitt-Rink, E. Abrahams, and A. E. Ruckenstein. *Phenomenology of the normal state of Cu-O high-temperature superconductors*. Phys. Rev. Lett. **63**, 1996–1999 (1989). (Cited on pages 1 and 16)

[8] L. D. Landau. *The theory of a Fermi liquid*. J. Exp. Theor. Phys. **30**, 1058 (1956). (Cited on page 1)

[9] P. Coleman. *Introduction to Many-Body Physics*. Cambridge University Press, Cambridge (2015). (Cited on pages 1, 10, 23, 28, and 96)

[10] B. Keimer, S. A. Kivelson, M. R. Norman, S. Uchida, and J. Zaanen. *From quantum matter to high-temperature superconductivity in copper oxides*. Nature **518**, 179–186 (2015). (Cited on pages 1, 2, 7, 8, 9, 10, 11, 86, and 101)

[11] A. P. Drozdov, P. P. Kong, V. S. Minkov, S. P. Besedin, M. A. Kuzovnikov, S. Mozaffari, L. Balicas, F. F. Balakirev, D. E. Graf, V. B. Prakapenka, E. Greenberg, D. A. Knyazev, M. Tkacz, and M. I. Eremets. *Superconductivity at 250 K in lanthanum hydride under high pressures.* Nature **569**, 528–531 (2019). (Cited on page **1**)

[12] E. Snider, N. Dasenbrock-Gammon, R. McBride, M. Debessai, H. Vindana, K. Vencatasamy, K. V. Lawler, A. Salamat, and R. P. Dias. *Room-temperature superconductivity in a carbonaceous sulfur hydride.* Nature **586**, 373–377 (2020). (Cited on page **1**)

[13] E. Dagotto. *Correlated electrons in high-temperature superconductors.* Rev. Mod. Phys. **66**, 763–840 (1994). (Cited on pages **1**, **2**, **7**, **9**, **58**, and **101**)

[14] P. A. Lee, N. Nagaosa, and X.-G. Wen. *Doping a Mott insulator: Physics of high-temperature superconductivity.* Rev. Mod. Phys. **78**, 17–85 (2006). (Cited on pages **1**, **2**, **7**, **9**, **11**, **12**, **13**, **16**, **18**, **28**, and **86**)

[15] D. S. Marshall, D. S. Dessau, A. G. Loeser, C.-H. Park, A. Y. Matsuura, J. N. Eckstein, I. Bozovic, P. Fournier, A. Kapitulnik, W. E. Spicer, and Z.-X. Shen. *Unconventional Electronic Structure Evolution with Hole Doping in* $Bi_2Sr_2CaCu_2O_{8+\delta}$*: Angle-Resolved Photoemission Results.* Phys. Rev. Lett. **76**, 4841–4844 (1996). (Cited on pages **1**, **9**, and **71**)

[16] A. Kaminski, S. Rosenkranz, H. M. Fretwell, Z. Z. Li, H. Raffy, M. Randeria, M. R. Norman, and J. C. Campuzano. *Crossover from Coherent to Incoherent Electronic Excitations in the Normal State of* $Bi_2Sr_2CaCu_2O_{8+\delta}$*.* Phys. Rev. Lett. **90**, 207003 (2003). (Cited on pages **1** and **9**)

[17] M. Platé, J. D. F. Mottershead, I. S. Elfimov, D. C. Peets, R. Liang, D. A. Bonn, W. N. Hardy, S. Chiuzbaian, M. Falub, M. Shi, L. Patthey, and A. Damascelli. *Fermi Surface and Quasiparticle Excitations of Overdoped* $Tl_2Ba_2CuO_{6+\delta}$*.* Phys. Rev. Lett. **95**, 77001 (2005). (Cited on pages **1** and **9**)

[18] S. Badoux, W. Tabis, F. Laliberté, G. Grissonnanche, B. Vignolle, D. Vignolles, J. Béard, D. A. Bonn, W. N. Hardy, R. Liang, N. Doiron-Leyraud, L. Taillefer, and C. Proust. *Change of carrier density at the pseudogap critical point of a cuprate superconductor.* Nature **531**, 210–214 (2016). (Cited on pages **1**, **9**, **10**, **11**, and **86**)

[19] S. D. Chen, M. Hashimoto, Y. He, D. Song, K. J. Xu, J. F. He, T. P. Devereaux, H. Eisaki, D. H. Lu, J. Zaanen, and Z. X. Shen. *Incoherent strange metal sharply bounded by a critical doping in Bi2212.* Science **366**, 1099–1102 (2019). (Cited on pages **1**, **9**, and **86**)

[20] T. Senthil. *Critical Fermi surfaces and non-Fermi liquid metals*. Phys. Rev. B **78**, 35103 (2008). (Cited on page **1**)

[21] C. M. Varma. *Non-Fermi-liquid states and pairing instability of a general model of copper oxide metals*. Phys. Rev. B **55**, 14554–14580 (1997). (Cited on page **2**)

[22] S. Sachdev. *Quantum Phase Transitions*. Cambridge University Press, 2nd edition (2011). (Cited on page **2**)

[23] J. G. Bednorz and K. A. Müller. *Possible high T_c superconductivity in the Ba-La-Cu-O system*. Z. Phys. B Cond. Mat. **64**, 189 (1986). (Cited on page **2**)

[24] J. R. Schrieffer. *Handbook of High-Temperature Superconductivity*. Springer, New York (2007). (Cited on pages **2**, **14**, **15**, and **71**)

[25] P. B. Allen. *Is kinky conventional?* Nature **412**, 494–495 (2001). (Cited on page **2**)

[26] A. Lanzara, P. V. Bogdanov, X. J. Zhou, S. A. Kellar, D. L. Feng, E. D. Lu, T. Yoshida, H. Eisaki, A. Fujimori, K. Kishio, J.-I. Shimoyama, T. Noda, S. Uchida, Z. Hussain, and Z.-X. Shen. *Evidence for ubiquitous strong electron-phonon coupling in high-temperature superconductors*. Nature **412**, 510–514 (2001). (Cited on page **2**)

[27] P. F. LeBlanc, A. E. Antipov, F. Becca, I. W. Bulik, G. K. L. Chan, C. M. Chung, Y. Deng, M. Ferrero, T. M. Henderson, C. A. Jiménez-Hoyos, E. Kozik, X. W. Liu, A. J. Millis, N. V. Prokof'ev, M. Qin, G. E. Scuseria, H. Shi, B. V. Svistunov, L. F. Tocchio, I. S. Tupitsyn, S. R. White, S. Zhang, B. X. Zheng, Z. Zhu, and E. Gull. *Solutions of the Two-Dimensional Hubbard Model: Benchmarks and Results from a Wide Range of Numerical Algorithms*. Phys. Rev. X **5**, 041041 (2015). (Cited on pages **2** and **12**)

[28] B.-B. Chen, C. Chen, Z. Chen, J. Cui, Y. Zhai, A. Weichselbaum, J. von Delft, Z. Y. Meng, and W. Li. *Quantum Many-Body Simulations of the 2D Fermi-Hubbard Model in Ultracold Optical Lattices*. arXiv:2008.02179 (2020). (Cited on pages **2** and **12**)

[29] E. Y. Loh, J. E. Gubernatis, R. T. Scalettar, S. R. White, D. J. Scalapino, and R. L. Sugar. *Sign problem in the numerical simulation of many-electron systems*. Phys. Rev. B **41**, 9301 (1990). (Cited on pages **2** and **12**)

[30] D. J. Scalapino. *A common thread: The pairing interaction for unconventional superconductors*. Rev. Mod. Phys. **84**, 1383–1417 (2012). (Cited on pages **2**, **11**, **12**, **16**, and **71**)

[31] S. Datta. *Ten nanometre CMOS logic technology*. Nat. Electron. **1**, 500–501 (2018). (Cited on page **2**)

[32] S. S. Batsanov. *Van der Waals Radii of Elements*. Inorg. Mater. **37**, 871–885 (2001). (Cited on page **2**)

[33] R. P. Feynman. *Simulating physics with computers*. Int. J. Theor. Phys. **21**, 467 (1982). (Cited on page **2**)

[34] F. Arute, K. Arya, R. Babbush, D. Bacon, J. C. Bardin, R. Barends, R. Biswas, S. Boixo, F. G. S. L. Brandao, D. A. Buell, B. Burkett, Y. Chen, Z. Chen, B. Chiaro, R. Collins, W. Courtney, A. Dunsworth, E. Farhi, B. Foxen, A. Fowler, C. Gidney, M. Giustina, R. Graff, K. Guerin, S. Habegger, M. P. Harrigan, M. J. Hartmann, A. Ho, M. Hoffmann, T. Huang, T. S. Humble, S. V. Isakov, E. Jeffrey, Z. Jiang, D. Kafri, K. Kechedzhi, J. Kelly, P. V. Klimov, S. Knysh, A. Korotkov, F. Kostritsa, D. Landhuis, M. Lindmark, E. Lucero, D. Lyakh, S. Mandrà, J. R. McClean, M. McEwen, A. Megrant, X. Mi, K. Michielsen, M. Mohseni, J. Mutus, O. Naaman, M. Neeley, C. Neill, M. Y. Niu, E. Ostby, A. Petukhov, J. C. Platt, C. Quintana, E. G. Rieffel, P. Roushan, N. C. Rubin, D. Sank, K. J. Satzinger, V. Smelyanskiy, K. J. Sung, M. D. Trevithick, A. Vainsencher, B. Villalonga, T. White, Z. J. Yao, P. Yeh, A. Zalcman, H. Neven, and J. M. Martinis. *Quantum supremacy using a programmable superconducting processor*. Nature **574**, 505–510 (2019). (Cited on page **2**)

[35] H.-S. Zhong, H. Wang, Y.-H. Deng, M.-C. Chen, L.-C. Peng, Y.-H. Luo, J. Qin, D. Wu, X. Ding, Y. Hu, P. Hu, X.-Y. Yang, W.-J. Zhang, H. Li, Y. Li, X. Jiang, L. Gan, G. Yang, L. You, Z. Wang, L. Li, N.-L. Liu, C.-Y. Lu, and J.-W. Pan. *Quantum computational advantage using photons*. Science **370**, 1460 LP – 1463 (2020). (Cited on page **2**)

[36] J. Preskill. *Quantum Computing in the NISQ era and beyond*. Quantum **2**, 79 (2018). (Cited on page **2**)

[37] M. Greiner, O. Mandel, T. Esslinger, T. W. Hänsch, and I. Bloch. *Quantum phase transition from a superfluid to a Mott insulator in a gas of ultracold atoms*. Nature **415**, 39 (2002). (Cited on page **2**)

[38] C. Gross and I. Bloch. *Quantum simulations with ultracold atoms in optical lattices*. Science **357**, 995–1001 (2017). (Cited on page **2**)

[39] I. Bloch, J. Dalibard, and S. Nascimbène. *Quantum simulations with ultracold quantum gases*. Nat. Phys. **8**, 267 (2012). (Cited on page **2**)

[40] T. Esslinger. *Fermi-Hubbard physics with atoms in an optical lattice*. Annu. Rev. Cond. Mat. Phys. **1**, 129 (2010). (Cited on pages **2** and **19**)

[41] P. W. Anderson. *The Resonating Valence Bond State in La2CuO4 and Superconductivity*. Science **235**, 1196–1198 (1987). (Cited on pages **2**, **11**, **12**, **16**, and **18**)

[42] R. Jördens, N. Strohmaier, K. Günter, H. Moritz, and T. Esslinger. *A Mott insulator of fermionic atoms in an optical lattice*. Nature **455**, 204 (2008). (Cited on page **2**)

[43] U. Schneider, L. Hackermüller, S. Will, T. Best, I. Bloch, T. A. Costi, R. W. Helmes, D. Rasch, and A. Rosch. *Metallic and insulating phases of repulsively interacting fermions in a 3D optical lattice*. Science **322**, 1520 (2008). (Cited on page **2**)

[44] D. Greif, T. Uehlinger, G. Jotzu, L. Tarruell, and T. Esslinger. *Short-range quantum magnetism of ultracold fermions in an optical lattice*. Science **340**, 1307 (2013). (Cited on page **2**)

[45] R. A. Hart, P. M. Duarte, T.-L. Yang, X. Liu, T. Paiva, E. Khatami, R. T. Scalettar, N. Trivedi, D. A. Huse, and R. G. Hulet. *Observation of antiferromagnetic correlations in the Hubbard model with ultracold atoms*. Nature **519**, 211 (2015). (Cited on page **2**)

[46] W. S. Bakr, J. I. Gillen, A. Peng, S. Fölling, and M. Greiner. *A quantum gas microscope for detecting single atoms in a Hubbard-regime optical lattice*. Nature **462**, 74–77 (2009). (Cited on pages **3**, **19**, **22**, and **62**)

[47] J. F. Sherson, C. Weitenberg, M. Endres, M. Cheneau, I. Bloch, and S. Kuhr. *Single-atom-resolved fluorescence imaging of an atomic Mott insulator*. Nature **467**, 68 (2010). (Cited on pages **3**, **19**, **22**, and **62**)

[48] C. Weitenberg, M. Endres, J. F. Sherson, M. Cheneau, P. Schauss, T. Fukuhara, I. Bloch, and S. Kuhr. *Single-spin addressing in an atomic Mott insulator*. Nature **471**, 319 (2011). (Cited on page **3**)

[49] A. Omran, M. Boll, T. A. Hilker, K. Kleinlein, G. Salomon, I. Bloch, and C. Gross. *Microscopic Observation of Pauli Blocking in Degenerate Fermionic Lattice Gases*. Phys. Rev. Lett. **115**, 1–5 (2015). (Cited on pages **3**, **19**, **22**, **35**, and **36**)

[50] L. W. Cheuk, M. A. Nichols, M. Okan, T. Gersdorf, V. V. Ramasesh, W. S. Bakr, T. Lompe, and M. W. Zwierlein. *Quantum-gas microscope for fermionic atoms*. Phys. Rev. Lett. **114**, 1–5 (2015). (Cited on pages **3**, **19**, and **22**)

[51] M. F. Parsons, F. Huber, A. Mazurenko, C. S. Chiu, W. Setiawan, K. Wooley-Brown, S. Blatt, and M. Greiner. *Site-Resolved imaging of fermionic li 6 in an optical lattice*. Phys. Rev. Lett. **114**, 213002 (2015). (Cited on pages **3**, **19**, and **22**)

[52] E. Haller, J. Hudson, A. Kelly, D. A. Cotta, B. Peaudecerf, G. D. Bruce, and S. Kuhr. *Single-atom imaging of fermions in a quantum-gas microscope.* Nat. Phys. **11**, 738–742 (2015). (Cited on pages **3** and **19**)

[53] G. J. A. Edge, R. Anderson, D. Jervis, D. C. McKay, R. Day, S. Trotzky, and J. H. Thywissen. *Imaging and addressing of individual fermionic atoms in an optical lattice.* Phys. Rev. A **92**, 063406 (2015). (Cited on pages **3** and **19**)

[54] M. F. Parsons, A. Mazurenko, C. S. Chiu, G. Ji, D. Greif, and M. Greiner. *Site-resolved measurement of the spin-correlation function in the Fermi-Hubbard model.* Science **353**, 1253–1256 (2016). (Cited on pages **3**, **22**, **33**, **62**, and **76**)

[55] L. W. Cheuk, M. A. Nichols, K. R. Lawrence, M. Okan, H. Zhang, E. Khatami, N. Trivedi, T. Paiva, M. Rigol, and M. W. Zwierlein. *Observation of spatial charge and spin correlations in the 2D Fermi-Hubbard model.* Science **353**, 1260–1265 (2016). (Cited on pages **3**, **22**, **62**, and **76**)

[56] M. Boll, T. A. Hilker, G. Salomon, A. Omran, J. Nespolo, L. Pollet, I. Bloch, and C. Gross. *Spin- and density-resolved microscopy of antiferromagnetic correlations in Fermi-Hubbard chains.* Science **353**, 1257–1260 (2016). (Cited on pages **3**, **22**, **62**, and **72**)

[57] T. A. Hilker, G. Salomon, F. Grusdt, A. Omran, M. Boll, E. Demler, I. Bloch, and C. Gross. *Revealing hidden antiferromagnetic correlations in doped Hubbard chains via string correlators.* Science **357**, 484–487 (2017). (Cited on pages **3**, **19**, **62**, and **83**)

[58] G. Salomon, J. Koepsell, J. Vijayan, T. A. Hilker, J. Nespolo, L. Pollet, I. Bloch, and C. Gross. *Direct observation of incommensurate magnetism in Hubbard chains.* Nature **565**, 56–60 (2019). (Cited on pages **3**, **33**, **62**, and **83**)

[59] M. A. Nichols, L. W. Cheuk, M. Okan, T. R. Hartke, E. Mendez, T. Senthil, E. Khatami, H. Zhang, and M. W. Zwierlein. *Spin Transport in a Mott Insulator of Ultracold Fermions.* Science **363**, 383–387 (2019). (Cited on pages **3** and **107**)

[60] P. T. Brown, D. Mitra, E. Guardado-Sanchez, R. Nourafkan, A. Reymbaut, C. D. Hébert, S. Bergeron, A. M. Tremblay, J. Kokalj, D. A. Huse, P. Schauß, and W. S. Bakr. *Bad metallic transport in a cold atom Fermi-Hubbard system.* Science **363**, 379–382 (2019). (Cited on pages **3**, **33**, and **107**)

[61] A. Mazurenko, C. S. Chiu, G. Ji, m. F. Parsons, M. Kanász-Nagy, R. Schmidt, F. Grusdt, E. Demler, D. Greif, and M. Greiner. *A cold-atom Fermi-Hubbard antiferromagnet.* Nature **545**, 462–466 (2017). (Cited on pages **3**, **33**, **65**, and **107**)

[62] Q. Zhou and T. L. Ho. *Universal thermometry for quantum simulation.* Phys. Rev. Lett. **106,** 225301 (2011). (Cited on pages **3** and **96**)

[63] J. H. Drewes, E. Cocchi, L. A. Miller, C. F. Chan, D. Pertot, F. Brennecke, and M. Köhl. *Thermodynamics versus Local Density Fluctuations in the Metal-Mott-Insulator Crossover.* Phys. Rev. Lett. **117,** 135301 (2016). (Cited on pages **3**, **67**, and **96**)

[64] T. Hartke, B. Oreg, N. Jia, and M. Zwierlein. *Doublon-Hole Correlations and Fluctuation Thermometry in a Fermi-Hubbard Gas.* Phys. Rev. Lett. **125,** 113601 (2020). (Cited on pages **3**, **67**, **96**, and **97**)

[65] J. T. Stewart, J. P. Gaebler, and D. S. Jin. *Using photoemission spectroscopy to probe a strongly interacting Fermi gas.* Nature **454,** 744–747 (2008). (Cited on pages **3** and **83**)

[66] J. P. Gaebler, J. T. Stewart, T. E. Drake, D. S. Jin, A. Perali, P. Pieri, and G. C. Strinati. *Observation of pseudogap behaviour in a strongly interacting Fermi gas.* Nat. Phys. **6,** 569–573 (2010). (Cited on pages **3** and **16**)

[67] M. Feld, B. Fröhlich, E. Vogt, M. Koschorreck, and M. Köhl. *Observation of a pairing pseudogap in a two-dimensional Fermi gas.* Nature **480,** 75–78 (2011). (Cited on page **3**)

[68] P. T. Brown, E. Guardado-Sanchez, B. M. Spar, E. W. Huang, T. P. Devereaux, and W. S. Bakr. *Angle-resolved photoemission spectroscopy of a Fermi-Hubbard system.* Nat. Phys. **16,** 26–31 (2020). (Cited on pages **3** and **83**)

[69] J. Vijayan, P. Sompet, G. Salomon, J. Koepsell, S. Hirthe, A. Bohrdt, F. Grusdt, I. Bloch, and C. Gross. *Time-Resolved Observation of Spin-Charge Deconfinement in Fermionic Hubbard Chains.* Science **367,** 186–189 (2019). (Cited on pages **3**, **62**, **83**, and **106**)

[70] G. Ji, M. Xu, L. H. Kendrick, C. S. Chiu, J. C. Brüggenjürgen, D. Greif, A. Bohrdt, F. Grusdt, E. Demler, M. Lebrat, and M. Greiner. *Dynamical interplay between a single hole and a Hubbard antiferromagnet.* arXiv:2006.06672 (2020). (Cited on pages **3**, **83**, **106**, and **107**)

[71] J. Koepsell, S. Hirthe, D. Bourgund, P. Sompet, J. Vijayan, G. Salomon, C. Gross, and I. Bloch. *Robust Bilayer Charge Pumping for Spin- and Density-Resolved Quantum Gas Microscopy.* Phys. Rev. Lett. **125,** 10403 (2020). (Cited on pages **3** and **22**)

[72] C. S. Chiu, G. Ji, A. Bohrdt, M. Xu, M. Knap, E. Demler, F. Grusdt, M. Greiner, and D. Greif. *String patterns in the doped Hubbard model.* Science **365,** 251–256 (2019). (Cited on pages **3**, **18**, **76**, **94**, **101**, and **107**)

[73] R. Liang, D. A. Bonn, and W. N. Hardy. *Growth of YBCO single crystals by the self-flux technique*. Philos. Mag. **92**, 2563–2581 (2012). (Cited on page **8**)

[74] F. C. Zhang and T. M. Rice. *Effective Hamiltonian for the superconducting Cu oxides*. Phys. Rev. B **37**, 3759–3761 (1988). (Cited on page **7**)

[75] N. F. Mott. *The basis of the electron theory of metals, with special reference to the transition metals*. Proc. Phys. Soc. **62**, 416 (1949). (Cited on page **7**)

[76] D. Vaknin, S. K. Sinha, D. E. Moncton, D. C. Johnston, J. M. Newsam, C. R. Safinya, and H. E. King. *Antiferromagnetism in* La_2CuO_{4-y}. Phys. Rev. Lett. **58**, 2802–2805 (1987). (Cited on page **8**)

[77] S. Chakravarty, B. I. Halperin, and D. R. Nelson. *Low-temperature behavior of two-dimensional quantum antiferromagnets*. Phys. Rev. Lett. **60**, 1057–1060 (1988). (Cited on page **8**)

[78] M. Frachet, I. Vinograd, R. Zhou, S. Benhabib, S. Wu, H. Mayaffre, S. Krämer, S. K. Ramakrishna, A. P. Reyes, J. Debray, T. Kurosawa, N. Momono, M. Oda, S. Komiya, S. Ono, M. Horio, J. Chang, C. Proust, D. LeBoeuf, and M.-H. Julien. *Hidden magnetism at the pseudogap critical point of a cuprate superconductor*. Nat. Phys. **16**, 1064–1068 (2020). (Cited on page **9**)

[79] H.-B. Yang, J. D. Rameau, P. D. Johnson, T. Valla, A. Tsvelik, and G. D. Gu. *Emergence of preformed Cooper pairs from the doped Mott insulating state in Bi2Sr2CaCu2O8+δ*. Nature **456**, 77–80 (2008). (Cited on page **9**)

[80] N. E. Hussey, K. Takenaka, and H. Takagi. *Universality of the Mott-Ioffe-Regel limit in metals*. Philos. Mag. **84**, 2847–2864 (2004). (Cited on pages **9** and **11**)

[81] M. R. Norman, H. Ding, M. Randeria, J. C. Campuzano, T. Yokoya, T. Takeuchi, T. Takahashi, T. Mochiku, K. Kadowaki, P. Guptasarma, and D. G. Hinks. *Destruction of the Fermi surface in underdoped high-Tc superconductors*. Nature **392**, 157–160 (1998). (Cited on page **9**)

[82] N. Doiron-Leyraud, C. Proust, D. LeBoeuf, J. Levallois, J. B. Bonnemaison, R. Liang, D. A. Bonn, W. N. Hardy, and L. Taillefer. *Quantum oscillations and the Fermi surface in an underdoped high-T c superconductor*. Nature **447**, 565–568 (2007). (Cited on page **9**)

[83] E. A. Yelland, J. Singleton, C. H. Mielke, N. Harrison, F. F. Balakirev, B. Dabrowski, and J. R. Cooper. *Quantum Oscillations in the Underdoped Cuprate* $YBa_2Cu_4O_8$. Phys. Rev. Lett. **100**, 47003 (2008). (Cited on page **9**)

[84] S. E. Sebastian, N. Harrison, F. F. Balakirev, M. M. Altarawneh, P. A. Goddard, R. Liang, D. A. Bonn, W. N. Hardy, and G. G. Lonzarich. *Normal-state nodal electronic structure in underdoped high-Tc copper oxides*. Nature **511**, 61–64 (2014). (Cited on page **9**)

[85] H.-B. Yang, J. D. Rameau, Z.-H. Pan, G. D. Gu, P. D. Johnson, H. Claus, D. G. Hinks, and T. E. Kidd. *Reconstructed Fermi Surface of Underdoped* $Bi_2Sr_2CaCu_2O_{8+\delta}$ *Cuprate Superconductors*. Phys. Rev. Lett. **107**, 47003 (2011). (Cited on page **9**)

[86] A. Bohrdt, E. Demler, F. Pollmann, M. Knap, and F. Grusdt. *Parton theory of angle-resolved photoemission spectroscopy spectra in antiferromagnetic Mott insulators*. Phys. Rev. B **102**, 35139 (2020). (Cited on page **9**)

[87] T. Nakano, M. Oda, C. Manabe, N. Momono, Y. Miura, and M. Ido. *Magnetic properties and electronic conduction of superconducting* $La_{2-x}Sr_xCuO_4$. Phys. Rev. B **49**, 16000–16008 (1994). (Cited on page **10**)

[88] A. P. Mackenzie, S. R. Julian, D. C. Sinclair, and C. T. Lin. *Normal-state magnetotransport in superconducting* $Tl_2Ba_2CuO_{6+ffi}$ *to millikelvin temperatures*. Phys. Rev. B **53**, 5848–5855 (1996). (Cited on pages **10** and **11**)

[89] H. Alloul, T. Ohno, and P. Mendels. ^{89}Y *NMR evidence for a fermi-liquid behavior in* $YBa_2Cu_3O_{6+x}$. Phys. Rev. Lett. **63**, 1700–1703 (1989). (Cited on page **10**)

[90] N. J. Curro, T. Imai, C. P. Slichter, and B. Dabrowski. *High-temperature* $^{63}Cu(2)$ *nuclear quadrupole and magnetic resonance measurements of* $YBa_2Cu_4O_8$. Phys. Rev. B **56**, 877–885 (1997). (Cited on page **10**)

[91] N. E. Hussey. *Phenomenology of the normal state in-plane transport properties of high-Tccuprates*. J. Phys. Condens. Matter **20**, 123201 (2008). (Cited on page **11**)

[92] J. M. Tranquada, B. J. Sternlieb, J. D. Axe, Y. Nakamura, and S. Uchida. *Evidence for stripe correlations of spins and holes in copper oxide superconductors*. Nature **375**, 561–563 (1995). (Cited on page **11**)

[93] D. A. Wollman, D. J. Van Harlingen, W. C. Lee, D. M. Ginsberg, and A. J. Leggett. *Experimental determination of the superconducting pairing state in YBCO from the phase coherence of YBCO-Pb dc SQUIDs*. Phys. Rev. Lett. **71**, 2134–2137 (1993). (Cited on page **11**)

[94] C. C. Tsuei and J. R. Kirtley. *Pairing symmetry in cuprate superconductors*. Rev. Mod. Phys. **72**, 969–1016 (2000). (Cited on page **11**)

[95] D. Reznik, L. Pintschovius, M. Ito, S. Iikubo, M. Sato, H. Goka, M. Fujita, K. Yamada, G. D. Gu, and J. M. Tranquada. *Electron-phonon coupling reflecting dynamic charge inhomogeneity in copper oxide superconductors*. Nature **440**, 1170–1173 (2006). (Cited on page **11**)

[96] J. Hubbard. *Electron correlations in narrow energy bands*. Proc. R. Soc. Lond. A **276**, 238 (1963). (Cited on page **12**)

[97] A. Auerbach. *Interacting Electrons and Quantum Magnetism*. Springer, Berlin (1998). (Cited on pages **12**, **13**, **14**, and **15**)

[98] E. Blomquist and J. Carlström. *Ab initio description of magnetic polarons in a Mott insulator*. arXiv:1912.08825 (2019). (Cited on page **12**)

[99] N. D. Mermin and H. Wagner. *Absence of Ferromagnetism or Antiferromagnetism in One- or Two-Dimensional Isotropic Heisenberg Models*. Phys. Rev. Lett. **17**, 1133–1136 (1966). (Cited on page **13**)

[100] A. Altland and B. D. Simons. *Condensed Matter Field Theory*. Cambridge University Press (2010). (Cited on page **14**)

[101] S. Schmitt-Rink, C. M. Varma, and A. E. Ruckenstein. *Spectral function of holes in a quantum antiferromagnet*. Phys. Rev. Lett. **60**, 2793–2796 (1988). (Cited on pages **14** and **71**)

[102] B. I. Shraiman and E. D. Siggia. *Mobile Vacancies in a Quantum Heisenberg Antiferromagnet*. Phys. Rev. Lett. **61**, 467–470 (1988). (Cited on pages **14** and **71**)

[103] J. R. Schrieffer, X.-G. Wen, and S.-C. Zhang. *Spin-bag mechanism of high-temperature superconductivity*. Phys. Rev. Lett. **60**, 944–947 (1988). (Cited on pages **14** and **71**)

[104] S. Sachdev. *Hole motion in a quantum Néel state*. Phys. Rev. B **39**, 12232–12247 (1989). (Cited on pages **14** and **71**)

[105] C. L. Kane, P. A. Lee, and N. Read. *Motion of a single hole in a quantum antiferromagnet*. Phys. Rev. B **39**, 6880–6897 (1989). (Cited on pages **14** and **71**)

[106] E. Dagotto, A. Moreo, and T. Barnes. *Hubbard model with one hole: Ground-state properties*. Phys. Rev. B **40**, 6721–6725 (1989). (Cited on pages **14** and **71**)

[107] F. Grusdt, M. Kánasz-Nagy, A. Bohrdt, C. S. Chiu, G. Ji, M. Greiner, D. Greif, and E. Demler. *Parton Theory of Magnetic Polarons: Mesonic Resonances and Signatures in Dynamics*. Phys. Rev. X **8**, 11046 (2018). (Cited on pages **14**, **16**, **18**, **71**, and **81**)

[108] F. Ronning, K. M. Shen, N. P. Armitage, A. Damascelli, D. H. Lu, Z. X. Shen, L. L. Miller, and C. Kim. *Anomalous high-energy dispersion in angle-resolved photoemission spectra from the insulating cuprate Ca 2CuO 2Cl 2*. Phys. Rev. B **71**, 094518 (2005). (Cited on page **14**)

[109] Y. Nagaoka. *Ferromagnetism in a narrow, almost half-filled s band*. Phys. Rev. **147**, 392–405 (1966). (Cited on page **15**)

[110] J. R. Schrieffer, X. . Wen, and S. C. Zhang. *Dynamic spin fluctuations and the bag mechanism of high-T, superconductivity*. Phys. Rev. B **39**, 11663–11679 (1989). (Cited on pages **16** and **101**)

[111] S. R. White and D. Scalapino. *Hole and pair structures in the t-J model*. Phys. Rev. B **55**, 6504–6517 (1997). (Cited on pages **16**, **25**, **71**, **80**, and **104**)

[112] E. Blomquist and J. Carlström. *Evidence of attraction between charge-carriers in a doped Mott insulator*. arXiv:2007.15011 (2020). (Cited on pages **16**, **104**, and **105**)

[113] J. Bardeen, L. N. Cooper, and J. R. Schrieffer. *Theory of superconductivity*. Phys. Rev. **108**, 1175 (1957). (Cited on page **16**)

[114] P. A. Murthy, M. Neidig, R. Klemt, L. Bayha, I. Boettcher, T. Enss, M. Holten, G. Zürn, P. M. Preiss, and S. Jochim. *High-temperature pairing in a strongly interacting two-dimensional Fermi gas*. Science **359**, 452–455 (2018). (Cited on page **16**)

[115] D. J. Scalapino. *Numerical Studies of the 2D Hubbard Model*. In J. R. Schrieffer and J. S. Brooks, editors, *Handb. High-Temperature Supercond. Theory Exp.*, pages 495–526. Springer New York (2007). (Cited on page **16**)

[116] A. Moreo. *Magnetic susceptibility of the two-dimensional Hubbard model*. Phys. Rev. B **48**, 3380 (1993). (Cited on pages **16**, **97**, and **107**)

[117] R. Preuss, W. Hanke, C. Gröber, and H. G. Evertz. *Pseudogaps and their interplay with magnetic excitations in the doped 2D hubbard model*. Phys. Rev. Lett. **79**, 1122–1125 (1997). (Cited on pages **16**, **99**, and **107**)

[118] B. Kyung, S. S. Kancharla, D. Sénéchal, A.-M. S. Tremblay, M. Civelli, and G. Kotliar. *Pseudogap induced by short-range spin correlations in a doped Mott insulator*. Phys. Rev. B **73**, 165114 (2006). (Cited on pages **16** and **107**)

[119] X. Chen, J. P. F. LeBlanc, and E. Gull. *Superconducting Fluctuations in the Normal State of the Two-Dimensional Hubbard Model*. Phys. Rev. Lett. **115**, 116402 (2015). (Cited on pages **16** and **107**)

[120] E. W. Huang, C. B. Mendl, S. Liu, S. Johnston, H. C. Jiang, B. Moritz, and T. P. Devereaux. *Numerical evidence of fluctuating stripes in the normal state of high-Tc cuprate superconductors*. Science **358**, 1161–1164 (2017). (Cited on pages **16** and **107**)

[121] M. Qin, C.-M. Chung, H. Shi, E. Vitali, C. Hubig, U. Schollwöck, S. R. White, and S. Zhang. *Absence of Superconductivity in the Pure Two-Dimensional Hubbard Model*. Phys. Rev. X **10**, 31016 (2020). (Cited on pages **16** and **20**)

[122] G. Martinez and P. Horsch. *Spin polarons in the t-J model*. Phys. Rev. B **44**, 317–331 (1991). (Cited on page **16**)

[123] M. Punk, A. Allais, and S. Sachdev. *Quantum dimer model for the pseudogap metal*. Proc. Natl. Acad. Sci. **112**, 9552–9557 (2015). (Cited on pages **16** and **93**)

[124] Y.-H. Zhang and S. Sachdev. *From the pseudogap metal to the Fermi liquid using ancilla qubits*. arXiv.2001.09159 (2020). (Cited on pages **16** and **93**)

[125] U. Löw. *Néel order in the two-dimensional $S = \frac{1}{2}$ Heisenberg model*. Phys. Rev. B **76**, 220409 (2007). (Cited on page **17**)

[126] G. Baskaran, Z. Zou, and P. W. Anderson. *The resonating valence bond state and high-Tc superconductivity - A mean field theory*. Solid State Commun. **63**, 973–976 (1987). (Cited on page **18**)

[127] X.-G. Wen and P. A. Lee. *Theory of Underdoped Cuprates*. Phys. Rev. Lett. **76**, 503–506 (1996). (Cited on page **18**)

[128] R. B. Laughlin. *Evidence for Quasiparticle Decay in Photoemission from Underdoped Cuprates*. Phys. Rev. Lett. **79**, 1726–1729 (1997). (Cited on page **18**)

[129] M. H. Anderson, J. R. Ensher, M. R. Matthews, C. E. Wieman, and E. A. Cornell. *Observation of Bose-Einstein condensation in a dilute atomic vapor*. Science **269**, 198 (1995). (Cited on page **19**)

[130] C. C. Bradley, C. A. Sackett, J. J. Tollett, and R. G. Hulet. *Evidence of Bose-Einstein condensation in an atomic gas with attractive interactions*. Phys. Rev. Lett. **75**, 1687 (1995). (Cited on page **19**)

[131] K. B. Davis, M.-O. Mewes, M. R. Andrews, N. J. van Druten, D. S. Durfee, D. M. Kurn, and W. Ketterle. *Bose-Einstein condensation in a gas of sodium atoms*. Phys. Rev. Lett. **75**, 3969 (1995). (Cited on page **19**)

[132] W. Ketterle and M. W. Zwierlein. *Making, probing and understanding ultracold*

Fermi gases. In *Ultra-cold Fermi Gases.* Società Italiana di Fisica, Bologna (2007). (Cited on pages **19**, **21**, and **30**)

[133] A. J. Daley. *Quantum computing and quantum simulation with group-II atoms.* Quantum Inf. Process. **10**, 865 (2011). (Cited on page **19**)

[134] K. Aikawa, A. Frisch, M. Mark, S. Baier, R. Grimm, and F. Ferlaino. *Reaching Fermi degeneracy via universal dipolar scattering.* Phys. Rev. Lett. **112**, 10404 (2014). (Cited on page **19**)

[135] I. Bloch, J. Dalibard, and W. Zwerger. *Many-body physics with ultracold gases.* Rev. Mod. Phys. **80**, 885 (2008). (Cited on pages **19** and **21**)

[136] M. Lewenstein, A. Sanpera, and V. Ahufinger. *Ultracold atoms in optical lattices.* Oxford University Press (2012). (Cited on page **19**)

[137] M. Endres, M. Cheneau, T. Fukuhara, C. Weitenberg, P. Schauß, C. Gross, L. Mazza, M. C. Bañuls, L. Pollet, I. Bloch, and S. Kuhr. *Observation of correlated particle-hole pairs and string order in low-dimensional Mott insulators.* Science **334**, 200 (2011). (Cited on page **19**)

[138] A. Lukin, M. Rispoli, R. Schittko, M. E. Tai, A. M. Kaufman, S. Choi, V. Khemani, J. Léonard, and M. Greiner. *Probing entanglement in a many-body-localized system.* Science **364**, 256 LP – 260 (2019). (Cited on page **19**)

[139] M. Rispoli, A. Lukin, R. Schittko, S. Kim, M. E. Tai, J. Léonard, and M. Greiner. *Quantum critical behaviour at the many-body localization transition.* Nature **573**, 385–389 (2019). (Cited on page **19**)

[140] T. Fukuhara, P. Schauß, M. Endres, S. Hild, M. Cheneau, I. Bloch, and C. Gross. *Microscopic observation of magnon bound states and their dynamics.* Nature **502**, 76 (2013). (Cited on page **19**)

[141] P. M. Preiss, R. Ma, M. E. Tai, A. Lukin, M. Rispoli, P. Zupancic, Y. Lahini, R. Islam, and M. Greiner. *Strongly correlated quantum walks in optical lattices.* Science **347**, 1229–1233 (2015). (Cited on pages **19**, **53**, and **62**)

[142] R. Grimm, M. Weidemüller, and Y. B. Ovchinnikov. *Optical Dipole Traps for Neutral Atoms.* volume 42 of *Advances In Atomic, Molecular, and Optical Physics*, pages 95–170. Academic Press (2000). (Cited on page **19**)

[143] F. Le Kien, P. Schneeweiss, and A. Rauschenbeutel. *Dynamical polarizability of atoms in arbitrary light fields: general theory and application to cesium.* Eur. Phys. J. D **67**, 92 (2013). (Cited on page **20**)

[144] B. Albrecht, Y. Meng, C. Clausen, A. Dareau, P. Schneeweiss, and A. Rauschenbeutel. *Fictitious magnetic field gradients in optical microtraps as an experimental tool for interrogating and manipulating cold atoms*. Phys. Rev. A **94**, 061401 (2016). (Cited on page **20**)

[145] T. Y. Wu, A. Kumar, F. Giraldo, and D. S. Weiss. *Stern-Gerlach detection of neutral-atom qubits in a state-dependent optical lattice*. Nat. Phys. **15**, 538–542 (2019). (Cited on pages **20** and **62**)

[146] E. Duchon, Y. L. Loh, and N. Trivedi. *Optical lattice emulators: Bose- and Fermi-Hubbard models*. In K.-H. Bennemann and J. B. Ketterson, editors, *Nov. Superfluids Vol. 2*. Oxford University Press (2014). (Cited on page **21**)

[147] L. Duca, T. Li, M. Reitter, I. Bloch, M. Schleier-Smith, and U. Schneider. *An Aharonov-Bohm interferometer for determining Bloch band topology*. Science **347**, 288–292 (2015). (Cited on page **22**)

[148] G. B. Jo, J. Guzman, C. K. Thomas, P. Hosur, A. Vishwanath, and D. M. Stamper-Kurn. *Ultracold atoms in a tunable optical kagome lattice*. Phys. Rev. Lett. **108**, 045305 (2012). (Cited on page **22**)

[149] S. Nascimbène, Y.-A. Chen, M. Atala, M. Aidelsburger, S. Trotzky, B. Paredes, and I. Bloch. *Experimental realization of plaquette resonating valence-bond states with ultracold atoms in optical superlattices*. Phys. Rev. Lett. **108**, 205301 (2012). (Cited on page **22**)

[150] D. Mitra, P. T. Brown, E. Guardado-Sanchez, S. S. Kondov, T. Devakul, D. A. Huse, P. Schauß, and W. S. Bakr. *Quantum gas microscopy of an attractive Fermi-Hubbard system*. Nat. Phys. **14**, 173–177 (2018). (Cited on page **22**)

[151] T. Schweigler, V. Kasper, S. Erne, I. Mazets, B. Rauer, F. Cataldini, T. Langen, T. Gasenzer, J. Berges, and J. Schmiedmayer. *Experimental characterization of a quantum many-body system via higher-order correlations*. Nature **545**, 323–326 (2017). (Cited on pages **23** and **26**)

[152] M. Prüfer, T. V. Zache, P. Kunkel, S. Lannig, A. Bonnin, H. Strobel, J. Berges, and M. K. Oberthaler. *Experimental extraction of the quantum effective action for a non-equilibrium many-body system*. Nat. Phys. **16**, 1012–1016 (2020). (Cited on page **23**)

[153] T. V. Zache, T. Schweigler, S. Erne, J. Schmiedmayer, and J. Berges. *Extracting the Field Theory Description of a Quantum Many-Body System from Experimental Data*. Phys. Rev. X **10**, 11020 (2020). (Cited on page **23**)

[154] S. Dowdy, S. Wearden, and D. Chilko. *Statistics for Research*. Wiley, 3rd edition (2011). (Cited on pages **24** and **27**)

[155] C. Gardiner. *Stochastic Methods*. Springer (2009). (Cited on page **26**)

[156] J. M. Tranquada. *Neutron Scattering Studies of Antiferromagnetic Correlations in Cuprates*. In J. R. Schrieffer and J. S. Brooks, editors, *Handb. High-Temperature Supercond. Theory Exp.*, pages 257–298. Springer New York (2007). (Cited on page **28**)

[157] A. Omran. *A microscope for Fermi gases*. PhD thesis, Ludwig-Maximilians-Universität München (2016). (Cited on pages **30**, **31**, and **35**)

[158] M. Boll. *Spin and density resolved microscopy of Hubbard chains*. PhD thesis, Ludwig-Maximilians-Universität München (2016). (Cited on page **30**)

[159] T. Hilker. *Spin-resolved microscopy of strongly correlated fermionic many-body states*. PhD thesis, Ludwig-Maximilians-Universität München (2017). (Cited on pages **30**, **56**, and **114**)

[160] M. E. Gehm. *Properties of ^6Li* (2003). https://www.physics.ncsu.edu/jet/techdocs/pdf/PropertiesOfLi.pdf. (Cited on page **30**)

[161] P. M. Duarte, R. A. Hart, J. M. Hitchcock, T. A. Corcovilos, T.-L. Yang, A. Reed, and R. G. Hulet. *All-optical production of a lithium quantum gas using narrow-line laser cooling*. Phys. Rev. A **84**, 61406 (2011). (Cited on page **30**)

[162] G. Zürn, T. Lompe, A. N. Wenz, S. Jochim, P. S. Julienne, and J. M. Hutson. *Precise characterization of ^6Li Feshbach resonances using trap-sideband-resolved RF spectroscopy of weakly bound molecules*. Phys. Rev. Lett. **110**, 135301 (2013). (Cited on page **31**)

[163] B. DeMarco, S. B. Papp, and D. S. Jin. *Pauli Blocking of Collisions in a Quantum Degenerate Atomic Fermi Gas*. Phys. Rev. Lett. **86**, 5409–5412 (2001). (Cited on page **33**)

[164] R. Onofrio. *Cooling and thermometry of atomic Fermi gases*. Physics-Uspekhi **59**, 1129–1153 (2016). (Cited on page **33**)

[165] C. S. Chiu, G. Ji, A. Mazurenko, D. Greif, and M. Greiner. *Quantum State Engineering of a Hubbard System with Ultracold Fermions*. Phys. Rev. Lett. **120**, 243201 (2018). (Cited on pages **33** and **108**)

[166] B. Yang, H. Sun, C. J. Huang, H. Y. Wang, Y. Deng, H. N. Dai, Z. S. Yuan, and

J. W. Pan. *Cooling and entangling ultracold atoms in optical lattices.* Science **369,** 550–553 (2020). (Cited on page **33**)

[167] M. S. Safronova, B. Arora, and C. W. Clark. *Frequency-dependent polarizabilities of alkali-metal atoms from ultraviolet through infrared spectral regions.* Phys. Rev. A **73,** 022505 (2005). (Cited on page **38**)

[168] B. Pasquiou, A. Bayerle, S. M. Tzanova, S. Stellmer, J. Szczepkowski, M. Parigger, R. Grimm, and F. Schreck. *Quantum degenerate mixtures of strontium and rubidium atoms.* Phys. Rev. A **88,** 23601 (2013). (Cited on page **38**)

[169] A. Bayerle. *Ultracold strontium and rubidium: mixtures, quantum gases and molecules.* PhD thesis, Universiteit van Amsterdam (2017). (Cited on page **38**)

[170] V. A. Dzuba and A. Derevianko. *Dynamic polarizabilities and related properties of clock states of the ytterbium atom.* J. Phys. B At. Mol. Opt. Phys. **43,** 74011 (2010). (Cited on page **38**)

[171] C. Hofrichter. *Probing the SU(N) Fermi-Hubbard model with ytterbium atoms in an optical lattice.* PhD thesis, Ludwig-Maximilians-Universität München (2016). (Cited on page **38**)

[172] M. Lubasch, V. Murg, U. Schneider, J. I. Cirac, and M.-C. Bañuls. *Adiabatic Preparation of a Heisenberg Antiferromagnet Using an Optical Superlattice.* Phys. Rev. Lett. **107,** 165301 (2011). (Cited on pages **40**, **44**, and **108**)

[173] A. Kantian, S. Langer, and A. J. Daley. *Dynamical Disentangling and Cooling of Atoms in Bilayer Optical Lattices.* Phys. Rev. Lett. **120,** 060401 (2018). (Cited on pages **40**, **105**, and **108**)

[174] W. P. Su, J. R. Schrieffer, and A. J. Heeger. *Solitons in polyacetylene.* Phys. Rev. Lett. **42,** 1698 (1979). (Cited on page **40**)

[175] K. P. Birch and M. J. Downs. *An Updated Edlén Equation for the Refractive Index of Air.* Metrologia **30,** 155–162 (1993). (Cited on pages **45** and **111**)

[176] B. E. A. Saleh and M. C. Teich. *Electro-Optics.* John Wiley & Sons, Ltd (1991). (Cited on pages **47** and **109**)

[177] R. Boyd. *Nonlinear Optics.* Academic Press (2008). (Cited on page **47**)

[178] M. Höse. *Erforschung eines bichromatischen optischen Supergitters für ein Fermi Gas Mikroskop.* Master's thesis, Ludwig-Maximilians-Universität München (2018). (Cited on pages **47** and **48**)

[179] D. Bourgund. *High-Stability, Tunable, Bichromatic Superlattice*. Master's thesis, Ludwig-Maximilians-Universität München (2019). (Cited on page **48**)

[180] K. D. Nelson, X. Li, and D. S. Weiss. *Imaging single atoms in a three-dimensional array*. Nat. Phys. **3**, 556–560 (2007). (Cited on page **53**)

[181] D. Barredo, V. Lienhard, S. de Léséleuc, T. Lahaye, and A. Browaeys. *Synthetic three-dimensional atomic structures assembled atom by atom*. Nature **561**, 79–82 (2018). (Cited on page **53**)

[182] O. Elíasson, J. S. Laustsen, R. Heck, R. Müller, J. J. Arlt, C. A. Weidner, and J. F. Sherson. *Spatial tomography of individual atoms in a quantum gas microscope*. Phys. Rev. A **102**, 53311 (2020). (Cited on page **53**)

[183] L. Wang, M. Troyer, and X. Dai. *Topological charge pumping in a one-dimensional optical lattice*. Phys. Rev. Lett. **111**, 026802 (2013). (Cited on page **53**)

[184] M. Lohse, C. Schweizer, O. Zilberberg, M. Aidelsburger, and I. Bloch. *A Thouless quantum pump with ultracold bosonic atoms in an optical superlattice*. Nat. Phys. **12**, 350–354 (2016). (Cited on page **53**)

[185] S. Nakajima, T. Tomita, S. Taie, T. Ichinose, H. Ozawa, L. Wang, M. Troyer, and Y. Takahashi. *Topological Thouless pumping of ultracold fermions*. Nat. Phys. **12**, 296–300 (2016). (Cited on page **53**)

[186] D. J. Thouless. *Quantization of particle transport*. Phys. Rev. B **27**, 6083–6087 (1983). (Cited on page **53**)

[187] M. Atala, M. Aidelsburger, J. T. Barreiro, D. Abanin, T. Kitagawa, E. Demler, and I. Bloch. *Direct measurement of the Zak phase in topological Bloch bands*. Nat. Phys. **9**, 795–800 (2013). (Cited on page **53**)

[188] O. Romero-Isart and J. J. García-Ripoll. *Quantum ratchets for quantum communication with optical superlattices*. Phys. Rev. A **76**, 052304 (2007). (Cited on page **53**)

[189] Y. Qian, M. Gong, and C. Zhang. *Quantum transport of bosonic cold atoms in double-well optical lattices*. Phys. Rev. A **84**, 13608 (2011). (Cited on page **53**)

[190] A. Damascelli, Z. Hussain, and Z. X. Shen. *Angle-resolved photoemission studies of the cuprate superconductors*. Rev. Mod. Phys. **75**, 473–541 (2003). (Cited on page **58**)

[191] O. Yuli, I. Asulin, O. Millo, D. Orgad, L. Iomin, and G. Koren. *Enhancement of the superconducting transition temperature of La2-xSrxCuO4 bilayers: Role of pairing and phase stiffness*. Phys. Rev. Lett. **101**, 057005 (2008). (Cited on page **58**)

[192] S. S. Kancharla and S. Okamoto. *Band insulator to Mott insulator transition in a bilayer Hubbard model*. Phys. Rev. B **75**, 193103 (2007). (Cited on pages **58** and **59**)

[193] N. Bulut, D. J. Scalapino, and R. T. Scalettar. *Nodeless d-wave pairing in a two-layer Hubbard model*. Phys. Rev. B **45**, 5577–5584 (1992). (Cited on page **58**)

[194] R. T. Scalettar, J. W. Cannon, D. J. Scalapino, and R. L. Sugar. *Magnetic and pairing correlations in coupled Hubbard planes*. Phys. Rev. B **50**, 13419–13427 (1994). (Cited on page **58**)

[195] A. I. Liechtenstein, I. I. Mazin, and O. K. Andersen. *S-wave superconductivity from an antiferromagnetic spin-fluctuation model for bilayer materials*. Phys. Rev. Lett. **74**, 2303–2306 (1995). (Cited on page **58**)

[196] S. Okamoto and T. A. Maier. *Enhanced Superconductivity in Superlattices of High-T c Cuprates*. Phys. Rev. Lett. **101**, 156401 (2008). (Cited on pages **58** and **61**)

[197] K. Bouadim, G. G. Batrouni, F. Hébert, and R. T. Scalettar. *Magnetic and transport properties of a coupled Hubbard bilayer with electron and hole doping*. Phys. Rev. B **77**, 144527 (2008). (Cited on page **58**)

[198] T. A. Maier and D. J. Scalapino. *Pair structure and the pairing interaction in a bilayer Hubbard model for unconventional superconductivity*. Phys. Rev. B **84**, 180513 (2011). (Cited on pages **58** and **61**)

[199] M. Golor, T. Reckling, L. Classen, M. M. Scherer, and S. Wessel. *Ground-state phase diagram of the half-filled bilayer Hubbard model*. Phys. Rev. B **90**, 195131 (2014). (Cited on pages **58** and **59**)

[200] H. Zhai, F. Wang, and D.-H. Lee. *Antiferromagnetically driven electronic correlations in iron pnictides and cuprates*. Phys. Rev. B **80**, 64517 (2009). (Cited on page **58**)

[201] A. W. Sandvik and D. J. Scalapino. *Order-disorder transition in a two-layer quantum antiferromagnet*. Phys. Rev. Lett. **72**, 2777–2780 (1994). (Cited on pages **59** and **61**)

[202] A. W. Sandvik, A. V. Chubukov, and S. Sachdev. *Quantum critical behavior in a two-layer antiferromagnet*. Phys. Rev. B **51**, 16483–16486 (1995). (Cited on page **59**)

[203] L. Wang, K. S. D. Beach, and A. W. Sandvik. *High-precision finite-size scaling analysis of the quantum-critical point of $S = 1/2$ Heisenberg antiferromagnetic bilayers*. Phys. Rev. B **73**, 14431 (2006). (Cited on page **59**)

[204] R. Chen, S. Lee, and L. Balents. *Dimer Mott insulator in an oxide heterostructure*. Phys. Rev. B **87**, 161119 (2013). (Cited on page **59**)

[205] R. Okazaki, Y. Ikemoto, T. Moriwaki, T. Shikama, K. Takahashi, H. Mori, H. Nakaya, T. Sasaki, Y. Yasui, and I. Terasaki. *Optical Conductivity Measurement of a Dimer Mott-Insulator to Charge-Order Phase Transition in a Two-Dimensional Quarter-Filled Organic Salt Compound*. Phys. Rev. Lett. **111**, 217801 (2013). (Cited on pages **59** and **60**)

[206] Y. Shimizu, K. Miyagawa, K. Kanoda, M. Maesato, and G. Saito. *Spin Liquid State in an Organic Mott Insulator with a Triangular Lattice*. Phys. Rev. Lett. **91**, 107001 (2003). (Cited on pages **59** and **60**)

[207] K. Penc and F. Mila. *Charge gap in the one-dimensional dimerized Hubbard model at quarter-filling*. Phys. Rev. B **50**, 11429–11445 (1994). (Cited on page **60**)

[208] M. Kwon, M. F. Ebert, T. G. Walker, and M. Saffman. *Parallel Low-Loss Measurement of Multiple Atomic Qubits*. Phys. Rev. Lett. **119**, 180504 (2017). (Cited on page **62**)

[209] E. Khatami and M. Rigol. *Thermodynamics of strongly interacting fermions in two-dimensional optical lattices*. Phys. Rev. A **84**, 53611 (2011). (Cited on pages **65**, **66**, **76**, **90**, **105**, **123**, and **124**)

[210] R. R. P. Rigol, Marcos and Bryant, Tyler and Singh. *Numerical linked-cluster algorithms. I. Spin systems on square, triangular, and kagomé lattices*. Phys. Rev. E **75**, 061118 (2007). (Cited on pages **65** and **66**)

[211] L. D. Landau. *Electron motion in crystal lattices*. Phys. Z. Sowjet. **3**, 664 (1933). (Cited on pages **69** and **70**)

[212] S. Pekar. *Autolocalization of the electron in an inertially polarizable dielectric medium*. Zh. Eksp. Teor. Fiz. **3**, 664 (1946). (Cited on pages **69** and **70**)

[213] S. Alexandrov and J. T. Devreese. *Advances in Polaron Physics*. Springer (2010). (Cited on pages **69** and **70**)

[214] H. Fröhlich. *Electrons in lattice fields*. Adv. Phys. **3**, 325–361 (1954). (Cited on page **70**)

[215] T. Holstein. *Studies of polaron motion: Part I. The molecular-crystal model*. Ann. Phys. (N. Y). **8**, 325–342 (1959). (Cited on page **70**)

[216] T. Holstein. *Studies of polaron motion: Part II. The "small" polaron*. Ann. Phys. (N. Y). **8**, 343–389 (1959). (Cited on page **70**)

[217] H. A. Jahn, E. Teller, and F. G. Donnan. *Stability of polyatomic molecules in de-*

generate electronic states - Orbital degeneracy. Proc. R. Soc. London. Ser. A - Math. Phys. Sci. **161**, 220–235 (1937). (Cited on page **70**)

[218] P. E. Kornilovitch. *Band Structure of the Jahn-Teller Polaron from Quantum Monte Carlo.* Phys. Rev. Lett. **84**, 1551–1554 (2000). (Cited on page **70**)

[219] S. A. Jackson and P. M. Platzman. *Polaronic aspects of two-dimensional electrons on films of liquid He.* Phys. Rev. B **24**, 499–502 (1981). (Cited on page **70**)

[220] S. N. Klimin, J. Tempere, V. R. Misko, and M. Wouters. *Finite-temperature Wigner solid and other phases of ripplonic polarons on a helium film.* Eur. Phys. J. B **89**, 172 (2016). (Cited on page **70**)

[221] A. S. Alexandrov and A. M. Bratkovsky. *Carrier Density Collapse and Colossal Magnetoresistance in Doped Manganites.* Phys. Rev. Lett. **82**, 141–144 (1999). (Cited on page **70**)

[222] A. S. Alexandrov, G.-m. Zhao, H. Keller, B. Lorenz, Y. S. Wang, and C. W. Chu. *Evidence for polaronic Fermi liquid in manganites.* Phys. Rev. B **64**, 140404 (2001). (Cited on pages **70** and **71**)

[223] N. Mannella, W. L. Yang, K. Tanaka, X. J. Zhou, H. Zheng, J. F. Mitchell, J. Zaanen, T. P. Devereaux, N. Nagaosa, Z. Hussain, and Z.-X. Shen. *Polaron coherence condensation as the mechanism for colossal magnetoresistance in layered manganites.* Phys. Rev. B **76**, 233102 (2007). (Cited on page **70**)

[224] N. Mannella, W. L. Yang, X. J. Zhou, H. Zheng, J. F. Mitchell, J. Zaanen, T. P. Devereaux, N. Nagaosa, Z. Hussain, and Z. X. Shen. *Nodal quasiparticle in pseudogapped colossal magnetoresistive manganites.* Nature **438**, 474–478 (2005). (Cited on page **71**)

[225] S. Watanabe, K. Ando, K. Kang, S. Mooser, Y. Vaynzof, H. Kurebayashi, E. Saitoh, and H. Sirringhaus. *Polaron spin current transport in organic semiconductors.* Nat. Phys. **10**, 308–313 (2014). (Cited on page **71**)

[226] M. Laukamp, G. B. Martins, C. Gazza, A. L. Malvezzi, E. Dagotto, P. M. Hansen, A. C. López, and J. Riera. *Enhancement of antiferromagnetic correlations induced by nonmagnetic impurities: Origin and predictions for NMR experiments.* Phys. Rev. B **57**, 10755–10769 (1998). (Cited on page **72**)

[227] N. Bulut, D. Hone, D. J. Scalapino, and E. Y. Loh. *Static vacancies on a 2D Heisenberg spin-1/2 antiferromagnet.* Phys. Rev. Lett. **62**, 2192–2195 (1989). (Cited on page **72**)

[228] G. Balster Martins, M. Laukamp, J. Riera, and E. Dagotto. *Local Enhancement of Antiferromagnetic Correlations by Nonmagnetic Impurities*. Phys. Rev. Lett. **78**, 3563–3566 (1997). (Cited on page **72**)

[229] G. B. Martins, R. Eder, and E. Dagotto. *Indications of spin-charge separation in the two-dimensional t-J model*. Phys. Rev. B **73**, 170–173 (1999). (Cited on page **80**)

[230] G. B. Martins, C. Gazza, J. C. Xavier, A. Feiguin, and E. Dagotto. *Doped Stripes in Models for the Cuprates Emerging from the One-Hole Properties of the Insulator*. Phys. Rev. Lett. **84**, 5844–5847 (2000). (Cited on page **80**)

[231] J. Koepsell, J. Vijayan, P. Sompet, F. Grusdt, T. A. Hilker, E. Demler, G. Salomon, I. Bloch, and C. Gross. *Imaging magnetic polarons in the doped Fermi-Hubbard model*. Nature **572**, 358–362 (2019). (Cited on pages **81** and **107**)

[232] A. Bohrdt, D. Greif, E. Demler, M. Knap, and F. Grusdt. *Angle-resolved photoemission spectroscopy with quantum gas microscopes*. Phys. Rev. B **97**, 125117 (2018). (Cited on page **83**)

[233] Z. Z. Yan, Y. Ni, C. Robens, and M. W. Zwierlein. *Bose polarons near quantum criticality*. Science **368**, 190 LP – 194 (2020). (Cited on page **83**)

[234] L. Radzihovsky and D. E. Sheehy. *Imbalanced Feshbach-resonant Fermi gases*. Reports Prog. Phys. **73**, 076501 (2010). (Cited on page **83**)

[235] R. Schmidt, M. Knap, D. A. Ivanov, J.-S. You, M. Cetina, and E. Demler. *Universal many-body response of heavy impurities coupled to a Fermi sea: a review of recent progress*. Reports Prog. Phys. **81**, 24401 (2018). (Cited on page **83**)

[236] J. Koepsell, D. Bourgund, P. Sompet, S. Hirthe, A. Bohrdt, Y. Wang, F. Grusdt, E. Demler, G. Salomon, C. Gross, and I. Bloch. *Microscopic evolution of doped Mott insulators from polaronic metal to Fermi liquid*. arXiv:2009.04440v1 (2020). (Cited on pages **92** and **107**)

[237] D. Pines. *Theory of Quantum Liquids: Normal Fermi Liquids*. CRC Press (2018). (Cited on page **93**)

[238] Y. M. Vilk, L. Chen, and A. M. Tremblay. *Theory of spin and charge fluctuations in the Hubbard model*. Phys. Rev. B **49**, 13267–13270 (1994). (Cited on page **93**)

[239] A.-M. S. Tremblay. *Two-Particle-Self-Consistent Approach for the Hubbard Model*. In A. Avella and F. Mancini, editors, *Strongly Correl. Syst. Theor. Methods*, pages 409–453. Springer Berlin Heidelberg, Berlin, Heidelberg (2012). (Cited on page **93**)

[240] A. Moreo, D. J. Scalapino, R. L. Sugar, S. R. White, and N. E. Bickers. *Numerical study of the two-dimensional Hubbard model for various band fillings*. Phys. Rev. B **41**, 2313–2320 (1990). (Cited on page **96**)

[241] N. Furukawa and M. Imada. *Two-Dimensional Hubbard Model - Metal Insulator Transition Studied by Monte Carlo Calculation -*. J. Phys. Soc. Japan **61**, 3331–3354 (1992). (Cited on page **96**)

[242] S. W. Cheong, G. Aeppli, T. E. Mason, H. Mook, S. M. Hayden, P. C. Canfield, Z. Fisk, K. N. Clausen, and J. L. Martinez. *Incommensurate magnetic fluctuations in La2-xSrxCuO4*. Phys. Rev. Lett. **67**, 1791–1794 (1991). (Cited on page **96**)

[243] A. Bohrdt, Y. Wang, J. Koepsell, M. Kánasz-Nagy, E. Demler, and F. Grusdt. *Dominant fifth-order correlations in doped quantum anti-ferromagnets*. arXiv:2007.07249v2 (2020). (Cited on page **106**)

[244] F. Grusdt, Z. Zhu, T. Shi, and E. A. Demler. *Meson formation in mixed-dimensional t-J models*. SciPost Phys. **5**, 57 (2018). (Cited on page **108**)

[245] H. P. Büchler. *Microscopic derivation of Hubbard parameters for cold atomic gases*. Phys. Rev. Lett. **104**, 090402 (2010). (Cited on page **119**)

[246] S. Trotzky, P. Cheinet, S. Fölling, M. Feld, U. Schnorrberger, A. M. Rey, A. Polkovnikov, E. A. Demler, M. D. Lukin, and I. Bloch. *Time-Resolved Observation and Control of Superexchange Interactions with Ultracold Atoms in Optical Lattices*. Science **319**, 295–299 (2008). (Cited on page **121**)

Acknowledgments

I would like to express my deepest gratitude to the following non-exhaustive list of people:

My supervisor Immanuel Bloch for offering me this PhD position and for making his group at MPQ a special place, where research can be pushed to its limits. For his inspiring and encouraging attitude and for sharing his enthusiasm and excitement about physics. Furthermore, thank you for all the support and freedom I experienced during my time.

I would equally like to thank our lithium-lab leader Christian Gross. For his pragmatic thinking and his keen ideas. For making complicated things simple, for being a critical mind and for finding a good balance. Thank you for being a fascinating experimentalist, who always has an open ear.

The entire lithium team. The previous generation, Ahmed Omran, Martin Boll, Timon Hilker, and Guillaume Salomon, for all the effort they put into the construction of this powerful machine. My labmate Jayadev Vijayan, with whom I learned to tame this machine. The newer generation with Pimonpan Sompet, Sarah Hirthe, and Dominik Bourgund, whom I would like to thank for their hard work and the fantastic atmosphere during our one year of upgrading the machine! Thomas Chalopin and Petar Bojovic are two great new additions to the team. Together with our new lab-leader Timon Hilker, they make an excellent fellowship and I can't wait to see where the machine will take you in the future!

I would like to highlight the contribution of Guillaume Salomon, my office mate, whose input was very essential. I learned a great deal from him and our physics discussions were very enlightening.

Our theory collaborator Eugene Demler, for all the brilliant thoughts he shared, for his dedication to our projects, for willing to referee my thesis, and for hosting my MPHQ stay.

Fabian Grusdt and Annabelle Bohrdt, for being great friends on and off the pitch. For their contributions to our numerous collaborations. Thank you for all the helpful discussions and the many exciting ideas!